

HETEROSTRUCTURES OF TOPOLOGICAL INSULATORS AND SUPERCONDUCTORS

by

Mahmoud Lababidi
A Dissertation Submitted
to the Graduate Faculty
of
George Mason University
in Partial Fulfillment of
The Requirements for the Degree
of
Doctor of Philosophy
Physics

Committee:

Dr. Erhai Zhao,
Dissertation Director

Dr. Dimitrios A. Papaconstantopoulos,
Committee Member

Dr. Predrag Nikolic,
Committee Member

Dr. Qiliang Li,
Committee Member

Dr. Michael E. Summers,
Director, School of Physics,
Astronomy, and Computational Science

Dr. Timothy L. Born,
Associate Dean for Student and Academic
Affairs, College of Science

Dr. Vikas Chandhoke, Dean,
College of Science

Date: JULY 2 , 2013

Summer Semester 2013
George Mason University, Fairfax, VA

Heterostructures of Topological Insulators and Superconductors

A dissertation submitted in partial fulfillment of the requirements for the degree of
Doctor of Philosophy at George Mason University

By

Mahmoud Lababidi
Bachelor of Science
University of Florida, 2006

Director: Dr. Erhai Zhao, Assistant Professor
School of Physics, Astronomy and Computational Science

Summer Semester 2013
George Mason University
Fairfax, VA

Copyright © 2013 by Mahmoud Lababidi
All Rights Reserved

Dedication

To Angus Macgyver, who needed only a roll of duct tape, paperclip, and a Swiss Army knife to solve any problem.
To my parents, Lina and Steve, for sacrificing their lives for me, my future, and my success and happiness in life.

Acknowledgments

First and foremost, I'd like to thank the most driven, understanding and supportive advisor anyone could ask for, Erhai Zhao. Not only have I learned more about physics than I could ever imagine, he has mentored me on being a good scientist, and a disciplined worker. I really could not have asked for a better advisor to lead me through this fascinating journey. I'd like to thank Dr. Papa for his incredible generosity from day one. He supported me throughout my PhD and without that support I would not have successfully completed the many projects and publications I have had. I consider Paul So to be more than just a graduate department advisor. You could add resident psychologist to his title and it would be wholly appropriate. Without his clear guidance on all topics, including ones beyond physics and art, I would be a lost soul. Furthermore, I thank Mike Summers for his help as a department chair and helping me in times of need. He has supported me financially at times and has always had an open door for me and any graduate student to talk to him.

Joe Weingartner would be considered the "House Dad" of the fraternity of the physics department. He has been a guiding light to me in many ways including physics and life. He is without a doubt one of the most important people the department has given tenure to for his kindness and empathy for anyone who walks into his office. I am very grateful to Indu Satija for her amazing creativity and beautiful ability to see physics like no one has. I give her full credit for the idea that spawned my most fascinating project on the driven quantum Hall system. I thank Predrag Nikolic, not only as helpful committee member but as great educator. He has always welcomed healthy discussion about a variety of topics that have helped me in my career numerous times. Qiliang Li has been one of the most excited and appreciative members I could have on my committee. His enthusiasm towards my work has been a heavy driver for a significant portion of my research. Ming Tian was the first person to take me under her wing as a student. She saw I had potential and ability to do physics and immediately gave me challenging problems to work on. She has been very supportive of my endeavours even if it meant changing groups. I thank Gerald Cook, the first Professor I interacted with during my first steps inching towards the wormhole of grad school, and his early enthusiasm for me to begin this journey. Phil Rubin was the person that urged me to apply to the program regardless of my physics background because he believed I'd do great. Somehow he was right. I later learned Phil was in a Psychology PhD program when he switched to physics. That's serious inspiration.

Without Kathleen Enos, Mari-Elaine Triolo, Geoff Elkins, Stephanie Monk, and Melissa Hayes I would be wrapped up in more paperwork than I could handle. They have made my this trip as smooth as possible and have been the best people to have around. Of course without Dan Thomas and Andrew Abdalian I'd be a headless chicken running around with regards to my IT issues.

Thank you Stephen Gildea for inspiring me to go to graduate school by becoming a rocket scientist and kicking ass at it. Anish Mitra, my first friend in graduate school and roommate, deserves much recognition for being the one person that was as interested in

math and science as I was. Indrajit Das and Zrinka Greguric Ferencek are staples in my early career. I owe much to them for their stimulating discussions while we completed course work together. Timofey Frolov is my favorite Russian physicist, metal guitarist, food snob I've ever known. He has been a great friend and colleague during our years at GMU before he ditched me for Berkeley. Ol' Dirty himself, Greg Byrne, deserves more than a mention here for our antics during these years especially at the Arlington Office. Many thanks go to Devin Vega and our enjoyable and stimulating discussions in course work and research under Ming Tian.

Quite importantly, I'd like to thank Lois Cohen, Edmund Lau, and Jean Wright for their influence during my formative high school years. I owe them more than just a line in this theses and without them I truly would not be here. The same goes for Anand Rangarajan and Eric Schwartz from my time at University of Florida, two professors who challenged me in innovative and creative ways.

Not least, I'd like to thank SPACS, Office of Naval Research, Air Force Office of Scientific Research, National Science Foundation and National Institute of Standards and Technology for the funding they have provided me over these years.

Table of Contents

	Page
List of Figures	viii
List of Symbols	xii
Abstract	xiii
1 Introduction	1
1.1 Topological Insulators	1
1.2 Superconductivity	7
1.2.1 Measurement	7
1.2.2 BCS and Bogoliubov Theory	9
1.3 Topological Superconductors and Superconductor-Topological Insulator Heterostructures	12
1.3.1 p_x+ip_y superconductors	13
1.3.2 Fu-Kane Superconductor/Topological Insulator Model	14
2 Metal to Topological Insulator Scattering	17
2.1 Introduction	18
2.2 Model Hamiltonian and Complex Band Structure	20
2.3 Scattering Matrix from Wave-Function Matching	23
2.4 Interface Spectrum and Scattering Matrix from Lattice Green Function	27
2.5 Discussions	31
3 Superconducting Proximity Effect	32
3.1 Introduction	32
3.2 Model and Basic Equations	35
3.3 Fourier Expansion	42
3.4 The Order Parameter	44
3.5 The Interface Mode and the Fu-Kane Model	48
3.6 Triplet Pair Correlations	50
3.7 Summary	57
4 Josephson Junction on TI Surface	60
4.1 Introduction	60

4.2	Model	61
4.3	Flat Bands in Spectrum	66
4.4	Periodic π Junction	67
4.5	Summary	69
5	Summary and Outlook	73
A	Additional Papers	75
	Bibliography	87

List of Figures

Figure	Page
1.1 (a) Energy spectrum of a trivial band insulator where two bands, conduction and valence, are separated by an energy gap. (b) Energy spectrum of a quantum Hall state. The gap now has one chiral edge state connecting the valence band to the conduction band. (c) Energy spectrum of a 2D TI (QSH). The gap now has one pair of chiral edge states connecting the valence band to the conduction band. One line is for the spin up state and the other is for the spin down state. This essentially mimics two copies of the quantum Hall state for each spin.	3
1.2 Dirac cone dispersion. Energy as a function of momentum, k_x and k_y	5
1.3 (left) Four probe measurement device. Probes 1 and 4 are used to flow a current across a sample while probes 2 and 3 measure the voltage drop across the sample where the current is flowing. (right) Resistance (Ω) vs Temperature (Kelvin) experiment on $\text{Cu}_{2.2}\text{Bi}_2\text{Se}_3$ from arXiv:1111.5805. The drop in resistance is a signature of superconductivity.	8
1.4 Energy spectrum for a BCS superconductor with a gap of $2\Delta_0$ and $\mu/\Delta_0 = 10$	12
1.5 Energy spectrum for a $p_x \pm ip_y$ superconductor with a chemical potential domain wall, ensuring linearly dispersing Majorana modes.	14
2.1 (a) Scattering geometry at a metal (M)-topological insulator (TI) interface. (b) Schematic band structure of the metal (modeled by \hat{H}_M) and topological insulator.	21
2.2 The complex band structure of topological insulator described by $\hat{H}_{TI}(\mathbf{k})$ for $k_y = 0$, $k_x = 0.02$ (left) and 0.04 (right). E is measured in eV, and k in \AA^{-1} . Subgap states with complex k_z represent evanescent waves. The topology of real lines [1] changes as k_x is increased.	22

2.3	The magnitudes (upper panel) and the phases (lower panel) of the spin-flip amplitude f and spin-conserving amplitude g versus the incident angle θ . $E = 0.1\text{eV}$, $E_F=0.28\text{eV}$. $ g ^2 + f ^2 = 1$. $\text{Arg}(g)$ and $\text{Arg}(f)$ are shifted upward by π for clarity.	26
2.4	The spectral function $N(E, k_x, k_y = 0)$ at the interface of metal and topological insulator. Left: good contact, $J = t_M$, showing the continuum of metal induced gap states. Right: poor contact with low transparency, $J = 0.2t_M$, showing well defined Dirac spectrum as on the TI surface. $t_M = 0.18\text{eV}$, $\mu_M = -4t_M$, a is lattice spacing.	28
2.5	The spin-conserving reflection amplitude $ g $ and spin rotation angle α versus the incident angle θ for increasing contact transparency, $J/t_M = 0.25, 1, 1.5, 2$ (from left to right). $t_M = 0.18\text{eV}$, $\mu_M = -4t_M$, $E = 0.05\text{eV}$, $k_y = 0$. $ f ^2 = 1 - g ^2$	29
3.1	Schematic (not to scale) band diagrams in a superconductor-topological insulator (S-TI) proximity structure. E_f is the Fermi energy of the metal described by H_M measured from the band crossing point. μ is the chemical potential of TI measured from the band gap center. The superconducting gap is much smaller than the band gap of TI.	37
3.2	The superconducting order parameter $\Delta(z)$ near an S-TI interface at $z = d = 0.95L$. The superconductor occupies $0 < z < d$, and topological insulator occupies $d < z < L$. $L = 300 \text{ nm}$, $\mu=0$, the bulk gap $\Delta_0 = 0.6\text{meV}$	44
3.3	The order parameter $\Delta(z)$ near an S-TI interface at $z = d = 0.9L$. $L = 160 \text{ nm}$, $\mu=0$, $\Delta_0 \sim 2.4\text{meV}$	46
3.4	The order parameter profile for two different chemical potentials of the topological insulator, $\mu = -0.1\text{eV}$ and $\mu = 0.2\text{eV}$. $L = 160\text{nm}$, $\Delta_0 \sim 5.2\text{meV}$	47
3.5	The lowest few energy levels $\epsilon_n(k_{ })$. $\mu = 0$, $L = 160\text{nm}$, and the bulk superconducting gap $\Delta_0 \sim 5.2\text{meV}$. A well-defined interface mode is clearly visible at sub-gap energies. Solid lines show a fit to the Fu-Kane model, with $\Delta_s = 1.8\text{meV}$, $v_s = 2.7\text{eV}\text{\AA}$, and $\mu_s = 7.5\text{meV}$	49
3.6	The dispersion of the lowest energy level for different μ (in eV). Other parameters are the same as in Fig. 3.5, $L = 160\text{nm}$ and $\Delta_0 \sim 5.2\text{meV}$. Fu-Kane model well describes the lowest energy mode. As μ is increased, Δ_s and v_s stay roughly the same, while μ_s scales linearly with μ	51

3.7	The spectral function $N(k_{\parallel}, z, \omega)$ of the lowest energy level, $\omega = E_{min}$, shown in Fig. 3.6. The interface is at $z = 0.9L$, $L = 160\text{nm}$. The spectral function oscillates rapidly with z , so only its envelope is plotted.	52
3.8	The local density of states $N(E, z)$ at $z = 0.8d$ and $z = 0.85d$ (the interface is at $z = 0.9d$). $\mu = 0$, $L = 160\text{nm}$, and $\Delta_0 \sim 5.2\text{meV}$. The subgap states are due to the interface mode. A level broadening $\sim 0.01\Delta_0$ is used.	53
3.9	The lowest energy level of an S-TI structure with $L = 160\text{nm}$, $d = 0.9L$, $\Delta_0 = 2.4\text{meV}$. μ is the chemical potential of the TI and measured in eV.	54
3.10	The imaginary part of triplet pair correlation function $F_{\uparrow\uparrow}(k_{\parallel}, z)$. The S-TI interface is at $d = 0.9L$. $\mu = 0$, $L = 160\text{nm}$, $\Delta_0 = 5.2\text{meV}$	56
3.11	The imaginary part of $F_{\uparrow\uparrow}(k_{\parallel}, z)$. $\mu = 0$, $L = 300\text{nm}$, $d = 0.95L$, $\Delta_0 = 0.6\text{meV}$. As comparison, the data points show the singlet pair correlation function $F_{\uparrow\downarrow}(k_{\parallel}, z = 0.9L)/3$	58
4.1	(color online) a) Schematic of a Josephson junction on the surface of a topological insulator (TI). The two superconducting leads (S) have a phase difference π . Δ is the superconducting gap, and w is the junction width (not to scale). b) Specular Andreev reflection in the regime $E > \mu$. c) Retro-reflection for $E < \mu$. d) Dark lines show the (k_y, μ) values for the zero energy Andreev bound states for $w = 10\hbar v_F/\Delta$ and $L \rightarrow \infty$. k_y is in unit of $\Delta/\hbar v_F$	62
4.2	(color online) The local spectral function $A_{\uparrow}(E, k_y, x)$ (upper panel) and local density of states $N(E, x)$ (lower panel, red solid line) at the center of the junction, $x = 0.5L$. One sees “flat” Andreev bound states near zero energy for $-k_F < k_y < k_F$, and correspondingly a pronounced peak at zero energy in the LDOS in the lower panel. The lower panel also shows different LDOS away from the center, for x from $0.52L$ to $0.58L$	65
4.3	(color online) Upper panel: Schematic of the periodic proximity structure with $\Delta(x) = \Delta \sin(\pi x/a)$. The wave function $ u(x) $ for the zero energy states are peaked at the domain wall boundaries, $x = ma$. Lower panel: Energy spectrum for $a = 24\hbar v_F/\Delta$ and $\mu = 4\Delta$ is flat at zero energy, which has fine structures upon closer inspection.	70

- 4.4 (color online) Spectral density function, $A(x = .5L, k_y, E)$, for values of μ from 0 eV to .14 eV. This images are used in a movie found online[2]. The linear dispersion ($E \sim k$) transitions to a flat band ($E \sim k^N$) as μ increases. This flat band is responsible for the peak in DOS in figure 4.2. 71
- 4.5 Fine structures in the energy spectrum of the periodic proximity structure with fixed $a = 12\hbar v_F/\Delta$ and increasing μ . The linearly dispersing Majorana spectrum at $\mu = 0$ splits and develops curvature to eventually become nearly flat within $(-k_F, k_F)$. The number of zero energy crossings increases with μ . 72

List of Symbols

v_F	Fermi velocity of Dirac electrons
\vec{k}	momentum vector
k_i	momentum in the i -th direction
\mathcal{E}_F	Fermi energy
$A(x, k, \epsilon)$	spin(σ), momentum and position resolved density of (energy) states
$N(x, \epsilon)$	spin(σ) and position resolved density of (energy) states
μ	chemical potential, sometimes as Fermi energy (\mathcal{E}_F)
\mathcal{H}	Hamiltonian
$\psi(x)$	wave function of particle
u_σ (v_σ)	Bogoliubov-de Gennes quasi-particle (hole) wave function
k_B	Boltzmann's constant

Abstract

HETEROSTRUCTURES OF TOPOLOGICAL INSULATORS AND SUPERCONDUCTORS

Mahmoud Lababidi, PhD

George Mason University, 2013

Dissertation Director: Dr. Erhai Zhao

Topological insulators (TI), such as Bi_2Se_3 , are a new class of quantum materials discovered recently. They are insulating in the bulk but can conduct on the surfaces. The robust surface states of three-dimensional strong TIs form a unique two-dimensional system of massless electrons, known as a helical metal, with a linear energy-momentum dispersion and spin-momentum locking. While these surface modes alone have spurred great interest, their interaction with superconductors (S) in close proximity has opened up opportunities to engineer topological superconductivity using TI-S heterostructures. This thesis is a microscopic, self-consistent theoretical investigation of the interplay between TI and superconductors. Three types of TI-based heterostructures with increasing complexity are studied in detail.

We first present a detailed study of the coupling between a metal and a topological insulator. We compute the spin-active scattering matrix for electrons coming from the metal incident on the metal-TI interface. We find that there exists a critical incident angle, where perfect spin-flip occurs as the incoming electron is reflected. We discuss the origin of this phenomena and its potential implications in spintronics. We then compute the local spectrum at the metal-TI interface, and examine its evolution from the tunneling limit

(bad contact) to the strong coupling limit (good contact). The calculations are done using two complementary approaches; in a continuum model based on a $\mathbf{k} \cdot \mathbf{p}$ Hamiltonian a wave function matching approach is taken and the lattice model requires the use of lattice Green's functions. The study of metal-TI interface lays the foundation for our subsequent theory of S-TI interface.

Next we carry out microscopic, self-consistent calculations of the superconducting order parameter and pairing correlations near a S-TI interface, where S is an *s*-wave superconductor. We discuss the suppression of the order parameter by the topological insulator and show that triplet pairing correlations are induced by spin-flip scattering at the interface. We verify that the interface spectrum at sub-gap energies is well described by the Fu-Kane model even for strongly coupled S and TI. These sub-gap modes are interface states with spectral weight penetrating well into the superconductor. We extract the phenomenological parameters of the phenomenological Fu-Kane model from our microscopic calculations, and find they are strongly renormalized from the bulk material parameters.

Building upon such understanding of single TI-S interface, we move on to examine a TI surface in contact with two superconductors with a phase bias, namely a Josephson junction patterned on the TI surface and mediated by the helical metal. A short Josephson junction of this kind at a phase bias of π is known to give rise to exotic quasiparticle excitations known as Majorana fermions with a linear dispersion, $E \sim k$. Our self-consistent calculation of the Andreev bound states spectrum reveals, for the first time, a new regime with very different physics in these devices. We show that the subgap spectrum becomes nearly flat at zero energy when the chemical potential is sufficiently away from the Dirac point. The flat dispersion is well approximated by $E \sim k^N$, where N scales with the chemical potential. We find a similar linear-to-flat dispersion evolution also occurs for the subgap spectrum of a periodic superconducting proximity structure, such as a TI surface in contact with a striped superconductor.

The systematic microscopic study of TI-S heterostructures helps interpret the data from ongoing experiments on these structures. The formalism developed also forms the basis for subsequent investigation of more complicated layered materials such as the periodic

array of magnetically doped TI and S which is argued to give rise to an exotic topological superconductor known as Weyl superconductor.

Chapter 1: Introduction

This thesis presents a systematic theoretical study of the interaction and interplay between a new class of materials named Topological Insulators (TIs) and superconductors. It consists of five chapters. The first chapter contains a brief introduction to TIs and superconductors. In addition, it describes basic concepts and notations used later in the bulk of the thesis. These include the topological surface states of a TI, the spin texture of the TI surface, phenomenological description of a superconductor coupled to a TI, exotic superconductors, and a Josephson junction structure on a TI surface. The second chapter presents a study of the interaction between metal and TI, and electron scattering at the M-TI interface. This chapter provides insight into understanding the effect of spin-orbit interactions on incoming arbitrarily spin-polarized electrons. The third chapter is a microscopic study of a heterostructure of a superconductor with a TI. The motivation is to understand the effect of a TI on an s -wave superconductor. The fourth chapter examines Josephson junctions on a TI surface and delves into new aspects of the energy spectra in regimes not studied before. Each chapter beyond Chapter 1 represents an original work published in Physical Review B.

1.1 Topological Insulators

The field of condensed matter physics has a history of understanding phases of matter that have been condensed. Where the early focus was on solids and liquids, the field has transitioned into studying a rich variety of novel phases that are much more complex. A result of the exploration of many of these novel phases, the concept of order arose, allowing, not only the ability to categorize these phases by recognizing the type of order the system had but the order is usually associated with symmetries of the system. This idea is clearly

seen in the phase transition of liquid atoms with rotational and translational symmetry into a crystal with discrete symmetries (e.g. translational, discrete rotational, inversion, etc.). An extension to this would be a paramagnet transitioning into a ferromagnet, thus breaking time-reversal symmetry. While this study of symmetry breaking is at the heart of condensed matter and allows for a deeper understanding, it is not the full story.

In 1980 Klaus von Klitzing et al performed an experiment measuring the Hall conductance of semiconductor heterostructures in a strong magnetic field[3]. What they found in the experiment was that the measured Hall conductance came in exact quantized fundamental units of e^2/h ,

$$\sigma = \nu \frac{e^2}{h}, \quad (1.1)$$

where ν is an integer value. The significance of this result was not only in the quantized nature of the Hall conductance, but something a bit deeper. This integer quantum Hall effect was special because this result could not be described through the usual symmetry breaking language. In the heterostructure used in the experiment, the internal “bulk” of the system is effectively a two dimensional electron gas exposed to a strong magnetic field. The strong magnetic field puts the electrons in a cyclotron orbit and forces the electrons into discrete energy levels, the Landau levels. This effect is rather similar to a harmonic oscillator where an electron is in a spatially quadratic electric potential well ($V(x) \propto x^2$). These separated energy levels allows for the system to be an insulator when the Fermi energy is placed within the gap between two separate energy levels. While this system is in an insulating state, the edge is still a host to electronic states that propagate in a chiral manner. This discrepancy between the ability to describe bulk of the material and its edge is the issue at hand.

The quantum Hall effect (QHE) is actually a topological phase of matter, with its energy bands described by topological invariants known as Chern numbers. An integer QH phase protected from being deformed into a phase with different topology in the same way a donut (torus) is protected from being deformed into a sphere. The only time such a change

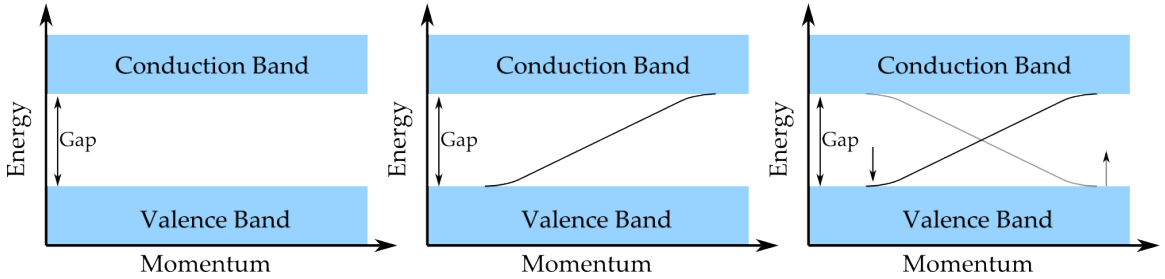


Figure 1.1: (a) Energy spectrum of a trivial band insulator where two bands, conduction and valence, are separated by an energy gap. (b) Energy spectrum of a quantum Hall state. The gap now has one chiral edge state connecting the valence band to the conduction band. (c) Energy spectrum of a 2D TI (QSH). The gap now has one pair of chiral edge states connecting the valence band to the conduction band. One line is for the spin up state and the other is for the spin down state. This essentially mimics two copies of the quantum Hall state for each spin.

is possible is through a phase transition where the gap in the energy spectrum closes in a critical fashion. More discussions on topological phases of matter can be found in literature.

We use the QHE as a lead-in for the topological insulator. By taking the QHE, we can extend it in the following way. The QHE is a gapped system with chiral edge states that depend on the applied magnetic field (see Fig. 1.1). The chirality of the edge states depend on the direction of the magnetic field, i.e. positive (negative) chiral motion of the electrons for positive (negative) out of plane magnetic field. If a system were to have both positive and negative magnetic fields simultaneously for two different species of electrons, we would see the electrons follow the two chiral motions simultaneously depending on their species. The two different species of electrons are, of course, spin-up and spin-down electrons which couple to the two magnetic fields. This system is a prototype of the quantum spin Hall effect. Kane and Mele first proposed the QSH to exist in graphene with spin-orbit coupling [4]. Shortly afterwards, Bernevig, Hughes, and Zhang proposed a realistic experimental setup to host the QSH effect [5]. Their proposal, which was verified successfully in an

experiment by Koenig's group [6], exploited the spin-orbit coupling and band inversion in a HgTe-CdTe-HgTe heterostructure to create pairs of counter-propogating edge states, which are related to each other by time reversal symmetry. The QSH insulator is a 2D topological insulator. An effective Hamiltonian for the edge state can be written as

$$H = \hbar v_F \sigma_x k_y, \quad (1.2)$$

where the basis is for spin up and spin down and the resulting eigen energies are $E = \pm \hbar v_F k_y$. v_F is the Fermi velocity. This is a massless Dirac Hamiltonian and the spectrum forms a Dirac crossing.

The existence of a surface state can be seen in the following manner. If a topological insulator has a parameter that can be tuned to transition from topologically non-trivial to trivial, the gap of the insulator must close. When a TI is interfaced with a trivial insulator, such as the vacuum, the parameter effectively causes the gap to close at the interface, which gives rise to the gapless surface state.

In principle, by stacking sheets of the 2D TIs and forming a 3D structure, this would be a “weak” topological insulator. The other extension of the TI from 2D to 3D is a “strong” topological insulator. Here, there is also an insulating 3D bulk and the 2D surfaces interfacing the vacuum are similar to the edge state of the 2D TI in their linear dispersing behavior, but they allow momentum to be in any in-plane direction, $\vec{k} = (k_x, k_y) = (k \cos(\theta), k \sin(\theta))$.

The effective low-energy Hamiltonian for these surface states is

$$H = \hbar v_F (\sigma_x k_y - \sigma_y k_x). \quad (1.3)$$

The energies and their respective eigenvectors

$$E = \pm \hbar v_F |\vec{k}| \quad |\psi_{\mathbf{k}}\rangle = \frac{1}{\sqrt{2}} \left(\pm ie^{-i\theta} |\uparrow\rangle + |\downarrow\rangle \right) \quad (1.4)$$

where $|\vec{k}| = \sqrt{k_x^2 + k_y^2}$ and $|\uparrow\rangle(|\downarrow\rangle)$ is the spin up (down) state.

We plot the energy dispersion as a function of k_x and k_y to find a Dirac cone in Fig. 1.2. Any cut taken for some value of $E \neq 0$ produces a circle of states. The eigenstates are always equal superpositions of spin up and down, meaning the spinor is pointing in the x-y plane. The exact direction is dictated by the phase ($ie^{i\theta}$). The spin is pointing at a $\pi/2$ angle from the momentum direction at angle θ , due to the extra i .

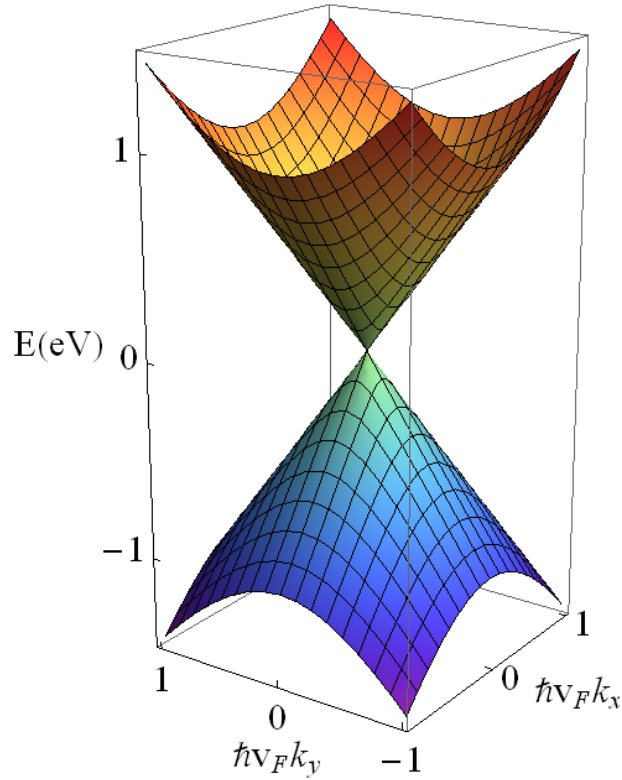


Figure 1.2: Dirac cone dispersion. Energy as a function of momentum, k_x and k_y .

If we look closely at the spin-momentum relationship we see that it is not possible to have arbitrary spin and momentum for an electron on the TI surface. Every direction of momentum is locked to one direction of spin and vice versa. This surface is very different from a normal metal where spin is arbitrary for any momentum and also different from a ferromagnet where the spin of an electron is fixed but can have arbitrary momentum. This coupling along with the relativistic energy dispersion is unique and provides a playground for many exotic properties. These include Majorana fermions[7, 8, 9, 10], barrier transmission [11], spin-currents [12, 13], Aharonov-Bohm oscillations [14], Shubnikov-de Haas oscillations [15], Landau level quantization [16], massive relativistic Dirac fermions [17, 18], and exciton condensation [19].

In 2008, Hassan’s group found a 3D TI in the form of $\text{Bi}_{0.9}\text{Sb}_{0.1}$ by way of ARPES measurements[20]. They found a linear dispersion, Dirac crossing, on the surface and while the bulk has a gapped energy spectrum. This experiment was motivated by several theoretical predictions[21, 22] to find topological insulators in such a 3D binary compound due to the spin-orbit coupling in the material. This led to the discovery of other TIs; Bi_2Se_3 , Bi_2Te_3 , Sb_2Te_3 ; as well as finding topological properties of pure Sb[23, 24, 25, 26, 11]. Since the discovery in 2008, there has been an explosion in research on topological insulators in ArXiv.org, where in years 2009, 2010, 2011, 2012 there were 100, 235, 362, 421 papers on topological insulators, respectively.

This concludes our basic description of the TI. We showed how a 2D TI was produced using two copies of a QH system with opposite simultaneous magnetic fields. We then extended the idea of a 2D TI to 3D “weak” and “strong” TIs. We then examined the surface states to understand the relationship between the spin and momentum as well as potential implications and applications.

1.2 Superconductivity

1.2.1 Measurement

Superconductivity was discovered by Heike Kamerlingh Onnes in 1911. He found that the resistance of mercury drops to zero as the temperature is lowered below 4.2K, a signature of perfect conduction. An immediate question arises, if using a typical voltmeter, as used in physics labs, and Ohm's law, $V = IR$, how can resistance or voltage be measured if they should both be zero? The answer is by using a four point probe. As seen in the diagram in Fig. 1.3, the probe has four point of contact on the material. Two of the connections (1,4) have a constant, controllable current flowing through them. The other two connections (2,3), then probe the sample and measure the voltage drop. The voltage measurement device has a high impedance to minimize any flow from the sample into it. The resulting voltage drop, V , and driving current, I , then give the resistance, $R = V/I$, which along with temperature results in a temperature dependent resistance. An example measurement of $\text{Cu}_2\text{Bi}_2\text{Se}_3$, a new superconducting material based on the topological insulator Bi_2Se_3 , is shown in Fig. 1.3. The plot shows a clear resistance drop at 3.5 Kelvin, the signature of superconductivity.

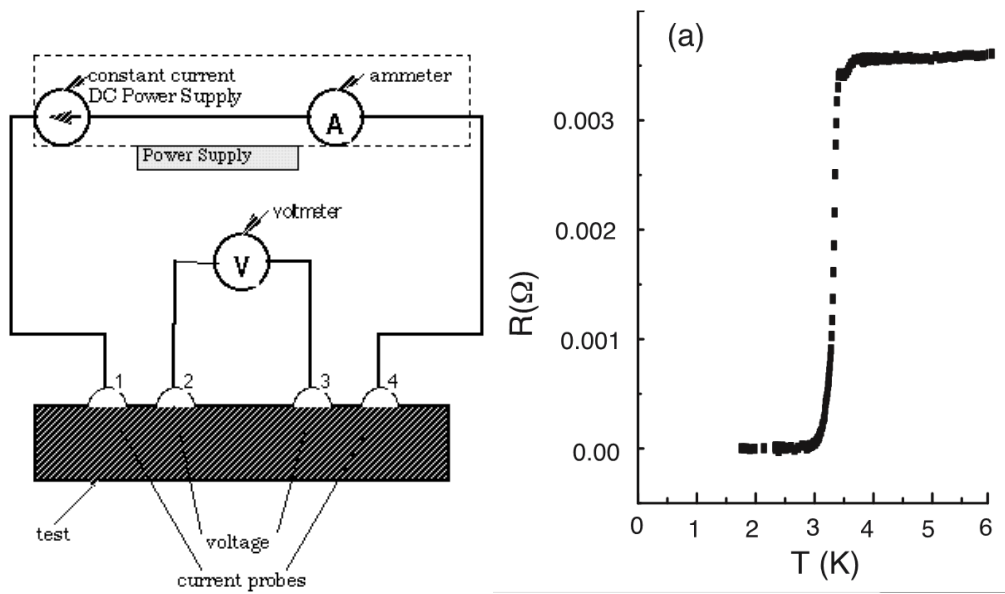


Figure 1.3: (left) Four probe measurement device. Probes 1 and 4 are used to flow a current across a sample while probes 2 and 3 measure the voltage drop across the sample where the current is flowing. (right) Resistance (Ω) vs Temperature (Kelvin) experiment on $\text{Cu}_{2}\text{Bi}_2\text{Se}_3$ from arXiv:1111.5805. The drop in resistance is a signature of superconductivity.

1.2.2 BCS and Bogoliubov Theory

Bardeen, Cooper, and Schreiffer (BCS) came up with a theory to explain the mechanism behind superconductivity. We start with the Hamiltonian that represents a free electron system with two-body electron interactions,

$$H = \sum_{\mathbf{k},\sigma} (\epsilon_{\mathbf{k}} - \mu) c_{\mathbf{k}\sigma}^\dagger c_{\mathbf{k}\sigma} + \sum_{\mathbf{k},\mathbf{k}',\sigma,\sigma'} V_{\mathbf{k},\mathbf{k}'} c_{\mathbf{k}\sigma}^\dagger c_{-\mathbf{k}\downarrow}^\dagger c_{-\mathbf{k}'\uparrow} c_{\mathbf{k}'\downarrow} \quad (1.5)$$

where $c_{\mathbf{k}\sigma}^\dagger$ ($c_{\mathbf{k}\sigma}$) is the electron creation (annihilation) operator, the summations are over spin (σ) and momentum (\mathbf{k}, \mathbf{k}'), $\epsilon_{\mathbf{k}}$ is the free electron energy, $V_{\mathbf{k},\mathbf{k}'}$ is the electron-electron interaction potential. The commutation relations for the fermion creation and annihilation operators are

$$\{c_{\mathbf{k}\sigma}^\dagger, c_{\mathbf{k}'\sigma'}\}_+ = \delta_{\mathbf{k},\mathbf{k}'} \delta_{\sigma\sigma'} \quad (1.6)$$

$$\{c_{\mathbf{k}\sigma}^\dagger, c_{\mathbf{k}'\sigma'}^\dagger\}_+ = \{c_{\mathbf{k}\sigma}, c_{\mathbf{k}'\sigma'}\}_+ = 0. \quad (1.7)$$

In usual electron systems, the Coulomb interaction between electrons is repulsive, but the effective interaction can become attractive. As an electron passes through a lattice of low-mobility nuclei, they actually cause the nuclei to shift causing a phonon interaction with electron. This phonon interaction can be strong enough to effectively attract, $V_{\mathbf{k}\mathbf{k}'} < 0$, two electrons with opposite momenta($\mathbf{k}, -\mathbf{k}$). From the Pauli exclusion principle, we seek a bound pair of electrons with zero total momentum and antisymmetric wave functions known as a Cooper pair. When the electrons pair, they form a condensate of the bosons, which supports superflow that is responsible for the lack of resistance. The electrons near the Fermi energy are most susceptible to pairing, usually when they are within some Debye energy cutoff, $\hbar\omega_D$. One way to describe the superconductor is through a condensate wave function or more precisely the superconducting order parameter, $\Delta(\mathbf{x})$, or $\Delta_{\mathbf{k}}$. This function

is found by a mean field approach to the pairing potential, $V_{\mathbf{k}\mathbf{k}'}$, through the gap equation

$$\Delta_{\mathbf{k}} = \sum_{\mathbf{k}'} V_{\mathbf{k}\mathbf{k}'} c_{-\mathbf{k}'\uparrow} c_{\mathbf{k}'\downarrow} \quad (1.8)$$

reducing the Hamiltonian down to

$$H = \sum_{\mathbf{k},\sigma} (\epsilon_{\mathbf{k}} - \mu) c_{\mathbf{k}\sigma}^\dagger c_{\mathbf{k}\sigma} + \sum_{\mathbf{k}} \Delta_{\mathbf{k}} c_{\mathbf{k}\uparrow}^\dagger c_{-\mathbf{k}\downarrow}^\dagger + h.c. \quad (1.9)$$

To diagonalize this Hamiltonian we change the basis, where rather than restricting ourselves to operators of electrons, we use the Bogoliubov-de Gennes (BdG) transformation to introduce the operators on quasiparticle excitations of particles and holes. This is done through

$$c_{\mathbf{k}\sigma} = \sum_n u_{n\mathbf{k}\sigma} \gamma_{n\mathbf{k}} + v_{n\mathbf{k}\sigma}^* \gamma_{n\mathbf{k}}^\dagger, \quad c_{\mathbf{k}\sigma}^\dagger = \sum_n u_{n\mathbf{k}\sigma}^* \gamma_{n\mathbf{k}}^\dagger + v_{n\mathbf{k}\sigma} \gamma_{n\mathbf{k}} \quad (1.10)$$

where the quasiparticle operators fulfill the anti-commutation relations,

$$\{\gamma_{\mathbf{k}\sigma}^\dagger, \gamma_{\mathbf{k}'\sigma'}\} = \delta_{\mathbf{k}\mathbf{k}'} \delta_{\sigma\sigma'}, \quad \{\gamma_{\mathbf{k}\sigma}, \gamma_{\mathbf{k}'\sigma'}\} = \{\gamma_{\mathbf{k}\sigma}^\dagger, \gamma_{\mathbf{k}'\sigma'}^\dagger\} = 0 \quad (1.11)$$

and allow us to diagonalize the Hamiltonian as

$$H = E_0 + \sum_{\mathbf{k},\sigma} E_{\mathbf{k}} \gamma_{\mathbf{k}\sigma}^\dagger \gamma_{\mathbf{k}\sigma}. \quad (1.12)$$

The quasiparticle (quasihole) wave function is $u_{\mathbf{k}\sigma}$ ($v_{\mathbf{k}\sigma}$). Each electron creation/annihilation operator is a superposition of a quasiparticle creation and annihilation operator. The inverse of this transformation,

$$\gamma_{\mathbf{k}\sigma} = \sum_n u_{n\mathbf{k}\sigma} c_{n\mathbf{k}} - v_{n\mathbf{k}\sigma}^* c_{n\mathbf{k}}^\dagger, \quad \gamma_{\mathbf{k}\sigma}^\dagger = \sum_n u_{n\mathbf{k}\sigma}^* c_{n\mathbf{k}}^\dagger - v_{n\mathbf{k}\sigma} c_{n\mathbf{k}} \quad (1.13)$$

leads to each quasiparticle operator being a superposition of the electron creation operator and the hole creation operator. This physical interpretation allow us to see that there is more to the story than just electrons and holes, but electron-like and hole-like quasiparticle excitations.

The form of the BdG Hamiltonian is

$$H_B = \begin{pmatrix} \epsilon_{\mathbf{k}} - \mu & -\hat{\Delta}_{\mathbf{k}} i\sigma_y \\ \hat{\Delta}_{\mathbf{k}}^\dagger i\sigma_y & \mu - \epsilon_{\mathbf{k}} \end{pmatrix}, \quad (1.14)$$

in the basis of

$$\psi = (u_{\mathbf{k}\uparrow}, u_{\mathbf{k}\downarrow}, v_{\mathbf{k}\uparrow}, v_{\mathbf{k}\downarrow})^T. \quad (1.15)$$

The $\hat{\Delta}_{\mathbf{k}}$ can come in a variety of forms, strictly depending on the pairing symmetry of the superconductor. Generally it can be written as $\Delta_{\mathbf{k}} = \Delta_0(\mathbf{k}) + \mathbf{d}(\mathbf{k}) \cdot \boldsymbol{\sigma}$, while in the BCS case, we focus on $\Delta_{\mathbf{k}} = \Delta_0$, a constant value, representing s-wave orbital pairing[27]. This allows us to find the eigen values of the system,

$$E_{\mathbf{k}} = \pm \sqrt{(\epsilon_{\mathbf{k}} - \mu)^2 + |\Delta|^2}. \quad (1.16)$$

where the spectrum can be seen in the Fig. 1.4. There is now a finite gap of size $2\Delta_0$ seen centered about 0. The gap is a result of the pairing that occurs in the superconductor. These paired states form the condensate and no low energy excitations can exist within the energy gap in the spectrum. In order to have an excitation out of the condensate, you would need $2\Delta_0$ energy to break the pair.

This concludes the introduction to superconductivity. Here, we reviewed the BCS theory on superconductivity to describe the mechanism behind the Cooper pairing, and diagonalizing the BCS Hamiltonian using a mean field approximation and the Bogoliubov-de Gennes Transformation to obtain the energy spectrum. These are the building blocks for understanding the discussions on superconductivity in this thesis.

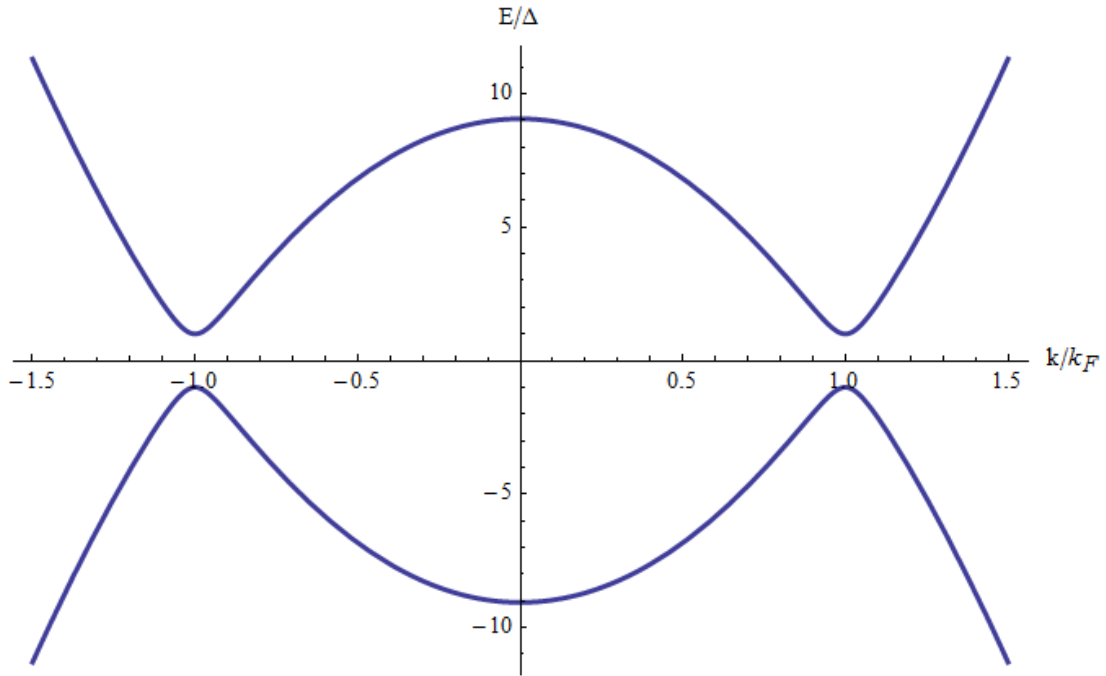


Figure 1.4: Energy spectrum for a BCS superconductor with a gap of $2\Delta_0$ and $\mu/\Delta_0 = 10$.

1.3 Topological Superconductors and Superconductor-Topological Insulator Heterostructures

This section presents two related condensed matter systems that have exotic properties and the motivation for studying them. These are p_x+ip_y superconductors and topological insulator-superconductor heterostructures that host Majorana Fermions. These systems have implications in understanding the role of topology in superconducting systems as well as the possibility of topological quantum computation through the Majorana Fermion. This thesis can be viewed as a systematic deeper study of the latter systems beyond phenomenology.

1.3.1 p_x+ip_y superconductors

One kind of a superconductor that has exotic topological behavior is the p_x+ip_y superconductor. The symmetry of this paired spin-triplet state is of the form $\hat{\Delta}_k = \Delta_0(k_x + ik_y)(\sigma_x + i\sigma_y)$. If we apply this form of the pairing into (1.14), we can diagonalize the BdG Hamiltonian and find eigenvalues of the form

$$E_{\mathbf{k}} = \pm \sqrt{(\epsilon_{\mathbf{k}} - \mu)^2 + (\Delta_0|\mathbf{k}|)^2}. \quad (1.17)$$

This differs from the conventional s-wave eigen energies because the gap term now depends on \mathbf{k} . For values of $\mu \gg 0$, this doesn't effect the spectrum by any more then a negligible change. The noticeable difference, as described Read and Green[28], is when the Fermi energy is reduced to a small value so that $(\epsilon_{\mathbf{k}} - \mu) \rightarrow -\mu$. The spectrum then evolves into a spectrum for a relativistic Dirac fermion with mass μ and speed of light Δ_0 . We also write the BdG equations in the form of

$$Eu = -\mu u + \Delta^* i(\partial_x + i\partial_y)v \quad (1.18)$$

$$Ev = \mu v + \Delta i(\partial_x - i\partial_y)u. \quad (1.19)$$

This is a form of the Dirac equation, and the BdG equations allow for $u = v^*$ through charge conjugation symmetry, where at each \mathbf{k} there is only one excitation mode. This shows that the particles, u , are their own anti-particles, v . When a Dirac fermion has this property, it is a Majorana Fermion. Now consider a setup for this system where the mass term varies spatially through a domain wall ($\mu(x) \propto \text{sign}(x - x_0)$), by tuning the Fermi energy spatially. The requirement for the domain wall is due to the parameter (x) dependent transition from a trivial state superconductor, $\mu < 0$ to a non trivial topological superconductor, $\mu > 0$. One simple model to do this is by $\mu(x) = \mu \sin(2\pi x/L)$. We find a spectrum with linear modes in Fig. 1.5. The linear Majorana modes are found to have chiral propagation and reside at the centers of the domain walls. Another way to host a

Majorana in a p-wave superconductor is by imposing a vortex through a magnetic field, where at the core of the vortex reside the Majorana modes.

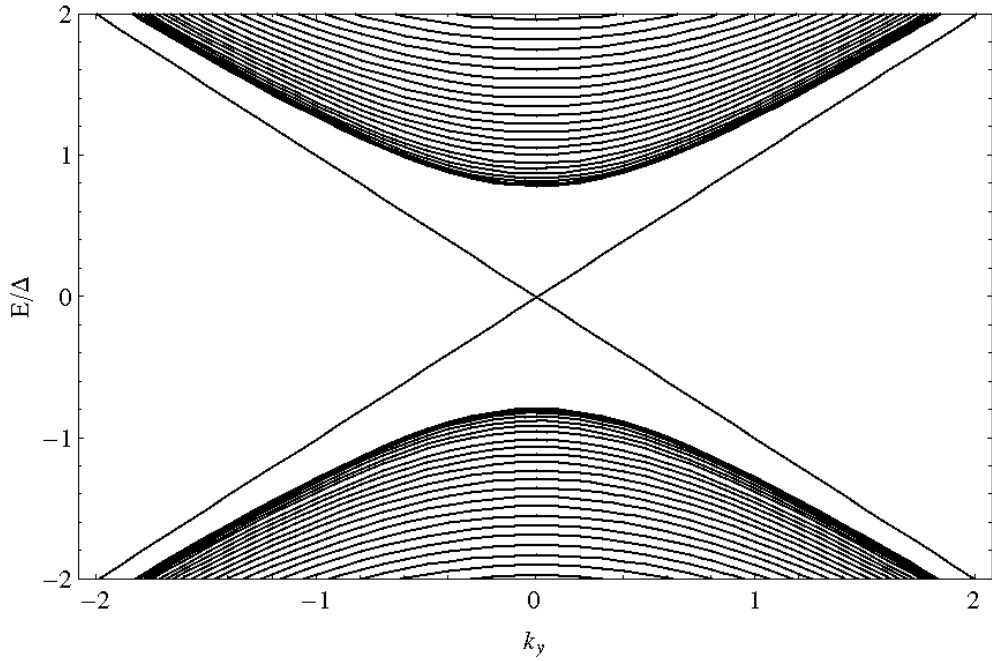


Figure 1.5: Energy spectrum for a $p_x \pm ip_y$ superconductor with a chemical potential domain wall, ensuring linearly dispersing Majorana modes.

1.3.2 Fu-Kane Superconductor/Topological Insulator Model

Fu and Kane were the first to describe the effect of a superconductor in close proximity to the surface of a TI[29]. The TI has the Hamiltonian in the form of $H = v_F(\sigma_x k_y - \sigma_y k_x) - \mu$,

where k_i are the momenta, σ_i are the Pauli spin matrices, and v_F is the Fermi velocity. If an s -wave superconductor is brought to the surface of the TI, Fu-Kane argued that pairing interaction between electrons will be induced on the surface.

This interplay between a TI and S presents many possibilities of various physical effects. This system can be seen to mimic a spin-less $p_x \pm ip_y$ superconductor. Also, under certain conditions where there is a domain wall through the superconductor order parameter, Δ or a magnetic domain wall, it is expected to find a Majorana mode.

Fu-Kane argued that the form of the pairing term is consistent from the S side to the TI side producing the following BdG Hamiltonian

$$\mathcal{H}(\mathbf{k}) = \begin{pmatrix} H(\mathbf{k}) & i\sigma_y \Delta \\ -i\sigma_y \Delta^* & -H^*(-\mathbf{k}) \end{pmatrix} = v_F(\sigma_x k_y - \tau_z \sigma_y k_x) - \tau_z \mu + \tau_y \sigma_y \Delta. \quad (1.20)$$

The spectrum for this system is

$$E = \sqrt{|\Delta|^2 + (v_F |\mathbf{k}| \pm \mu)^2}. \quad (1.21)$$

This system is very analogous to the p-wave superconductor. If we take the limit $\mu \rightarrow 0$ this dispersion is also relativistic where the mass term is Δ and the speed of light is v_F . The $p_x \pm ip_y$ term is responsible for the resulting Majorana mode. In the superconductor-TI heterostructure, this term is also, as we shall see soon, responsible for producing Majorana modes. Since the mass term is parameter, it can be tuned to close the gap at one (or an odd number of points) in the spectrum. The mass term in the S-TI system is the gap parameter, Δ . If we allow Δ to flip sign spatially from a positive value, $|\Delta_0|$, to a negative value, $-|\Delta_0|$, for example through $\Delta(x) = \Delta_0 \tanh(x/L)$, we find a Majorana mode localized at the point where $\Delta(x) = 0$ ($x = 0$) with a linear dispersion that resembles the spectrum of the p-wave superconductor edge-state in Fig. 1.5. One difference is the TI version is four-fold degenerate (particle/hole) of the $E = 0$ mode while the p-wave is

two-fold degenerate (particle/hole). Both systems' linear dispersing states are localized at the domain wall, $x = 0$. This domain wall can be seen as a Majorana wire in the y-direction.

We've now shown some superconductors with exotic properties. We looked at the p-wave superconductor and how it can be tuned to host Majorana modes along with its relativistic Dirac-like energy dispersion. We also looked at the TI-S heterostructure proposed by Fu and Kane which can be tuned to host Majorana modes. These systems are very analogous to each other and show the potential of engineering topological superconductivity using the hybrid structures of TI and s -wave superconductors. The Fu-Kane will be the starting point for latter two thirds of the thesis where we study TI-S structures in greater detail.

Chapter 2: Metal to Topological Insulator Scattering

As described in Chapter 1, the topological insulator (TI) has a unique surface where the spin and momentum of an electron are coupled such that the direction of the spin is equal to the direction of the momentum plus $\pi/2$. That is to say, the electron's wave function, $|\psi_{\mathbf{k}}\rangle$, is presented as

$$|\psi_{\mathbf{k}}\rangle = \pm ie^{-i\theta} |\uparrow\rangle + |\downarrow\rangle \quad (2.1)$$

where $\theta = \arctan(k_y/k_x)$ and $|\uparrow\rangle(|\downarrow\rangle)$ is the spin up (down) state. It's clear that the phase $ie^{-i\theta}$ dictates the direction of the spin in the $x - y$ plane. This special surface is the motivation for the following chapter.

Since we understand the spin-momentum behavior of the electrons that reside on the surface of the TI, a natural extension would be to understanding electrons that scatter off the surface of a TI. Any incoming electron has an interaction with the spin-orbit coupling of the TI. This interaction dictates the resulting spin of the reflected electron.

We find that for a certain critical angle, the electron's spin will always flip, regardless of its state before reflection (i.e. $\alpha|\uparrow\rangle + \beta|\downarrow\rangle \rightarrow \alpha|\downarrow\rangle + \beta|\uparrow\rangle$). This is very different from reflection from a ferromagnetic insulator, where the spin directions of incoming polarized electrons are rotated by the exchange field [30]. This clear difference is unique and allows for an ability to control electrons arbitrarily and perform NOT-gate like operations in binary logic devices, (i.e. TRUE→FALSE and FALSE→TRUE).

To understand this spin dependent interaction we theoretically study a metal-TI interface. The left half, spatially, is a metal and the right half is the TI. An incoming electron comes from the metal side and travels to the TI surface. Since the TI is an insulator, incoming electrons do not propagate through but rather reflect back to the metal side.

We calculate the spin dependent reflection coefficients of the reflected electron. This spin-resolved reflection has implications in using TIs for spintronics because of the ability to invert the spin direction, hence negate the information stored on there.

In addition to the scattering approach, we seek to understand what the combined effect is when a metal and TI are in contact with each other in a different perspective. We do this by using a lattice Green's function method to find the resulting spatially resolved energy spectrum and to calculate the scattering coefficients, also. We find that the local spectrum has two limits depending on the strength of the tunneling between the metal and TI. For good tunneling we find that the metal has a stronger influence on the spectrum near the surface whereas for weak contacts the Dirac cone is clear and well-defined.

Lastly, we discuss the complex energy spectrum of the TI ($E(k_{\text{Real}}, k_{\text{Imag}})$, $k_z \rightarrow k_{\text{Real}} + ik_{\text{Imag}}$). It gives us insight into understanding the behavior of the surface localized wave function of the Dirac electrons.

2.1 Introduction

Recently discovered three dimensional topological band insulators [31, 32, 33], such as $\text{Bi}_{1-x}\text{Sb}_x$ [34] and Bi_2Se_3 [35, 36, 37], are spin-orbit coupled crystal solids with a bulk gap but protected gapless surface states. The low energy excitations at the surface are helical Dirac fermions, i.e., their spin and momentum are entangled (locked) [38]. The charge and spin transport on the surface of a topological insulator are intrinsically coupled [39]. This makes these materials a promising new platform for spintronics. In addition, heterostructures involving topological insulator, superconductor, and/or ferromagnet have been predicted to show a remarkable array of spectral and transport properties (for review see Ref. [40, 41, 42]).

Electronic or spintronic devices based on topological insulators will almost inevitably involve metal as measurement probes or functioning components [43]. This motivates us to study the local spectrum near the interface between a metal (M) and a topological insulator

(TI). For a metal-ordinary semiconductor junction with good contact, it is well known that the metallic Bloch states penetrate into the semiconductor as evanescent waves localized at the interface (for energies within the band gap). Such interface states are known as metal induced gap states (MIGS) [44, 45]. They play an important role in controlling the junction properties, e.g., by pinning the semiconductor Fermi level to determine the Schottky barrier height [46], a key parameter of the junction.

The local spectrum at the M-TI junction is intimately related to the spin-active scattering of electrons at the M-TI interface. In this chapter, we systematically study the evolution of the scattering matrix and the interface spectra with the junction transparency and metal Fermi surface parameters. The scattering matrix [47] we obtain here also forms the basis to investigate the details of the superconducting proximity effect near the superconductor-TI interface [48], which was shown by Fu and Kane to host Majorana fermions [29].

The scattering at the M-TI interface differs significantly from its two dimensional analog, the interface between a metal and a quantum spin Hall (QSH) insulator studied by Tokoyama et al [43]. They predicted a giant spin rotation angle $\alpha \sim \pi$ and interpreted the enhancement as resonance with the one-dimensional helical edge modes. By contrast, for M-TI interface we predict a critical incident angle at which complete spin flipping occurs and the spin rotation angle jumps by π . We will explain its origin, in particular its relation to the surface helical Dirac spectrum, and discuss its spintronic implications.

This chapter is organized as follows. We will first compute the scattering matrix using a $\mathbf{k} \cdot \mathbf{p}$ continuum model by matching the envelope wave functions at the M-TI interface. This simple calculation is easy to understand, and it brings out the main physics of our problem. Along the way, we will discuss the complex band structure of Bi_2Se_3 , which describes the decaying (rather than propagating Bloch wave) solutions of the crystal Hamiltonian. The various caveats of this calculation are then remedied by considering a much more general lattice model. Most importantly, it enables us to track how the scattering matrix and interface spectrum change with interface transparency. It also sheds light on the origin of perfect spin-flip scattering at the critical angle. We will show that the results obtained from

these two complementary methods are consistent with each.

2.2 Model Hamiltonian and Complex Band Structure

We consider Bi_2Se_3 as a prime example of 3D strong topological insulators. Its low energy $\mathbf{k} \cdot \mathbf{p}$ Hamiltonian was obtained by Zhang et al [36],

$$\hat{H}_{TI}(\mathbf{k}) = \epsilon_0(\mathbf{k})\hat{1} + \sum_{\mu=0}^3 d_\mu(\mathbf{k})\hat{\Gamma}_\mu.$$

Here $d_0(\mathbf{k}) = M - B_1 k_z^2 - B_2(k_x^2 + k_y^2)$, $d_1(\mathbf{k}) = A_2 k_x$, $d_2(\mathbf{k}) = A_2 k_y$, $d_3(\mathbf{k}) = A_1 k_z$, and $\epsilon_0(\mathbf{k}) = C + D_1 k_z^2 + D_2(k_x^2 + k_y^2)$. The numerical values of M , A , B , C , D are given in Ref. [36]. We choose the basis $(|+\uparrow\rangle, |+\downarrow\rangle, |- \uparrow\rangle, |- \downarrow\rangle)$, where \pm labels the hybridized p_z orbital with even (odd) parity [36]. The Gamma matrices are defined as $\hat{\Gamma}_0 = \hat{\tau}_3 \otimes \hat{1}$, $\hat{\Gamma}_i = \hat{\tau}_1 \otimes \hat{\sigma}_i$, with $\hat{\tau}_i$ ($\hat{\sigma}_i$) being the Pauli matrices in the orbital (spin) space. The chemical potential of as-grown Bi_2Se_3 crystal actually lies in the conduction band [38]. By hole doping [38] or applying a gate voltage [49], the chemical potential can be tuned inside the gap. The system is well described by H_{TI} (note that energy zero is set as in the middle of the band gap).

In this section, we first adopt a rather artificial model for metals with negligible spin-orbit coupling. It is obtained by turning off the spin-orbit interaction (setting $d_\mu = 0$ for $\mu=1,2,3$) in H_{TI} and shifting the Fermi level into the conduction band. The result is spin-degenerate two-band Hamiltonian

$$\hat{H}_M(\mathbf{k}) = [\epsilon_0(\mathbf{k}) - E_F]\hat{1} + d_0(\mathbf{k})\hat{\Gamma}_0.$$

Its band structure, schematically shown in Fig. 1(b), consists of two oppositely dispersing bands (the solid and dash line). E_F is tuned to be much higher than the band crossing point,

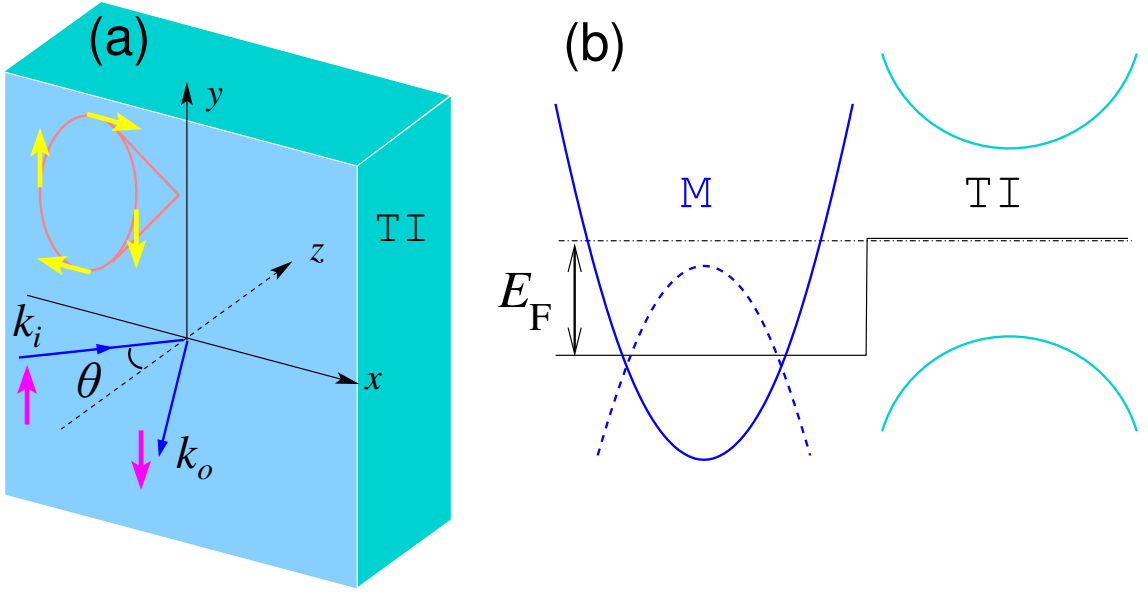


Figure 2.1: (a) Scattering geometry at a metal (M)-topological insulator (TI) interface. (b) Schematic band structure of the metal (modeled by \hat{H}_M) and topological insulator.

so the scattering properties of low energy electrons near the Fermi surface are insensitive to the band crossing at high energies. This claim will be verified later using a more generic model for the metal. A similar model was used in the study of metal-QSH interface [43].

Matching the wave functions of two dissimilar materials (such as Au and Bi_2Se_3) at interface is in general complicated within the $\mathbf{k} \cdot \mathbf{p}$ formalism, because the envelope wave functions on either side are defined using different basis (see Ref. [50] and reference therein). For the particular model H_M , however, such complication is circumvented. Then, the wave functions at the metal-TI interface ($z = 0$) satisfy the Ben-Daniel and Duke boundary condition [51],

$$\hat{\Phi}_M = \hat{\Phi}_{TI}, \quad \hat{v}_M \hat{\Phi}_M = \hat{v}_{TI} \hat{\Phi}_{TI}.$$

Here $\hat{\Phi}_i$ is the four-component wave function, and the velocity matrix $\hat{v}_i = \partial \hat{H}_i / \partial k_z$, $i \in$

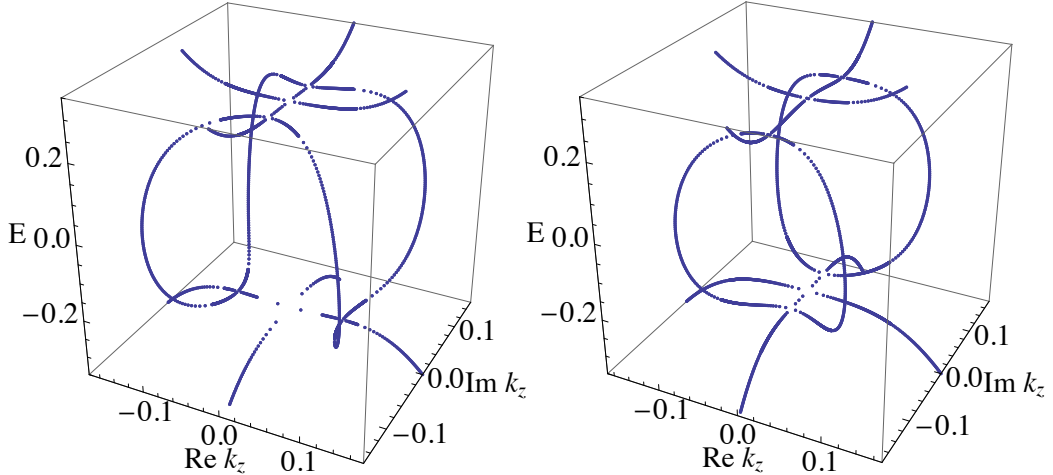


Figure 2.2: The complex band structure of topological insulator described by $\hat{H}_{TI}(\mathbf{k})$ for $k_y = 0$, $k_x = 0.02$ (left) and 0.04 (right). E is measured in eV, and k in \AA^{-1} . Subgap states with complex k_z represent evanescent waves. The topology of real lines [1] changes as k_x is increased.

$\{M, TI\}$. Such boundary condition assumes good atomic contact between two materials.

We are interested in energies below the band gap of TI, so $\hat{\Phi}_{TI}$ is evanescent in nature and only penetrates into TI for a finite length. Such localized (surface or interface) states inside topological insulator can be treated within the $\mathbf{k} \cdot \mathbf{p}$ formalism using the theory of *complex band structures*, pioneered by Kohn [52], Blount [53], and Heine [1] et al. The main idea is to allow the crystal momentum to be complex and analytically continue $H_{TI}(\mathbf{k})$ to the complex \mathbf{k} plane. While the extended Bloch waves are the eigen states of $H_{TI}(\mathbf{k})$ for real \mathbf{k} , eigen functions of $H_{TI}(\mathbf{k})$ for complex \mathbf{k} describe localized states. Together they form a complete basis to describe crystals of finite dimension.

In our scattering problem, we have to find all eigen states of $H_{TI}(\mathbf{k})$ with energy E and wave vector $\mathbf{k} = (k_x, k_y, \tilde{k}_z)$, where k_x and k_y are given and real, but \tilde{k}_z is complex and unknown. For a general $\mathbf{k} \cdot \mathbf{p}$ Hamiltonian such as \hat{H}_{TI} , we follow Chang and Schulman

[54] to rewrite it as

$$\hat{H}_{TI} = \hat{h}_0(k_x, k_y) + \hat{h}_1 \tilde{k}_z + \hat{h}_2 \tilde{k}_z^2,$$

where $\hat{h}_1 = A_1 \hat{\Gamma}_3$, and $\hat{h}_2 = -B_1 \hat{\Gamma}_0$. Then the eigen equation $(\hat{H}_{TI} - E\hat{1})\hat{\phi} = 0$ can be reorganized into an eigen value problem for \tilde{k}_z ,

$$\begin{pmatrix} 0 & 1 \\ -\hat{h}_2^{-1}(\hat{h}_0 - E\hat{1}) & -\hat{h}_2^{-1}\hat{h}_1 \end{pmatrix} \begin{pmatrix} \hat{\phi} \\ \hat{\phi}' \end{pmatrix} = \tilde{k}_z \begin{pmatrix} \hat{\phi} \\ \hat{\phi}' \end{pmatrix}.$$

Then all possible values of \tilde{k}_z can be obtained for given incident parameter E , k_x , and k_y . For the anisotropic Dirac Hamiltonian $H_{TI}(\mathbf{k})$, the energy eigenvalues can be obtained analytically [55], which allows for an analytical solution of the complex band structure.

For E within the gap, there are in general 4 pairs of complex solution of \tilde{k}_z , for if \tilde{k}_z is a solution so is \tilde{k}_z^* . We label those with positive imaginary parts with $\{\tilde{k}_z^\nu\}$, and the corresponding wave function $\{\hat{\phi}^\nu\}$, $\nu = 1, 2, 3, 4$. They are decaying solutions in the half space $z > 0$. In our model, \tilde{k}_z turns out to be doubly degenerate, as shown in Fig. 2. The wave function inside TI ($z > 0$) then has the form

$$\hat{\Phi}_{TI} = \sum_\nu t_\nu e^{i\tilde{k}_z^\nu z} \hat{\phi}_\nu.$$

2.3 Scattering Matrix from Wave-Function Matching

To set the stage for discussing scattering off a topological insulator, it is instructive to recall the generic features of elastic scattering of electrons by a heavy ion with spin-orbit interaction. This classical problem was solved by Mott, and known as *Mott scattering*. The

scattering matrix has the general form [56]

$$\hat{S}_{Mott} = u\hat{1} + w\hat{\sigma} \cdot (\mathbf{k}_i \times \mathbf{k}_o),$$

where \mathbf{k}_i and \mathbf{k}_o are the incident and outgoing momentum respectively, $\hat{\sigma}$ is the Pauli matrix, and u, w depend on the scattering angle. It is customary to define the spin-flip amplitude $f = S_{21}$, and spin-conserving amplitude $g = S_{11}$. Both f and g are complex numbers, their relative phase defines the *spin rotation angle* $\alpha = \text{Arg}(g^*f)$. One immediately sees that for back scattering, $\hat{S}_{Mott} = u\hat{1}$, so there is no spin flip, $f = 0$. As we will show below, this also holds true for scattering off TI.

Now consider an electron coming from the metal with momentum \mathbf{k} incident on the M-TI interface located at $z = 0$, as schematically shown in Fig. 1(a). We assume the interface is translationally invariant, so the transverse momentum $\mathbf{k}_{\parallel} = (k_x, k_y)$ is conserved, and the energy E of the electron lies within the band gap of TI. Then, only total reflection is possible, but the spin-orbit coupling inside TI acting like a \mathbf{k} -dependent magnetic field rotates the spin of the incident particle. The scattering (reflection) matrix has the form

$$\hat{S}(\mathbf{k}) = \begin{pmatrix} g & \bar{f} \\ f & \bar{g} \end{pmatrix},$$

where $|g|^2 + |f|^2 = 1$. Our goal is to find the dependence of the scattering amplitudes f, g on \mathbf{k} , or equivalently, on energy E and incident angle θ . From time-reversal symmetry, $\bar{f}(E, \theta) = f(E, -\theta)$ and $\bar{g}(E, \theta) = g(E, -\theta)$. We shall show that $f(\mathbf{k}_{\parallel}) = -f(-\mathbf{k}_{\parallel})$, $g(\mathbf{k}_{\parallel}) = g(-\mathbf{k}_{\parallel})$. So f is an odd function of θ , while g is even in θ . Since our problem can be viewed as coherent multiple scattering from a lattice array of Mott scatters occupying half the space, we will refer to spin-active scattering at the metal-TI interface as Mott scattering.

Consider a spin up electron from the conduction band of the metal with momentum \mathbf{k} and energy $E = \epsilon_0(\mathbf{k}) - E_F - d_0(\mathbf{k})$ lying within the band gap of TI. The wave function

inside the metal ($z < 0$) has the form

$$\hat{\Phi}_M = (r_1 e^{-ik'_z z}, r_2 e^{-ik'_z z}, e^{ik_z z} + r_3 e^{-ik_z z}, r_4 e^{-ik_z z})^T,$$

up to the trivial $e^{i(k_x x + k_y y)}$ and renormalization factor. Here $k_z = \hat{z} \cdot \mathbf{k}$, and $\{r_i\}$ are the reflection amplitudes. We identify the spin flip amplitude $f = r_4$ and the spin-conserving amplitude $g = r_3$. Note that there is no propagating mode at energy E available in the valence band for the reflected electron. So k'_z has an imaginary component. At such energy, there is no propagating mode available in TI. We have discussed the evanescent wave function $\hat{\Phi}_{TI}$ in the previous section. With $\hat{\Phi}_M$ and $\hat{\Phi}_{TI}$, we solve the boundary condition at $z = 0$ to obtain r_ν, t_ν and the scattering matrix S .

Fig. 3 shows the magnitude and phase of f and g versus the incident angle θ for $E = 0.1\text{eV}$, with E_F set to be 0.28eV . At normal incidence, $\theta = 0$, spin flip scattering is forbidden as in the single-ion Mott scattering. With increasing θ the magnitude of g drops continuously. At a critical angle θ_c , $|g|$ drops to zero and we have perfect (100%) spin flip reflection. At the same time, the spin rotation angle α (the relative phase between f and g) jumps by π .

It is tantalizing to think of what happens at θ_c as resonant scattering with the helical surface mode of the TI. This however is problematic. We are considering good contacts at which the wave functions of the two materials hybridize strongly. Surface mode is preempted by MIGS. Indeed, we checked that the corresponding critical transverse momentum k_{\parallel} depends only weakly on E . This is at odds with the linear dispersion of the TI surface mode, $E = A_2 k_{\parallel}$ [36]. To gain better understanding, we now switch to a lattice model to systematically study the role of interface transparency and metal Fermi surface parameter (E_f, k_f, v_f) on the scattering matrix.

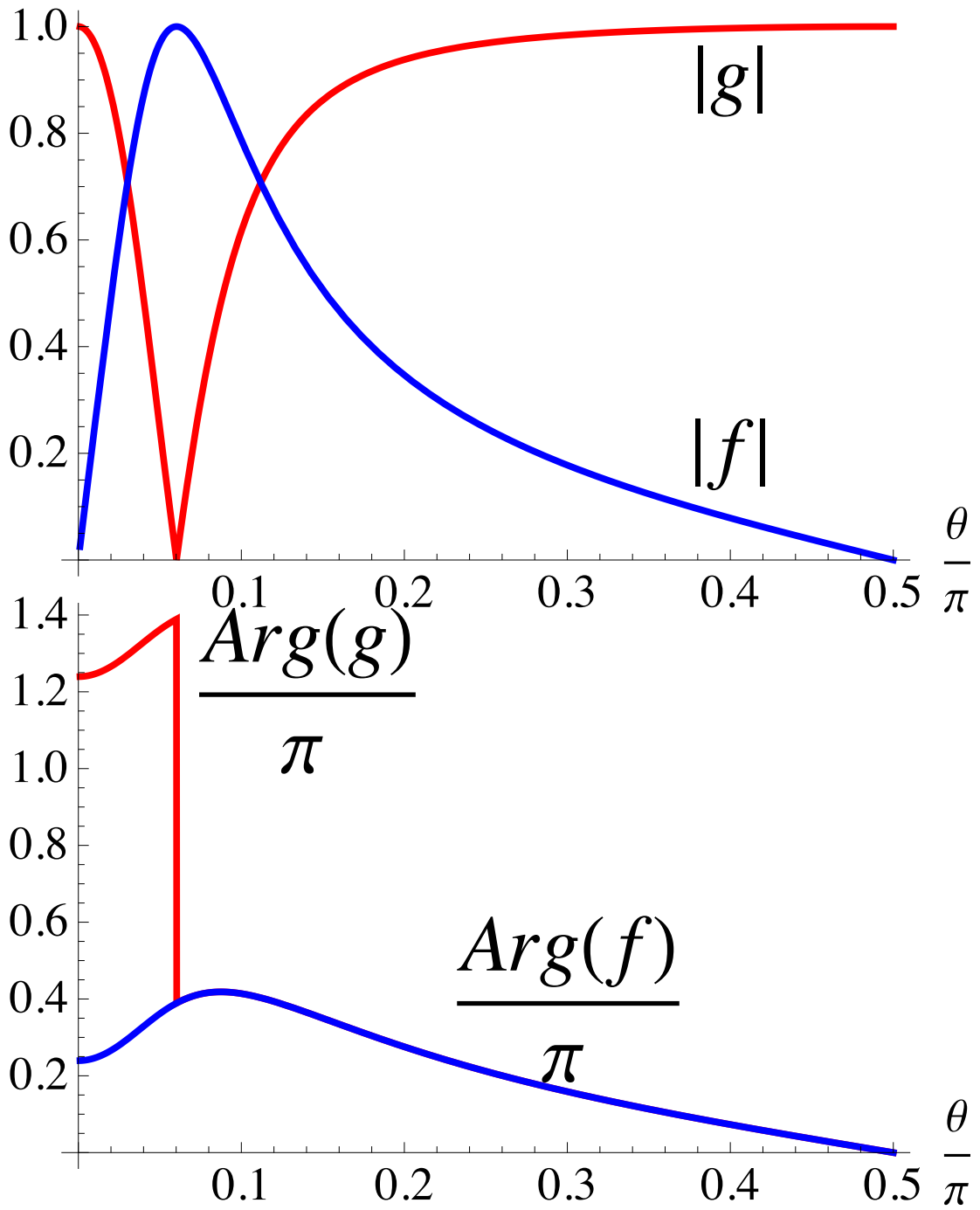


Figure 2.3: The magnitudes (upper panel) and the phases (lower panel) of the spin-flip amplitude f and spin-conserving amplitude g versus the incident angle θ . $E = 0.1\text{eV}$, $E_F=0.28\text{eV}$. $|g|^2 + |f|^2 = 1$. $\text{Arg}(g)$ and $\text{Arg}(f)$ are shifted upward by π for clarity.

2.4 Interface Spectrum and Scattering Matrix from Lattice Green Function

We consider a simple lattice model for the M-TI junction. The topological insulator is modeled by a tight binding Hamiltonian on cubic lattice,

$$\begin{aligned}\mathcal{H}_R = & \sum_{k_+,n} \left\{ \hat{\psi}_{k_+,n}^\dagger (b_1 \hat{\Gamma}_0 - i \frac{a_1}{2} \hat{\Gamma}_3) \hat{\psi}_{k_+,n+1} + h.c. \right. \\ & \left. + \hat{\psi}_{k_+,n}^\dagger \left[d(k_+) \hat{\Gamma}_0 + a_2 (\hat{\Gamma}_1 \sin k_x + \hat{\Gamma}_2 \sin k_y) \right] \hat{\psi}_{k_+,n} \right\}.\end{aligned}$$

Here $\hat{\psi} = (\psi_{+\uparrow}, \psi_{+\downarrow}, \psi_{-\uparrow}, \psi_{-\downarrow})^T$ is the annihilation operator, $d(k_+) = M - 2b_1 + 2b_2(\cos k_x + \cos k_y - 2)$ with k measured in $1/a$. The cubic lattice consists of layers of square lattice stacked in the z direction, n is the layer index, and k_+ is the momentum in the xy plane. The isotropic version of \mathcal{H}_R , with $a_1 = a_2$, $b_1 = b_2$, was studied by Qi et al as a minimal model for 3D topological insulators [55]. To mimic Bi₂Se₃, we set the lattice spacing $a = 5.2\text{\AA}$, which gives the correct unit cell volume, and $a_i = A_i/a$, $b_i = B_i/a^2$ for $i = 1, 2$. Although a crude caricature of the real material, \mathcal{H}_R yields the correct gap size and surface dispersion, it also reduces to the continuum $\mathbf{k} \cdot \mathbf{p}$ Hamiltonian \hat{H}_{TI} in the small k limit, aside from the topologically trivial $\epsilon_0(\mathbf{k})$ term.

As a generic model for metal, we consider a single band tight binding Hamiltonian on cubic lattice,

$$\mathcal{H}_L = \sum_{k_+,n,\sigma} [h(k_+) n_{k_+,n,\sigma} - t_M \phi_{k_+,n,\sigma}^\dagger \phi_{k_+,n+1,\sigma} + h.c.]$$

where $h(k_+) = -2t_M(\cos k_x + \cos k_y) - \mu_M$. The Fermi surface parameters of the metal can be varied by tuning t_M and μ_M . The metal occupies the left half space, $n \leq 0$, and the TI occupies the right half space $n \geq 1$. The interface domain consists of layer $n = 0, 1$. The

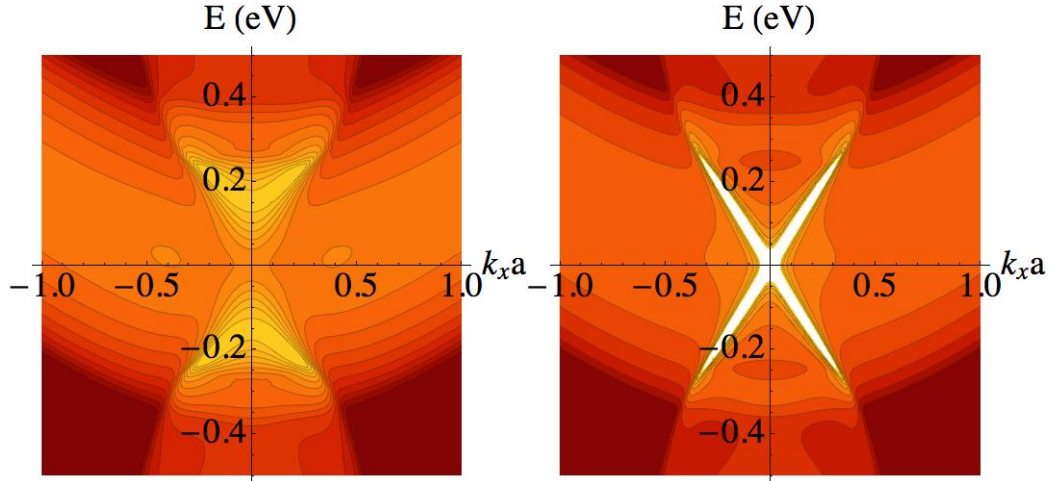


Figure 2.4: The spectral function $N(E, k_x, k_y = 0)$ at the interface of metal and topological insulator. Left: good contact, $J = t_M$, showing the continuum of metal induced gap states. Right: poor contact with low transparency, $J = 0.2t_M$, showing well defined Dirac spectrum as on the TI surface. $t_M = 0.18\text{eV}$, $\mu_M = -4t_M$, a is lattice spacing.

coupling between metal and TI is described by hopping,

$$\mathcal{H}_{LR} = - \sum_{k_+, \ell, \sigma} J_\ell \psi_{k_+, n=1, \ell, \sigma}^\dagger \phi_{k_+, n=0, \sigma} + h.c.$$

J_ℓ is the overlap integral between the p -orbital $\ell = \pm$ of TI and the s -like orbital of metal. For simplicity, we assume J_ℓ is independent of spin. Then, $J_+ = -J_- = J$. J can be tuned from weak to strong. Small J mimics a large tunneling barrier between M and TI, and large J (comparable to t_M or B_2) describes a good contact.

The lattice Green function of the composite system is computed via standard procedure by introducing the inter-layer transfer matrix and the method of interface Green function matching [57]. Fig. 4 shows two examples of the local spectral function (momentum-resolved

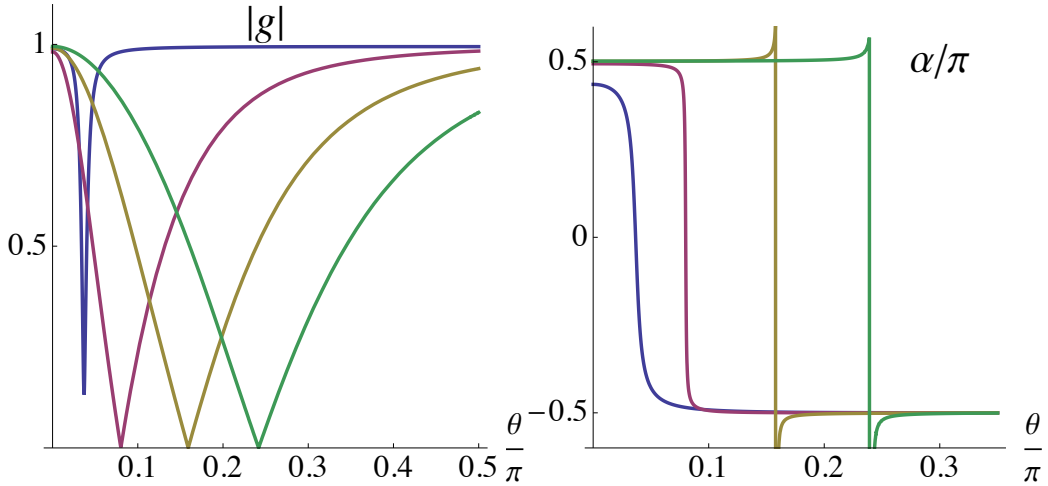


Figure 2.5: The spin-conserving reflection amplitude $|g|$ and spin rotation angle α versus the incident angle θ for increasing contact transparency, $J/t_M = 0.25, 1, 1.5, 2$ (from left to right). $t_M = 0.18\text{eV}$, $\mu_M = -4t_M$, $E = 0.05\text{eV}$, $k_y = 0$. $|f|^2 = 1 - |g|^2$.

density of states) at the interface,

$$N(E, k_+) = - \sum_{n=0,1} \text{ImTr} \hat{\mathcal{G}}(E, k_+)_{n,n},$$

where $\hat{\mathcal{G}}(E, k_+)_{n,n'}$ is the local Green function at the interface with $n, n' = 0, 1$, and the trace is over the spin and orbital space. In the tunneling (weak coupling, small J) limit, the interface spectrum includes a sharply defined Dirac cone as on the surface of TI. As J is increased, the linearly dispersing mode becomes ill defined and eventually replaced by a continuum of metal induced gap states.

Once the lattice Green function is known for given incident E and k_{\parallel} , the scattering

(reflection) matrix can be constructed from $\hat{\mathcal{G}}$ by [57],

$$\hat{S}(E, k_+) = \hat{\mathcal{G}}(E, k_+)_{0,0} g_M^{-1}(E, k_+) - \hat{1}$$

where g_M is the spin-degenerate bulk Green function of metal. Fig. 5 shows the evolution of $|g(\theta)|$ and $\alpha(\theta)$ for increasing J , where a level broadening of $E/10$ is used. Most importantly, we observe that the existence of a critical angle θ_c , where complete spin-flip occurs and α jumps by π , is a robust phenomenon. It is independent of the details of the contact, the metal Fermi surface, or other high energy features in the band structure.

To understand the perfect spin flip, we first focus on the tunneling limit, $J \ll t_M$. In this limit, the local spectrum at layer $n = 1$ as shown in the right panel of Fig. 4 approaches the TI surface spectrum, namely the helical Dirac cone. An incident up spin tunneling across the barrier will develop resonance with the helical mode, which is a quasi-stationary state with long life time, if its momentum and energy satisfy $k_{\parallel} = E/A_2$. Moreover, it has to flip its spin, since only down spin can propagate in the k_x direction (suppose $k_y = 0$). The π jump in the phase shift is also characteristic of the resonance. Indeed, we have checked that precisely at θ_c the resonance criterion, $k_f \sin \theta_c = E/A_2$, is met. We also varied μ_M for fixed J and t_M , bigger μ_M yields a bigger Fermi surface and a smaller θ_c . This is consistent with the resonance criterion above.

As J is increased, the width of the resonance grows and eventually it is replaced by a broad peak (dip) in $|f|$ ($|g|$), but the vanishing of $|g|$ and π shift in α at θ_c persist to good contacts, even though in this limit the interface is flooded by MIGS (left panel of Fig. 4) and bears little resemblance to the Dirac spectrum. With all other parameters held fixed, θ_c increases with J . Qualitatively, coupling to TI renormalizes the metal spectrum near the interface, producing a smaller effective k_f (hence a larger θ_c) compared to its bulk value. It is remarkable that perfect spin flip at the critical angle persists all the way from poor to good contacts. Indeed, the main features observed here for good contacts using the lattice model agree well with the results obtained in previous section by wave function

matching.

2.5 Discussions

We now discuss the experimental implications of our results. The M-TI interface spectrum can be measured by ARPES (or scanning tunneling microscope) experiments on metal film coated on a topological insulator. Our results also suggest that a topological insulator can serve as a perfect mirror to flip the electron spin in metal. Such spin-active scattering at the M-TI interface may be exploited to make novel spintronic devices. The magnitude of g or f can be measured by attaching two ferromagnetic leads to a piece of metal in contact with TI, forming a multi-terminal device. One of the ferromagnetic leads produces spin-polarized electrons incident on the M-TI interface at some angle, while the other lead detects the polarization of reflected electron, as in a giant magneto-resistance junction. The spin rotation angle α can be measured indirectly by comparing the predicted current-voltage characteristics of M-TI-M or Superconductor-TI-Superconductor junctions, which are sensitive the phase shift α . It can also be inferred from the spin transport in a TI-M-TI sandwich, as discussed for QSH insulator in Ref. [43]. Detailed calculations of the transport properties of these structured, using the scattering matrix obtained here, will be subjects of future work.

Chapter 3: Superconducting Proximity Effect

In the first chapter we described the topological insulator and it's novel features. We also described the exotic p -wave superconductor and along with the topological insulator in proximity to an s -wave superconductor. We showed that these systems are topological in the sense that there exist with gap-less modes localized near certain boundaries. These edge states have linear dispersions.

In this chapter we focus on the superconductor-topological insulator heterostructure. This structure is predicted by Fu and Kane to be a host to a Majorana fermion under certain conditions. Our focus is not on the phenomenological properties of the Majorana regime, but rather to understand the behavior of the system in a more realistic fashion. We set up the Bogoliubov-de Gennes model for a TI and a superconductor to calculate the eigensystem in a recursive, self-consistent manner. The eigen energies and wave functions provide the framework we need to calculate several quantitative properties. These include order parameter, $\Delta(z)$, spatially resolved spectral function, $A(z, k, \epsilon)$, local density of states, $N(z, \epsilon)$. In addition we also find singlet ($F_{\uparrow\downarrow}(k, z)$) and triplet ($F_{\uparrow\uparrow}(k, z)$ $F_{\downarrow\downarrow}(k, z)$) pairing correlations. We show that the energy spectrum does indeed host sub-gap states as predicted by Fu-Kane with renormalized parameters. We also find triplet correlations, exhibiting $p_x + ip_y$ behavior, consistent with previous studies of a similar system.

3.1 Introduction

Fu and Kane showed that at the interface between a three-dimensional topological band insulator (TI) and an s -wave superconductor (S) forms a remarkable two-dimensional non-Abelian superconductor [58]. It hosts Majorana zero modes at vortex cores, as in a $p_x + ip_y$ superconductor [59], but respects time-reversal symmetry. As argued in Ref. [58], the

presence of superconductor induces a pairing interaction between the helical Dirac fermions at the surface of the topological insulator, and gaps out the surface spectrum. Then, the interface can be modeled elegantly by a simple matrix Hamiltonian in Nambu space (we follow the convention of Ref. [60]),

$$H_{FK}(\mathbf{k}) = \begin{pmatrix} h_s(\mathbf{k}) & i\sigma_y\Delta_s \\ -i\sigma_y\Delta_s^* & -h_s^*(-\mathbf{k}) \end{pmatrix}, \quad (3.1)$$

where $\mathbf{k} = (k_x, k_y)$ is the two-dimensional momentum in the interface plane, σ_i are the Pauli matrices, $h_s(\mathbf{k})$ is the surface Hamiltonian for the topological insulator describing the helical Dirac fermions [60, 41],

$$h_s(\mathbf{k}) = -\mu_s + v_s(\sigma_x k_y - \sigma_y k_x). \quad (3.2)$$

Fu and Kane also proposed to use S-TI proximity structures to generate and manipulate Majorana fermions which obey non-Abelian statistics and are potentially useful for fault tolerant quantum computation [58]. This proposal and a few others that followed based on superconductor-semiconductor heterostructures [61, 62, 63, 64, 65] have revived the interest in superconducting proximity effect involving insulating/semiconducting materials with spin-orbit coupling. More complex S-TI proximity structures with ferromagnets [66, 67] or unconventional superconductors [68] have been investigated.

Experiments are beginning to realize various S-TI proximity structures [69, 70, 71]. In light of these developments, it is desirable to understand to what extent the effective model H_{FK} holds, and what are the values of (Δ_s, μ_s, v_s) for given materials. Answering these questions is crucial for future experiments designed to probe and manipulate Majorana fermions. As a first step in this direction, Stanesco et al considered a microscopic lattice model for the TI-S interface [48]. In this model, TI and S are described by a tight binding Hamiltonian defined on the diamond and hexagonal lattice respectively. The two materials

are coupled by tunneling term in the Hamiltonian. These authors found that for small \mathbf{k} , $H_{FK}(\mathbf{k})$ is valid but its parameters are significantly renormalized by the presence of the superconductor. This is supported by leading order perturbation theory in the weak coupling (tunneling) limit. They also discussed the induced p -wave correlation within the framework of perturbation theory. The p -wave correlation has also been noted in an analogous proximity structure in two dimension between a quantum spin Hall insulator and a superconductor [72].

In this work, we consider S-TI proximity structures where S and TI are *strongly* coupled to each other, rather than being separated by a tunneling barrier. This is the desired, presumably the optimal, configuration to realize the Fu-Kane proposal, e.g. to achieve maximum value of Δ_s in H_{FK} for given superconductor. In the strong coupling limit, the modification of superconductivity by the TI becomes important. This includes the suppression of the superconducting order parameter, the induction of triplet pair correlations by spin-active scattering at the interface, and the formation of interface states below the bulk superconducting gap. In order to accurately answer questions raised in the preceding paragraph for strongly coupled S-TI structures, one has to self-consistently determine the spatial profile of the order parameter near the interface.

Our work is also motivated by recent experimental discovery that Copper-doped topological insulator $\text{Cu}_x\text{Bi}_2\text{Se}_3$ becomes superconducting at a few Kelvins [73, 74, 75]. It seems possible then to combine such superconductors with topological insulator Bi_2Se_3 to achieve strong proximity coupling. We set up microscopic, continuum models for the S-TI structures and solve the result Bogoliubov-de Gennes (BdG) equation numerically. We first compute the superconducting order parameter as a function of the distance away from the interface. We then verify the validity of the Fu-Kane effective model and extract its parameters from the low energy sector of the energy spectrum. The emergence of H_{FK} will be viewed as the result of the “inverse proximity effect”, namely strong modification of superconductivity by the presence of TI. This is in contrast to the previous viewpoint of pairing between surface Dirac fermions, which is a more proper description in the tunneling limit. The spectral

weight of these low energy modes (with energy below the bulk superconducting gap) are shown explicitly to peak near the interface but penetrate well into the superconductor. We will also show analytically that the induced triplet pair correlations are of $p_x \pm ip_y$ orbital symmetry, and systematically study their spatial and momentum dependence. Our results connect the phenomenological theory of Fu and Kane [58] to real materials. Our results for continuum models and strong coupling limit are also complementary to the results of Stanescu et al [48] for lattice models and tunneling limit.

In what follows, we first outline the formulation of the problem and then present the main results. Technical details on numerically solving the BdG equation are relegated to the appendix.

3.2 Model and Basic Equations

The band gaps of topological insulators are much larger than the superconducting gap of all weak coupling s -wave superconductors. For the purpose of studying the proximity effect between such superconductors and topological insulators, it is sufficient to describe the topological insulator using the low energy effective $\mathbf{k} \cdot \mathbf{p}$ Hamiltonian. Following Zhang et al [76], we model Bi₂Se₃ by

$$H_{TI}(\mathbf{k}) = \begin{pmatrix} M(\mathbf{k}) & 0 & A_1 k_z & A_2 k_- \\ 0 & M(\mathbf{k}) & A_2 k_+ & -A_1 k_z \\ A_1 k_z & A_2 k_- & -M(\mathbf{k}) & 0 \\ A_2 k_+ & -A_1 k_z & 0 & -M(\mathbf{k}) \end{pmatrix} - \mu \hat{I}. \quad (3.3)$$

Here $k_{\pm} = k_x \pm ik_y$, $M(\mathbf{k}) = M - B_1 k_z^2 - B_2(k_x^2 + k_y^2)$, and \hat{I} is 4×4 unit matrix. The numerical values of the parameters are obtained from first principle calculations [76, 77], $M = 0.28$ eV, $A_1 = 2.2$ eVÅ, $A_2 = 4.1$ eVÅ, $B_1 = 10$ eVÅ², $B_2 = 56.6$ eVÅ². We work in basis $\{|1\uparrow\rangle, |1\downarrow\rangle, |2\uparrow\rangle, |2\downarrow\rangle\}$, where 1 (2) labels the $P1_z^+$ ($P2_z^+$) orbital [76]. Note that

we have neglected the unimportant diagonal term $\epsilon_0(\mathbf{k})$ in Ref. [76] which only slightly modifies the overall curvature of the band dispersion. We also keep the chemical potential μ as a tuning parameter.

We consider a simple model of superconductor derived from a metallic state obtained by turning off the spin-orbit coupling ($A_1 = A_2 = 0$) in H_{TI} and tuning the Fermi level well into the conduction band [78]. The metal Hamiltonian

$$H_M(\mathbf{k}) = \text{diag}[M(\mathbf{k}), M(\mathbf{k}), -M(\mathbf{k}), -M(\mathbf{k})] - E_f \hat{I}, \quad (3.4)$$

with $E_f > M$. This mimics electron-doping the topological insulator [74] or equivalently electrochemically shifting its chemical potential by applying a gate voltage [49]. As shown in Fig. 3.1, the valence band (band 1 with dispersion $M(\mathbf{k}) - E_f$) is well below the Fermi level and remains inert as far as superconductivity is concerned. Next, within the framework of Bardeen-Cooper-Schrieffer theory, we assume attractive interaction between the electrons in the conduction band (band 2) near the Fermi surface described by the reduced Hamiltonian,

$$H_{int} = \sum_{\mathbf{k}} \psi_{2\uparrow}^\dagger(\mathbf{k}) \psi_{2\downarrow}^\dagger(-\mathbf{k}) \Delta + h.c. \quad (3.5)$$

Here Δ is the superconducting order parameter, $\psi_{l\sigma}^\dagger$ is the electron creation operator for orbital $l = 1, 2$ and spin $\sigma = \uparrow, \downarrow$. The superconductor is then described by

$$H_S = \sum_{\mathbf{k}, l, \sigma} \psi_{l\sigma}^\dagger(\mathbf{k}) H_M(\mathbf{k})_{l\sigma, l\sigma} \psi_{l\sigma}(\mathbf{k}) + H_{int}. \quad (3.6)$$

Note that H_S and H_{TI} are in the same basis.

This model can serve as a generic model for *s*-wave superconductors with negligible spin-orbital coupling. Whether it can actually describe the superconductor $\text{Cu}_x\text{Bi}_2\text{Se}_3$ has to be settled by future experiments. The transition temperature of $\text{Cu}_x\text{Bi}_2\text{Se}_3$ at optimal

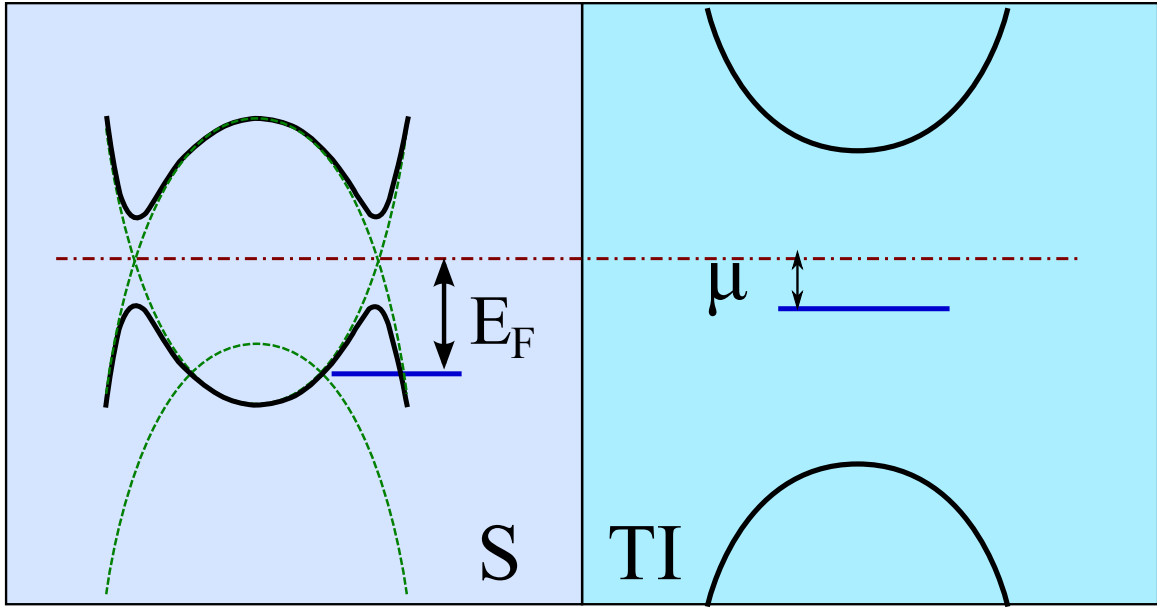


Figure 3.1: Schematic (not to scale) band diagrams in a superconductor-topological insulator (S-TI) proximity structure. E_f is the Fermi energy of the metal described by H_M measured from the band crossing point. μ is the chemical potential of TI measured from the band gap center. The superconducting gap is much smaller than the band gap of TI.

doping $x = 0.12$ is $T_c = 3.8\text{K}$, which corresponds to a zero temperature superconducting gap $\Delta \sim 0.6\text{meV}$ [73, 74, 75]. The Fermi level is 0.25eV above the bottom of the conduction band, and the Fermi wave vector $k_f \sim 0.12\text{\AA}^{-1}$. The pairing symmetry of $\text{Cu}_x\text{Bi}_2\text{Se}_3$ is to our best knowledge is unknown at present (it appears to be fully gapped from the specific heat measurement [75] and might be a topological superconductor [74]). If it turns out to be a conventional s -wave superconductor, its mains features will be captured by H_S above with suitable choice of E_f and Δ .

Now consider a proximity structure consisting of a superconductor at $z < d$ and a topological insulator at $z > d$ (Fig. 3.1). The interface at $z = d$ is assumed to be specular, so the momentum $\mathbf{k}_{\parallel} = (k_x, k_y)$ parallel to the interface is conserved. The Hamiltonian for

the whole system

$$\begin{aligned}
\mathcal{H} = & \int d\mathbf{k}_\parallel dz \left\{ \sum_\sigma \psi_{1\sigma}^\dagger(\mathbf{k}_\parallel, z) [h_0 - \mu(z)] \psi_{1\sigma}^\dagger(\mathbf{k}_\parallel, z) \right. \\
& - \sum_\sigma \psi_{2\sigma}^\dagger(\mathbf{k}_\parallel, z) [h_0 + \mu(z)] \psi_{2\sigma}^\dagger(\mathbf{k}_\parallel, z) \\
& + \Delta(z) \psi_{2\uparrow}^\dagger(\mathbf{k}_\parallel, z) \psi_{2\downarrow}^\dagger(-\mathbf{k}_\parallel, z) + h.c. \\
& + A_1(z) [\psi_{1\uparrow}^\dagger(-i\partial_z) \psi_{2\uparrow} + \psi_{1\downarrow}^\dagger(i\partial_z) \psi_{2\downarrow} + h.c.] \\
& \left. + A_2(z) [\psi_{1\uparrow}^\dagger k_- \psi_{2\downarrow} + \psi_{1\downarrow}^\dagger k_+ \psi_{2\uparrow} + h.c.] \right\}. \tag{3.7}
\end{aligned}$$

Here $h_0(\mathbf{k}_\parallel, \partial_z) = M - B_1 \partial_z^2 - B_2 k_\parallel^2$, $\mu(z)$ and $A_i(z)$ are piece-wise constant,

$$\mu(z) = E_f \theta(d - z) + \mu \theta(z - d), \tag{3.8}$$

$$A_i(z) = A_i \theta(z - d), \quad i = 1, 2 \tag{3.9}$$

in terms of the step function θ . The order parameter obeys the gap equation

$$\Delta(z) = g(z) \int d\mathbf{k}_\parallel \langle \psi_{2\uparrow}(\mathbf{k}_\parallel, z) \psi_{2\downarrow}(-\mathbf{k}_\parallel, z) \rangle. \tag{3.10}$$

We assume $g(z) = g \theta(d - z)$, the coupling constant g determines the bulk gap.

To self-consistently solve Eq. (3.7) and (3.10), we introduce Bogoliubov transformation

$$\psi_{l\sigma}(\mathbf{k}_\parallel, z) = \sum_n u_{n,l\sigma}(\mathbf{k}_\parallel, z) \gamma_{n,\mathbf{k}_\parallel} + v_{n,l\sigma}^*(\mathbf{k}_\parallel, z) \gamma_{n,\mathbf{k}_\parallel}^\dagger \tag{3.11}$$

to diagonalize \mathcal{H} as

$$\mathcal{H} = E_g + \int d\mathbf{k}_\parallel \sum_n \epsilon_n(k_\parallel) \gamma_{n,\mathbf{k}_\parallel}^\dagger \gamma_{n,\mathbf{k}_\parallel}, \tag{3.12}$$

where E_g is the ground state energy, and $\gamma_{n,\mathbf{k}_\parallel}^\dagger$ is the creation operator of Bogoliubov quasi-particles with energy $\epsilon_n(k_\parallel)$. The wave function u and v satisfy the following Bogoliubov-de Gennes (BdG) equation,

$$\hat{H}_B(\mathbf{k}_\parallel, z)\hat{\phi}_n(\mathbf{k}_\parallel, z) = \epsilon_n(k_\parallel)\hat{\phi}_n(\mathbf{k}_\parallel, z). \quad (3.13)$$

Here, the BdG Hamiltonian

$$\hat{H}_B = \begin{pmatrix} h_0 - \mu & \mathbf{d} \cdot \boldsymbol{\sigma} & 0 & 0 \\ \mathbf{d} \cdot \boldsymbol{\sigma} & -h_0 - \mu & 0 & -\Delta i\sigma_y \\ 0 & 0 & \mu - h_0 & \mathbf{d} \cdot \boldsymbol{\sigma}^* \\ 0 & \Delta^* i\sigma_y & \mathbf{d} \cdot \boldsymbol{\sigma}^* & \mu + h_0 \end{pmatrix}, \quad (3.14)$$

and the wave function (dropping the arguments)

$$\hat{\phi}_n = (u_{n,1\uparrow}, u_{n,1\downarrow}, u_{n,2\uparrow}, u_{n,2\downarrow}, v_{n,1\uparrow}, v_{n,1\downarrow}, v_{n,2\uparrow}, v_{n,2\downarrow})^T. \quad (3.15)$$

The vector $\mathbf{d}(\mathbf{k}_\parallel, z)$ is defined as

$$d_x = A_1(z)k_x, \quad d_y = A_1(z)k_y, \quad d_z = A_2(z)(-i\partial_z). \quad (3.16)$$

Other quantities such as $h_0(\mathbf{k}_\parallel, z)$, $\mu(z)$, and $\Delta(z)$ are defined above. In terms of the wave functions, the zero temperature gap equation becomes

$$\Delta(z) = g(z) \int d\mathbf{k}_\parallel \sum'_n u_{n,2\uparrow}(\mathbf{k}_\parallel, z) v_{n,2\downarrow}^*(-\mathbf{k}_\parallel, z), \quad (3.17)$$

where the summation denoted by prime is restricted to $0 < \epsilon_n < \omega_D$ with ω_D being the Debye frequency.

We will exploit a particular symmetry of the BdG Hamiltonian to simplify calculations. Define the polar angle φ_k for the in-plane wave vector \mathbf{k}_{\parallel} ,

$$k_x + ik_y = k_{\parallel} e^{i\varphi_k}. \quad (3.18)$$

Then the BdG Hamiltonian for arbitrary (k_x, k_y) is related to that for $(k_x = k_{\parallel}, k_y = 0)$ by unitary transformation

$$\hat{U}^{\dagger}(\mathbf{k}_{\parallel}) \hat{H}_B(k_x, k_y) \hat{U}(\mathbf{k}_{\parallel}) = \hat{H}_B(k_{\parallel}, 0). \quad (3.19)$$

Here U is a block diagonal matrix,

$$U(\mathbf{k}_{\parallel}) = \text{diag}[e^{-i\sigma_z \frac{\varphi_k}{2}}, e^{-i\sigma_z \frac{\varphi_k}{2}}, e^{i\sigma_z \frac{\varphi_k}{2}}, e^{i\sigma_z \frac{\varphi_k}{2}}]. \quad (3.20)$$

Thus, the eigen energy ϵ_n only depends on the magnitude of \mathbf{k}_{\parallel} . Once the wave function for $\varphi_k = 0$ is known, the wave function for $\varphi_k \in (0, 2\pi)$ can be obtained by simple unitary transformation.

We solve the matrix differential equation (3.13) by conserving it into an algebraic equation, following the treatment of superconductor-ferromagnet structure by Halterman and Valls [79]. The whole S-TI proximity structure is assumed to have finite dimension L in the z direction. The superconductor occupies the region $0 < z < d$, while the topological insulator occupies $d < z < L$. Hard wall boundary conditions are enforced at the end points, $z = 0$ and $z = L$. The exact boundary conditions at the end points only affect the local physics there, provided that the boundaries are sufficiently far away from the S-TI

interface. We expand the wave function and order parameter in Fourier series [79],

$$u_{n,l\sigma}(z) = \sum_m u_{nm}^{l\sigma} \phi_m(z), \quad (3.21)$$

$$v_{n,l\sigma}(z) = \sum_m v_{nm}^{l\sigma} \phi_m(z), \quad (3.22)$$

$$\Delta(z) = \sum_m \Delta_m \phi_m(z), \quad (3.23)$$

$$\phi_m(z) = \sqrt{2/L} \sin(k_m z). \quad (3.24)$$

The integer $m = 1, 2, \dots, N$ labels the quantized longitudinal (along z) momentum $k_m = m\pi/L$. The cutoff N is chosen as [80]

$$B_1 k_N^2 = M + E_f + \omega_D. \quad (3.25)$$

By expansion Eq. (3.21)-(3.23), the BdG equation becomes an $8N \times 8N$ matrix equation. With a reasonable guess of the order parameter profile, the eigen energies and eigen wave functions are obtained by solving the matrix eigen value problem. Then a new order parameter profile is computed from the gap equation. The procedure is iterated until convergence is achieved. Relevant technical details can be found in the Fourier calculations section.

To analyze the spectrum of the system, it is convenient to define the retarded Green's function

$$G_{l\sigma}^R(\mathbf{k}_\parallel, z, t) = -i\theta(t) \langle \{\psi_{l\sigma}(\mathbf{k}_\parallel, z, t), \psi_{l\sigma}^\dagger(\mathbf{k}_\parallel, z, 0)\} \rangle \quad (3.26)$$

where the time-dependent field operators are in Heisenberg picture. For given \mathbf{k}_\parallel and z , the spectral functions are defined as

$$N_{l\sigma}(\mathbf{k}_\parallel, z, \omega) = -\text{Im}G_{l\sigma}^R(\mathbf{k}_\parallel, z, \omega), \quad (3.27)$$

$$N(\mathbf{k}_\parallel, z, \omega) = \sum_{l\sigma} N_{l\sigma}(\mathbf{k}_\parallel, z, \omega). \quad (3.28)$$

In terms of the wave functions and eigen energies,

$$N_{l\sigma}(\mathbf{k}_{\parallel}, z, \omega > 0) = \sum_n |u_{n,l\sigma}(\mathbf{k}_{\parallel}, z)|^2 \delta(\omega - \epsilon_n). \quad (3.29)$$

We also introduce the equal-time pair correlation functions for the conduction electrons

$$F_{\alpha\beta}(\mathbf{k}_{\parallel}, z) = \langle \psi_{2\alpha}(\mathbf{k}_{\parallel}, z) \psi_{2\beta}(-\mathbf{k}_{\parallel}, z) \rangle. \quad (3.30)$$

For example, at zero temperature we have

$$F_{\uparrow\uparrow}(\mathbf{k}_{\parallel}, z) = \sum_n' u_{n,2\uparrow}(\mathbf{k}_{\parallel}, z) v_{n,2\uparrow}^*(-\mathbf{k}_{\parallel}, z), \quad (3.31)$$

$$F_{\downarrow\downarrow}(\mathbf{k}_{\parallel}, z) = \sum_n' u_{n,2\downarrow}(\mathbf{k}_{\parallel}, z) v_{n,2\downarrow}^*(-\mathbf{k}_{\parallel}, z). \quad (3.32)$$

Triplet components of F will be induced near the S-TI interface by spin-active scattering [78].

3.3 Fourier Expansion

We follow the numerical scheme of Halterman and Valls to solve the matrix BdG equation [79]. The wave functions and the order parameter are expanded in the orthonormal basis $\{\phi_m(z)\}$, with $m = 1, \dots, N$. For example, function $u_{n,1\uparrow}(z)$ is represented by N numbers,

$$(u_{n,1}^{1\uparrow}, u_{n,2}^{1\uparrow}, \dots, u_{n,m}^{1\uparrow}, \dots, u_{n,N}^{1\uparrow}).$$

Accordingly, each term in \hat{H}_B is represented by a $N \times N$ matrix with the matrix elements given by

$$h_0(\mathbf{k}_{\parallel}, \partial_z) \rightarrow \delta_{mm'}(M - B_1 k_m^2 - B_2 k_{\parallel}^2)$$

$$U(z) \rightarrow E_f E_{mm'} + \mu F_{mm'}$$

$$A_2(z) \partial_z \rightarrow A_2 G_{mm'}$$

$$A_1(z) k_{\pm} \rightarrow A_z k_{\pm} F_{mm'}$$

$$\Delta \rightarrow D_{mm'} \equiv \sum_{m''} J_{m,m',m''} \Delta_{m''}$$

where

$$\begin{aligned} E_{mm'} &= \int_0^d \phi_m(z) \phi_{m'}(z) dz \\ F_{mm'} &= \int_d^L \phi_m(z) \phi_{m'}(z) dz \\ G_{mm'} &= \int_d^L \phi_m(z) \partial_z \phi_{m'}(z) dz \\ J_{m,m',m''} &= \int_0^d \phi_m(z) \phi_{m'}(z) \phi_{m''}(z) dz \end{aligned}$$

These integrals can be evaluated analytically. Then the BdG equation becomes an $8N \times 8N$ matrix equation. The gap equation can be rewritten as

$$\Delta_m = g \int d\mathbf{k}_{\parallel} \sum_n' \sum_{m',m''} J_{m,m',m''} u_{nm'}^{2\uparrow}(\mathbf{k}_{\parallel}) v_{nm''}^{2\downarrow}(-\mathbf{k}_{\parallel})^*$$

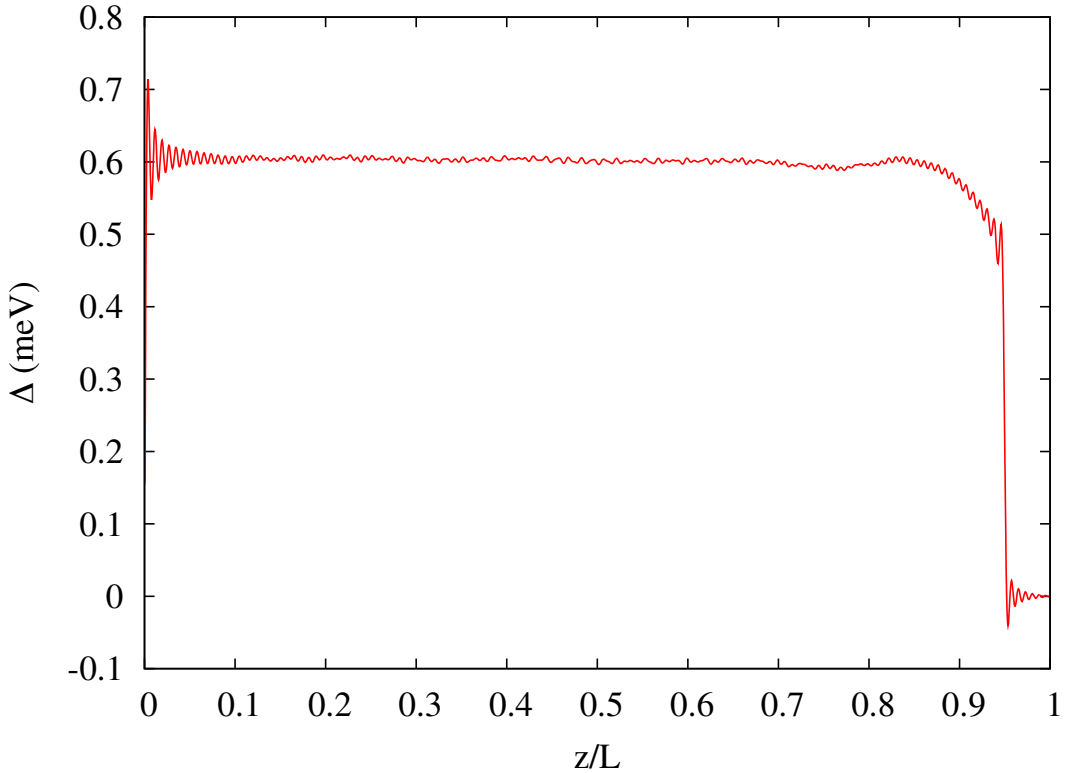


Figure 3.2: The superconducting order parameter $\Delta(z)$ near an S-TI interface at $z = d = 0.95L$. The superconductor occupies $0 < z < d$, and topological insulator occupies $d < z < L$. $L = 300$ nm, $\mu=0$, the bulk gap $\Delta_0 = 0.6$ meV.

The integral over \mathbf{k}_{\parallel} is first simplified to an integral over k_{\parallel} by the symmetry Eq. (3.19) and then evaluated numerically with high momentum cutoff $\sqrt{(E_F + \omega_D + M)/B_2}$.

3.4 The Order Parameter

First we present the spatial profile of the superconducting order parameter $\Delta(z)$ after the convergence is achieved. In all following calculations, E_f is fixed at 0.4 eV, which is modeled after optimally doped $\text{Cu}_x\text{Bi}_2\text{Se}_3$ [74]. And the Debye frequency is set as $\omega_D = 0.1E_f$ [79].

Fig. 3.2 shows an example with $\mu = 0$, $L = 300\text{nm}$, $d = 0.95L$, and a bulk gap of 0.6meV as found in $\text{Cu}_x\text{Bi}_2\text{Se}_3$. Going from the superconductor into the topological insulator, Δ first gets suppressed as the interface is approached before it drops to zero inside TI. The suppression is roughly 20% at the interface. Note that the fine wiggles of Δ in the simulation results are due to the finite momentum cutoff of the longitudinal momentum k_m . As previously discussed by Stojkovic and Valls [80], the number of oscillations is $\sim N/2$, and the oscillation amplitude vanishes in the bulk as N is increased. In this case, N is chosen to be 258 according to Eq. (3.25). So the matrix to be diagonalized is 2064 by 2064.

Fig. 3.3 show the result for $\mu = 0$, $d = 0.9L$, and a superconductor with bulk gap $\Delta_0 \sim 2.4\text{meV}$. Since the coherence length is much smaller than the previous example, it is sufficient to consider $L = 160\text{nm}$, and correspondingly $N = 138$. The order parameter profile depends weakly on μ , as shown in Fig. 3.4 for a superconductor with bulk gap $\sim 5.2\text{meV}$. From these examples, one observes that the length scale over which Δ is significantly suppressed does *not* scale with ξ_0 , the zero temperature coherence length of the superconductor. Rather it stays roughly the same, on the order of 30nm, as ξ_0 is varied over one decade from Fig. 3.2 to Fig. 3.4 (note the horizontal axis is z/L). This is not very surprising since ξ_0 is not the only length scale at play here. The interface represents a strong (as compared to Δ_0) perturbation that significantly distorts the bulk wave functions. The self-consistent microscopic BdG approach provides a reliable way to capture the details of $\Delta(z)$ near the interface.

It is illuminating to compare the proximity effect in S-TI structure with that in S-F structure [30], where F stands for a ferromagnetic insulator. The presence of F breaks time-reversal and spin rotation symmetry and significantly suppresses the order parameter. The suppression is sensitive to the spin mixing angle which is related to the band gap and exchange field of F [30]. In contrast, despite the spin-active scattering of electrons by TI which introduces spin-flips and spin-dependent phase shifts [78], spin-orbit coupling is not pair breaking. The suppression of Δ near the interface is to a large extent due to the reorganization of local wave functions enforced by the boundary conditions at $z = d$ for

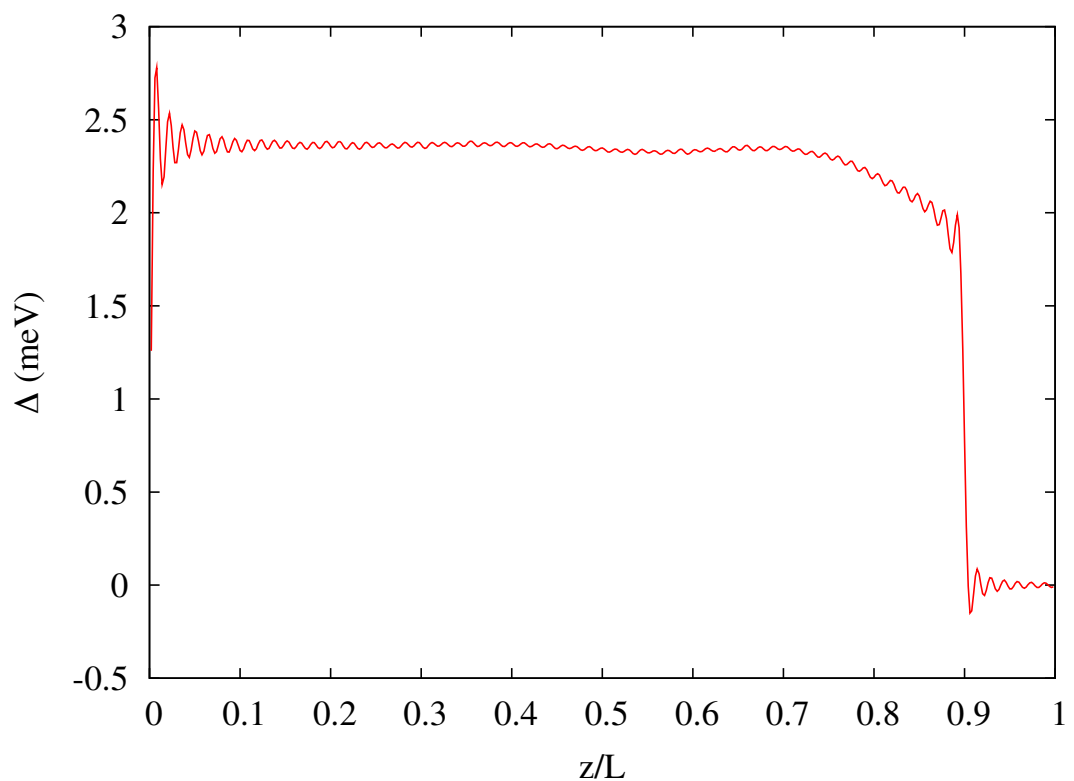


Figure 3.3: The order parameter $\Delta(z)$ near an S-TI interface at $z = d = 0.9L$. $L = 160$ nm, $\mu=0$, $\Delta_0 \sim 2.4$ meV.

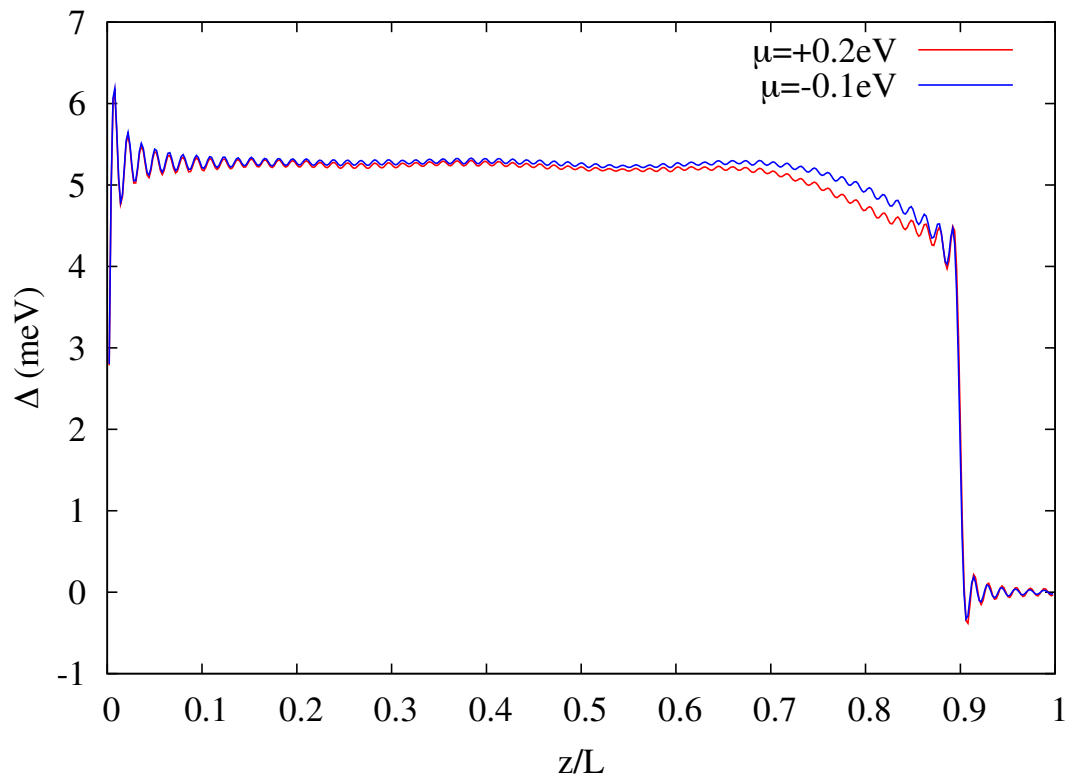


Figure 3.4: The order parameter profile for two different chemical potentials of the topological insulator, $\mu = -0.1\text{eV}$ and $\mu = 0.2\text{eV}$. $L = 160\text{nm}$, $\Delta_0 \sim 5.2\text{meV}$.

piece-wise potentials $\mu(z)$, $A_i(z)$, $g(z)$. It depends on for example how the wave functions decay inside the TI for given E_f and μ , and involves “high-energy” physics beyond the scale of Δ but below the scale of the band gap. To test this, we have investigated the proximity effect between the same superconductor and a hypothetical ordinary insulator modeled by H_{TI} with $A_1 = A_2 = 0$ and the same band gap. The suppression of Δ by such an ordinary insulator turns out to be very similar.

3.5 The Interface Mode and the Fu-Kane Model

Next we analyze the energy spectrum of the system, $\epsilon_n(k_\parallel)$, obtained from the BdG calculation. Take the case of $\mu = 0$, $L = 160\text{nm}$, $d = 0.9L$, $\Delta_0 \sim 5.2\text{meV}$ as an example. Fig. 3.5 shows the first several energy levels of the composite system versus the transverse momentum k_\parallel . There are many continuously dispersing modes at energies above the bulk gap. They are the usual Bogoliubov quasiparticles for different quantized longitudinal momenta. One also sees a series of avoided level crossings. At small k_\parallel emerges a well-defined mode below Δ_0 . We will identify it as the interface mode first discussed by Fu and Kane [58].

The Fu-Kane model Eq. (3.1) predicts the dispersion

$$E(k) = \sqrt{|\Delta_s|^2 + (v_s k \pm \mu_s)^2}. \quad (3.33)$$

We fit the very low energy portion of the spectrum to this prediction to extract the phenomenological parameters in the Fu-Kane model. The result is shown in Fig. 3.5. We find that, not surprisingly, $\Delta_s = 1.8\text{meV}$ which is much smaller than $\Delta_0 = 5.2\text{meV}$, and $v_s = 2.7\text{eV}\text{\AA}$ which deviates significantly from $A_2 = 4.2\text{eV}\text{\AA}$ predicted for the surface dispersion of TI. Moreover, $\mu_s = 7.5\text{meV}$ despite that the chemical potential of TI is $\mu = 0$. Therefore, our results show that the values of (Δ_s, v_s, μ_s) are strongly renormalized by the presence of the superconductor. This is consistent with the findings of Stanescu et al for weakly coupled S-TI structures [48].

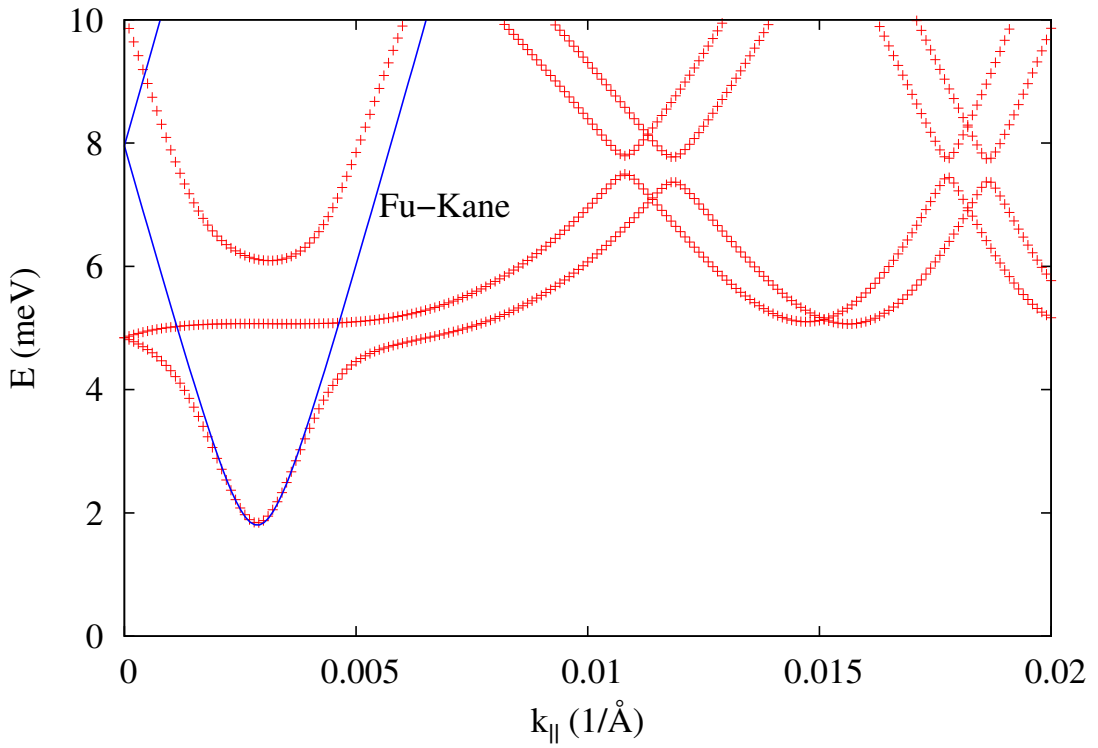


Figure 3.5: The lowest few energy levels $\epsilon_n(k_{\parallel})$. $\mu = 0$, $L = 160\text{nm}$, and the bulk superconducting gap $\Delta_0 \sim 5.2\text{meV}$. A well-defined interface mode is clearly visible at sub-gap energies. Solid lines show a fit to the Fu-Kane model, with $\Delta_s = 1.8\text{meV}$, $v_s = 2.7\text{eV}\text{\AA}$, and $\mu_s = 7.5\text{meV}$.

We have checked the validity of the Fu-Kane model for a variety of chemical potentials. Representative examples are plotted in Fig. 3.6. In each case, the sub-gap mode can be well accounted by the Fu-Kane model with suitable choice of parameters. While μ_s is always different from μ , numerically we find it scales linearly with μ . At the same time, Δ_s and v_s show no strong dependence on μ for this set of parameters. To make sure that the sub-gap mode is indeed localized near the interface, we plot in Fig. 3.7 the z dependence of the spectral function $N(k_{\parallel}, z, \omega)$. The spectral weight of the sub-gap mode is peaked near the interface and decays over a length scale $\sim \xi_0$ into the superconductor. This result clearly shows that for strongly coupled S-TI interfaces, the Fu-Kane model actually describe a rather “fat” interface mode. Note that the spectral weight on the TI side (not shown in the figure) is finite, but it is much smaller in magnitude and decays very fast inside TI. Finally, Fig. 3.8 shows the local density of states near the interface. The interface mode leads to finite density of states below the bulk gap, but the spectral weight is very small.

We have carried out similar analysis for superconductors with larger coherence length. Fig. 3.9 shows the evolution of the sub-gap mode with μ for $\Delta_0 = 2.4\text{meV}$. In this case, the values of (Δ_s, v_s, μ_s) all varies with μ . Superconductors with larger ξ_0 and smaller Δ_0 are thus more sensitive to changes in μ and other microscopic details near the interface. The exact values of the effective parameters in the Fu-Kane model in general depend on such microscopic details.

3.6 Triplet Pair Correlations

It is well known that in heterostructures of s -wave superconductors, pairing correlations in other orbital channels, e.g. p -wave correlations, will be induced by scattering at the interfaces [81, 82]. For example, inversion/reflection symmetry ($z \leftrightarrow -z$) is lost in an S-TI proximity structure, and the appearance of p -wave correlations seems natural from partial wave analysis. Moreover, scattering by a topological insulator is spin-active. The spin-orbit coupling inside a TI acts like a momentum-dependent magnetic field to flip the

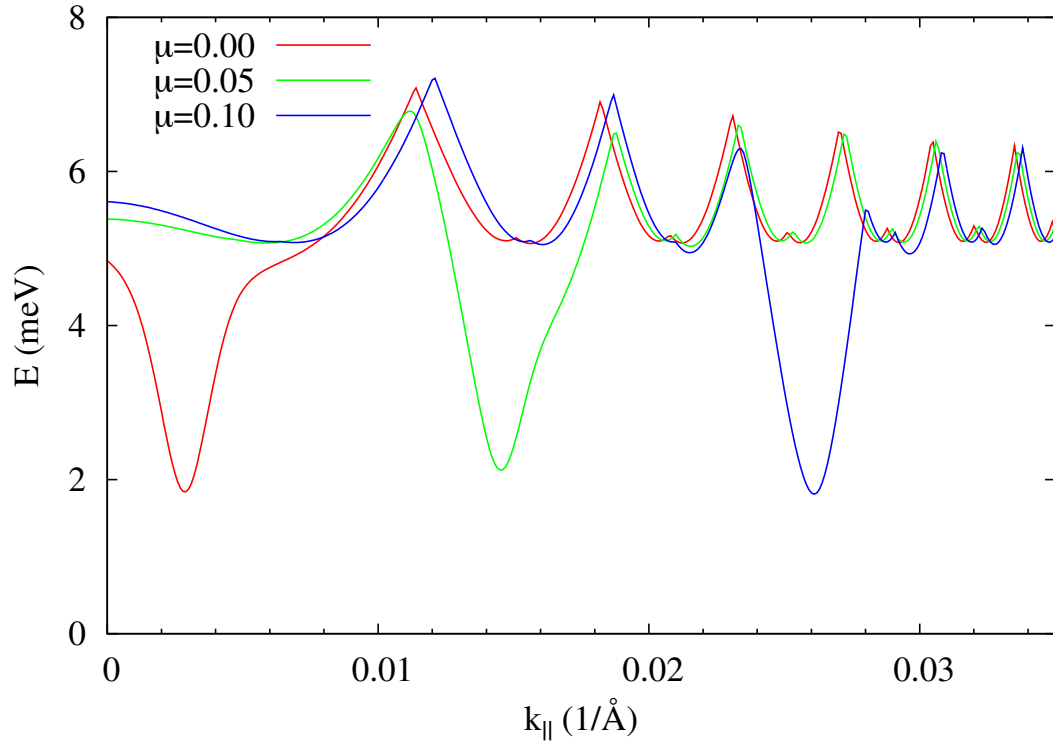


Figure 3.6: The dispersion of the lowest energy level for different μ (in eV). Other parameters are the same as in Fig. 3.5, $L = 160\text{nm}$ and $\Delta_0 \sim 5.2\text{meV}$. Fu-Kane model well describes the lowest energy mode. As μ is increased, Δ_s and v_s stay roughly the same, while μ_s scales linearly with μ .

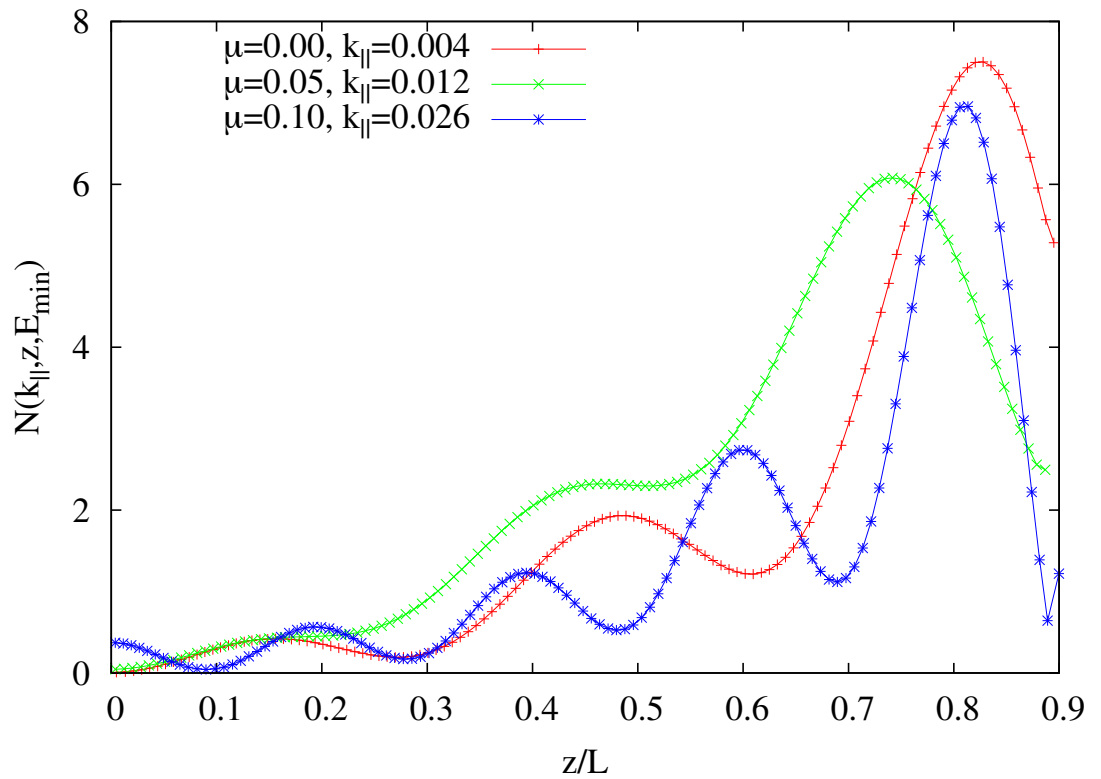


Figure 3.7: The spectral function $N(k_{\parallel}, z, \omega)$ of the lowest energy level, $\omega = E_{\min}$, shown in Fig. 3.6. The interface is at $z = 0.9L$, $L=160\text{nm}$. The spectral function oscillates rapidly with z , so only its envelope is plotted.

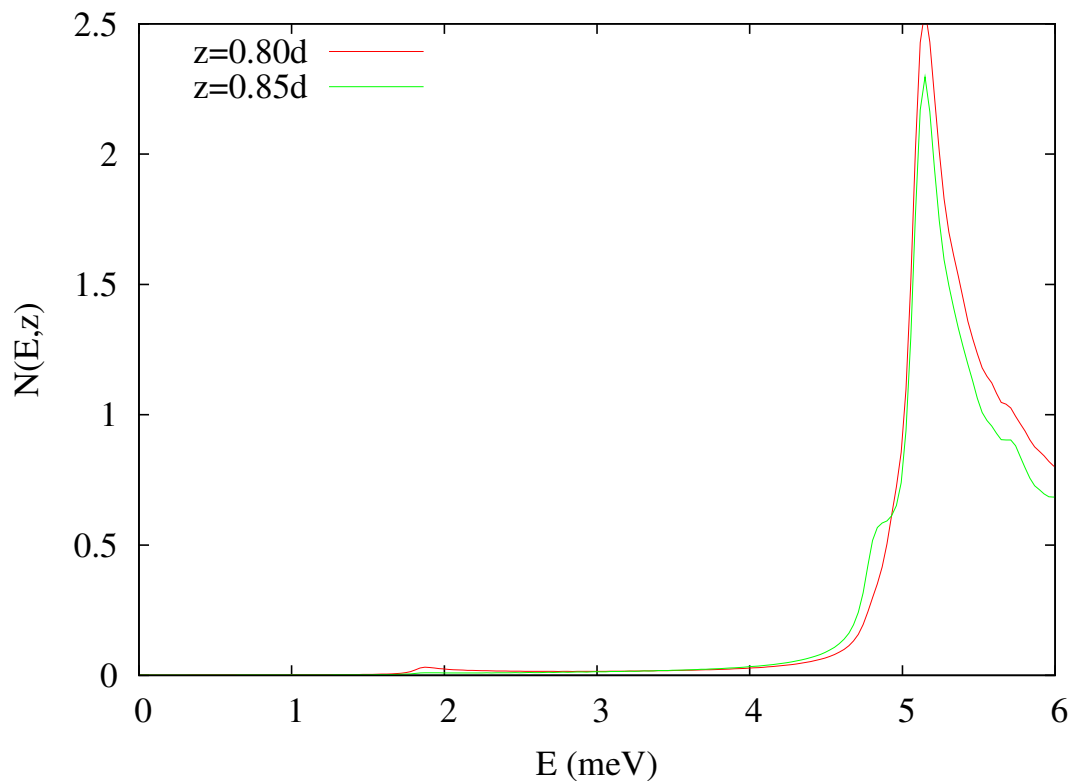


Figure 3.8: The local density of states $N(E, z)$ at $z = 0.8d$ and $z = 0.85d$ (the interface is at $z = 0.9d$). $\mu = 0$, $L = 160\text{nm}$, and $\Delta_0 \sim 5.2\text{meV}$. The subgap states are due to the interface mode. A level broadening $\sim 0.01\Delta_0$ is used.

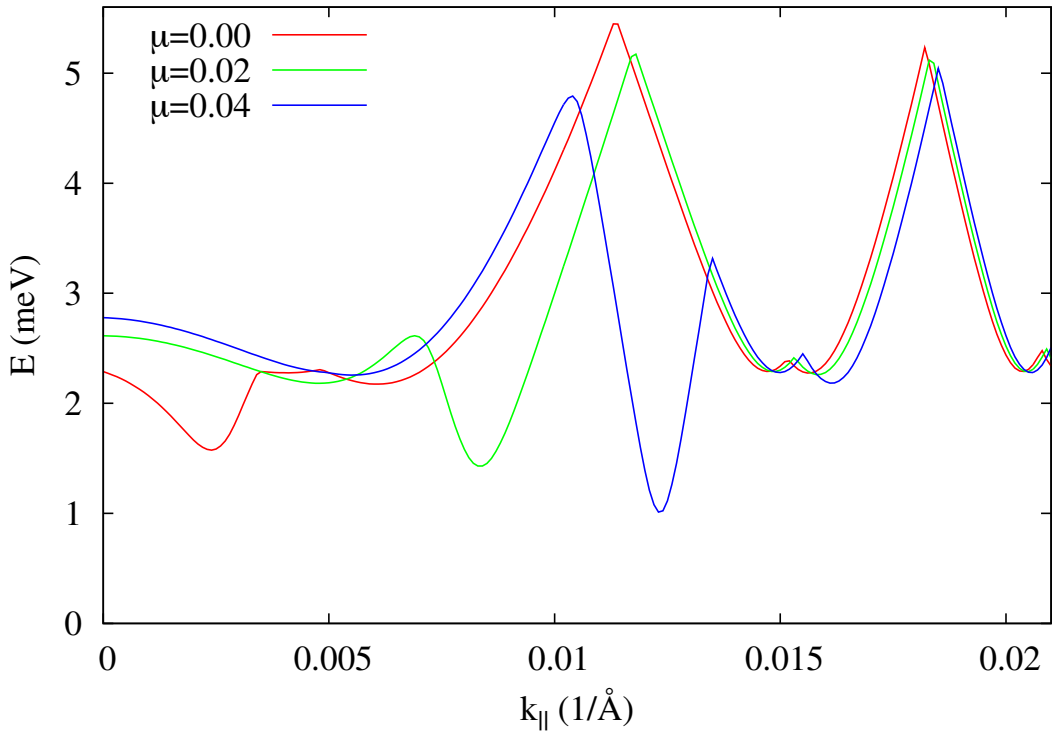


Figure 3.9: The lowest energy level of an S-TI structure with $L = 160\text{nm}$, $d = 0.9L$, $\Delta_0 = 2.4\text{meV}$. μ is the chemical potential of the TI and measured in eV.

electron spin and introduce different phase shifts for spin up and down electrons. The scattering matrix has been worked out by us previously [78]. Thus, a singlet *s*-wave Cooper pair can be converted into a pair of electrons in spin-triplet state at the S-TI interface. However, it is important to recall that by assumption attractive interaction only exists (or is appreciable) in the *s*-wave channel. There is no binding force to sustain a triplet Cooper pair or a triplet superconducting order parameter. Similar (but different) pairing correlations in superconductor-ferromagnet hybrid structures have been extensively studied [81]. The appearance of *p*-wave correlations in S-TI systems has been pointed out previously by Stanescu et al using a perturbative analysis [48].

We focus on the equal-time pair correlation functions defined in Eq. (3.30). By exploiting the symmetry of the BdG Hamiltonian, Eq. (3.19), we are able to find analytically the orbital structure of the triplet correlation functions. The unitary transformation Eq. (3.20) yields

$$\begin{aligned} u_{2\uparrow}(k_x, k_y) &= u_{2\uparrow}(k_{\parallel}, 0)e^{-i\varphi_k/2}, \\ u_{2\downarrow}(k_x, k_y) &= u_{2\downarrow}(k_{\parallel}, 0)e^{+i\varphi_k/2}, \\ v_{2\uparrow}(k_x, k_y) &= v_{2\uparrow}(k_{\parallel}, 0)e^{+i\varphi_k/2}, \\ v_{2\downarrow}(k_x, k_y) &= v_{2\downarrow}(k_{\parallel}, 0)e^{-i\varphi_k/2}. \end{aligned} \tag{3.34}$$

Using these relations, we find

$$F_{\uparrow\uparrow}(\mathbf{k}_{\parallel}, z) = F_{\uparrow\uparrow}(k_{\parallel}, z)e^{-i\varphi_k}, \tag{3.35}$$

$$F_{\downarrow\downarrow}(\mathbf{k}_{\parallel}, z) = F_{\downarrow\downarrow}(k_{\parallel}, z)e^{+i\varphi_k}. \tag{3.36}$$

Namely $F_{\uparrow\uparrow}$ ($F_{\downarrow\downarrow}$) has $p_x - ip_y$ ($p_x + ip_y$) orbital symmetry. Finally, the remaining triplet

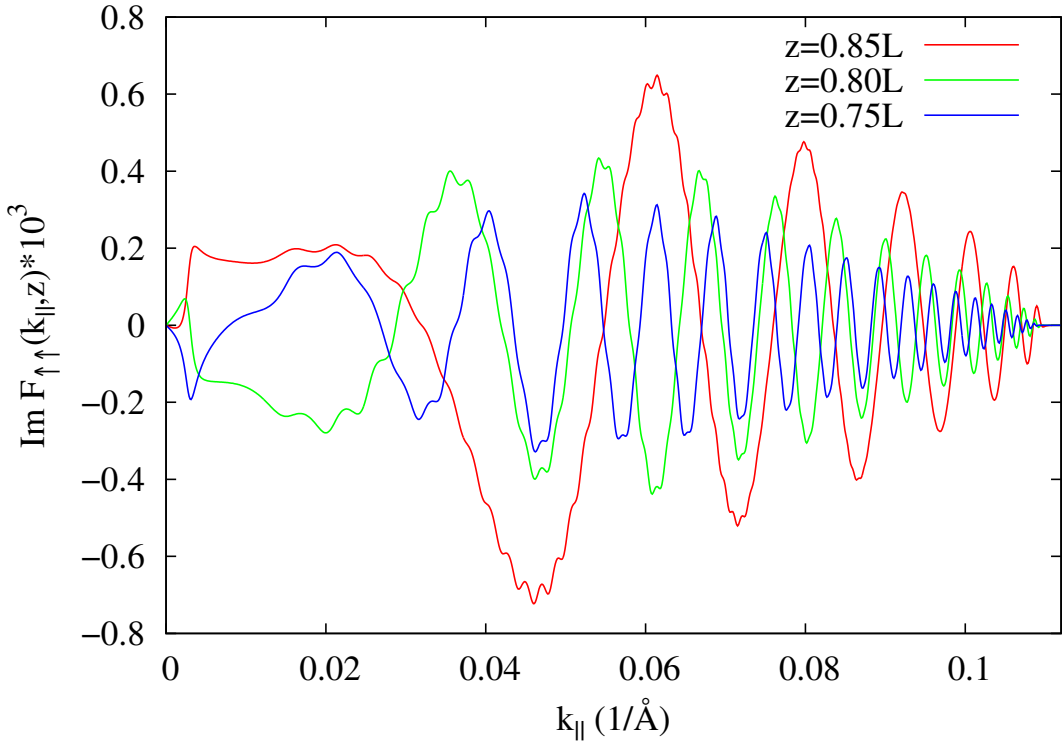


Figure 3.10: The imaginary part of triplet pair correlation function $F_{\uparrow\uparrow}(k_{\parallel}, z)$. The S-TI interface is at $d = 0.9L$. $\mu = 0$, $L = 160\text{nm}$, $\Delta_0 = 5.2\text{meV}$.

correlation function

$$\langle \psi_{2\uparrow}(\mathbf{k}_{\parallel}, z) \psi_{2\downarrow}(-\mathbf{k}_{\parallel}, z) + \psi_{2\downarrow}(\mathbf{k}_{\parallel}, z) \psi_{2\uparrow}(-\mathbf{k}_{\parallel}, z) \rangle \quad (3.37)$$

turns out to be zero. Note that the so-called odd-frequency paring correlations [81, 82, 83], which vanishes in the equal-time limit, are also interesting in S-TI structures, but we will not discuss their behaviors here.

We find that $F_{\uparrow\uparrow}(k_{\parallel}, z)$ is purely imaginary and identical to $F_{\downarrow\downarrow}(k_{\parallel}, z)$. The results for

$\mu = 0$, $L = 160\text{nm}$, $d = 0.9L$, $\Delta_0 = 5.2\text{meV}$ are plotted in Fig. 3.10. $F_{\uparrow\uparrow}$ vanishes at $k_{\parallel} = 0$ as well as for large k_{\parallel} , namely when $k_{\parallel} > \sqrt{(E_F + \omega_D + M)/B_2}$. This is consistent with lack of pairing in both limits. The behavior of $F_{\uparrow\uparrow}$ for small k_{\parallel} is illustrated in Fig. 3.11 for $\mu = 0$, $L = 300\text{nm}$, $d = 0.95L$, $\Delta_0 = 0.6\text{meV}$. As comparison, we also plotted the singlet pair correlation function

$$F_{\uparrow\downarrow}(\mathbf{k}_{\parallel}, z) = \sum_n' u_{n,2\uparrow}(\mathbf{k}_{\parallel}, z) v_{n,2\downarrow}^*(-\mathbf{k}_{\parallel}, z) \quad (3.38)$$

which is *s*-wave and purely real.

3.7 Summary

In summary, we have investigated the proximity effect between an *s*-wave superconductor and a topological insulator using a microscopic continuum model. Strong coupling between the two materials renders the surface state of TI a less useful concept for this problem. Our focus has been on the various modifications to superconductivity by the presence of TI. These include the suppression of the order parameter, the formation of interface modes below the bulk superconducting gap, and the induction of triplet pairing correlations. It is gratifying to see the Fu-Kane effective model emerges in the low energy sector albeit with a set of renormalized parameters. Our results are complementary to previous theoretical work on the proximity effect [58, 48] and confirm the validity of the Fu-Kane model.

We made a few simplifying assumptions in our calculation. The superconductor is described by a two-band model with the valence band well below the Fermi level. Since only electrons near the Fermi surface are relevant for weak coupling superconductivity, we believe our main results are general. As idealizations, the chemical potential, the spin-orbit coupling, and the attractive interaction are assumed to be step functions with a sudden jump at the interface. More elaborate and realistic models can be considered within the framework of BdG equations. For example, one can add a tunneling barrier between S and TI, or

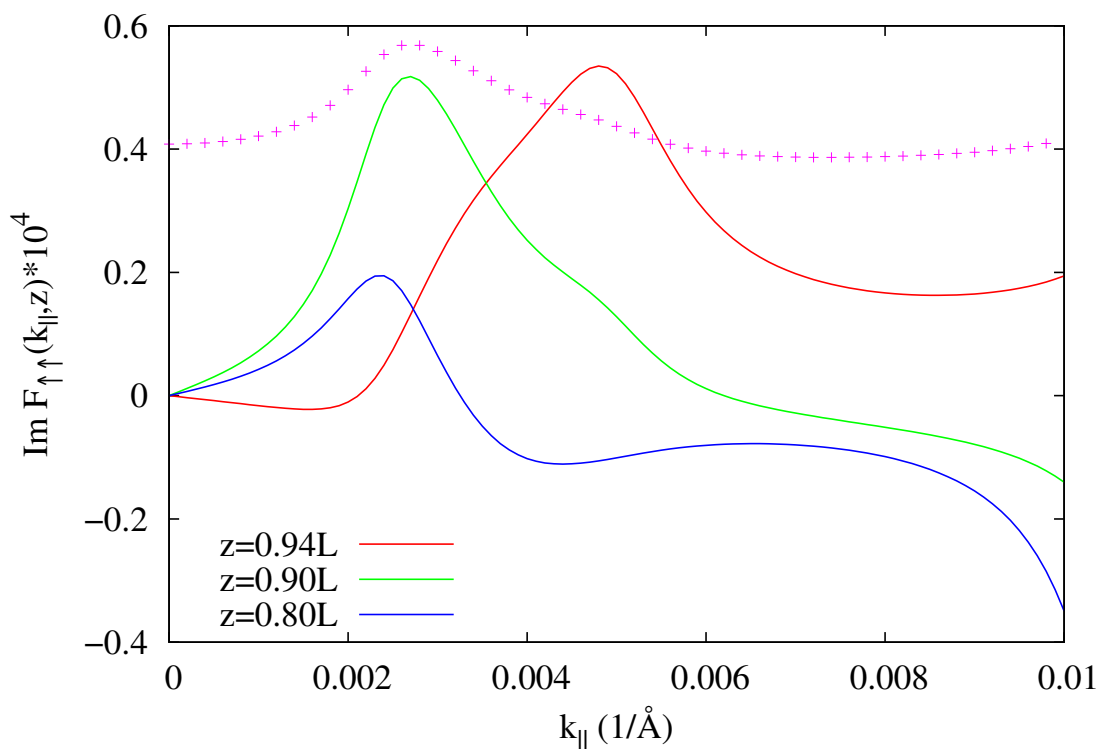


Figure 3.11: The imaginary part of $F_{\uparrow\uparrow}(k_{\parallel}, z)$. $\mu = 0$, $L = 300\text{nm}$, $d = 0.95L$, $\Delta_0 = 0.6\text{meV}$. As comparison, the data points show the singlet pair correlation function $F_{\uparrow\downarrow}(k_{\parallel}, z = 0.9L)/3$.

include a Rashba-type spin-orbit coupling term (due to the gradient of chemical potential) at the interface. We will not pursuit these generalizations here. Finally, the approach outlined here can be straightforwardly applied to study non-Abelian superconductivity in other superconductor-semiconductor heterostructures where spin-orbit coupling also plays a significant role [61, 62, 63, 64, 65].

Chapter 4: Josephson Junction on TI Surface

So far, we have found that the regions near the interface, between the topological insulator and a superconductor, is an exotic playground to interesting phenomena, namely a subgap energy state localized near the interface. This two dimensional interface considered to be the Fu-Kane superconductor and modeled by a Dirac-like relativistic equation

$$\mathcal{H} = -i\hbar v_F(\sigma_x \partial_y - \tau_z \sigma_y \partial_x) + \tau_z \mu + \tau_y \sigma_y \Delta \quad (4.1)$$

is good up to some renormalization of the constants, v_F , μ , Δ as found in the previous chapter. This model was used in the first chapter to illustrate the existence of Majorana bound states localized where the effective mass term, Δ , changes sign ($\Delta \rightarrow -\Delta$) as in a Josephson π junction. This Majorana mode has a linear dispersion, $E \propto \pm k$. In this chapter we explore this π junction further, in particular for $\mu \neq 0$, where we find an energy dispersion that is flat and follows as $E \propto k^N$, where N scales with μ . An extension of the the π junction is a periodic π junction where alternating $(\dots -\Delta, \Delta, -\Delta, \Delta \dots)$ stripes of superconductors are placed in one direction. We find that this system also hosts the flat dispersion. We also find that the dispersion has “wiggles” when the spectrum is really closely analyzed.

4.1 Introduction

Moving at “the speed of light”, v_F , massless Dirac electrons on the surface of a three-dimensional Z_2 topological insulator (TI) can not be localized by scattering from nonmagnetic impurities [8, 10], nor can they be easily confined by electrostatic potentials due to Klein tunneling [84]. Proximity coupling to ferromagnetic or superconducting order can

however open up a gap in the spectrum, thus rendering excitations massive [8, 10]. An intriguing possibility is to engineer new *massless* excitations by confining and coherently mixing Dirac electrons and holes using two or more superconductors with definite phase difference [7]. For example, Fu and Kane showed that a Josephson junction on the surface of a TI with a phase bias of π is a one-dimensional quantum wire for Majorana fermions, which can be further manipulated by using tri-junctions [7]. Signatures of Majorana fermions in such structures have been reported in recent experiments [85, 86].

In this Letter, we demonstrate a drastically different regime for the same, albeit slightly more general, Josephson structures considered by Fu and Kane. This regime features massless zero energy excitations that are almost dispersion-less, i.e. with vanishing group velocity ($\partial E/\partial k \simeq 0$). We elucidate the scattering kinematics behind the nearly flat dispersion at zero energy using simple models, and verify the results with self-consistent calculations. We find it striking that in such simple structures, which are now available in experiments, the low energy excitation can be easily tuned all the way from $E \sim k$ to $E \sim k^N$, where N is large, by increasing the chemical potential. By extending such junctions into a class of *periodic* superconductor-TI proximity structures, we further show that these states become a flat band near zero energy.

4.2 Model

The Josephson junction is schematically shown in Fig. 4.1a). Two *s*-wave superconductors are patterned on the TI surface. Due to the proximity effect, the S-TI interface becomes a 2D superconductor (S). The S-TI-S junction can be well described by the following Bogoliubov-Dirac Hamiltonian introduced in Ref. [7],

$$\mathcal{H} = \hbar v_F (\sigma_x k_y + i\tau_z \sigma_y \partial_x) + \tau_z \mu(x) + \tau_y \sigma_y \Delta(x). \quad (4.2)$$

Here τ_i (σ_i) are the Pauli matrices in the particle-hole (spin) space. The system is translationally invariant in the y direction, and k_y is the momentum along y . In the TI region of

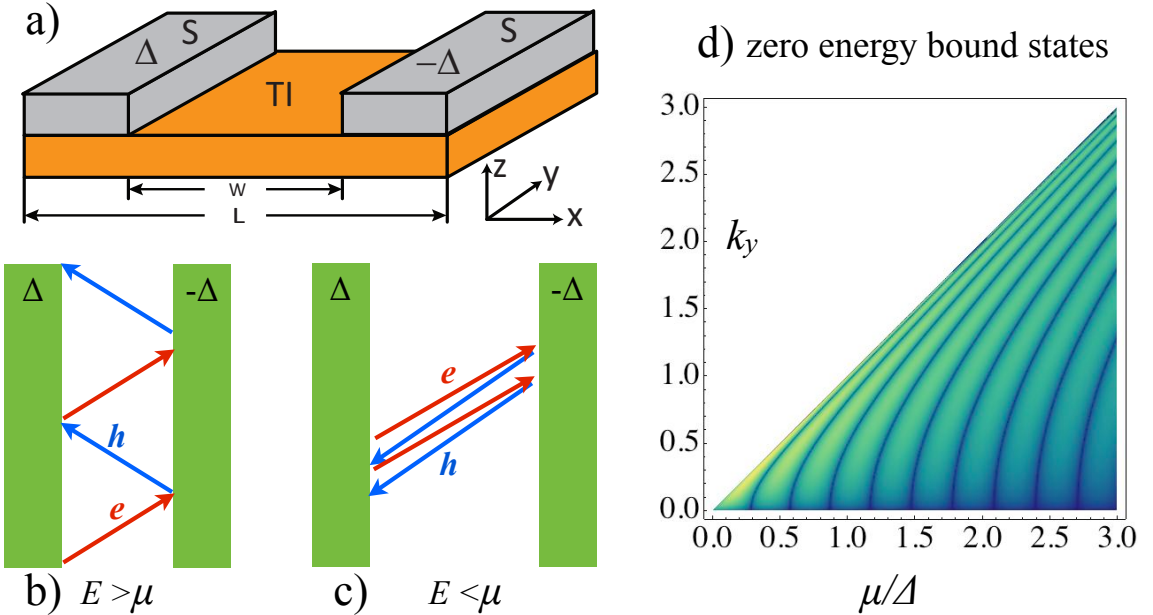


Figure 4.1: (color online) a) Schematic of a Josephson junction on the surface of a topological insulator (TI). The two superconducting leads (S) have a phase difference π . Δ is the superconducting gap, and w is the junction width (not to scale). b) Specular Andreev reflection in the regime $E > \mu$. c) Retro-reflection for $E < \mu$. d) Dark lines show the (k_y, μ) values for the zero energy Andreev bound states for $w = 10\hbar v_F/\Delta$ and $L \rightarrow \infty$. k_y is in unit of $\Delta/\hbar v_F$.

length w , the superconducting order parameter $\Delta(x)=0$, while it is constant Δ deep into the superconductor. The chemical potential μ can be tuned by applying a gate voltage. In general, its value can differ in the TI and S region, but for simplicity, we assume it is uniform in all regions. Also, we will focus on the case of phase difference of π across the junction.

We first give a heuristic argument for the existence of two regimes. A Dirac electron in the TI region incident on S will be Andreev reflected into a hole if its energy is below the superconducting gap ($E < \Delta$). In the context of graphene [87, 88], Beenakker pointed out

that in addition to the familiar Andreev retro-reflection where the reflected hole has a group velocity opposite to the incident electron when $E < \mu$, there is also the case of specular Andreev reflection where the reflected hole's group velocity is in the specular direction for $E > \mu$. Typical scattering trajectories in these two regimes are contrasted in Fig. 4.1b) and 4.1c). For $\mu = 0$ as considered in Ref. [7], the Majorana fermion excitation with linear dispersion is associated with the specular Andreev reflections in Fig. 4.1b). For large μ , as in the case of as grown Bi_2Se_3 crystals, one expects very different behaviors at low energies. For the $E < \mu$ case, it can be shown analytically that the phase of the retro-reflected hole is equal to the incident angle of an incoming electron at zero energy, $\theta = \arcsin(\hbar v_F k_y / \mu)$. This is unique to TIs because the wavefunction of a Dirac electron [or hole], $(1, \pm e^{i\theta}, 0, 0)$ $[(0, 0, 1, \pm e^{i\theta})]$, is determined by the angle θ , or k_y . The resultant hole incident on the opposite S with phase of π retro-reflects into an electron. This electron has exactly the same phase as it started with, thus forming an Andreev bound state.

The remaining key question is whether there will be any states at or near zero energy when μ is finite. We can answer the question by solving Eq. (4.2) for an idealized, step function profile of $\Delta(x)$,

$$\Delta(x) = \Delta[\theta(-x) - \theta(x - w)]. \quad (4.3)$$

The dark lines in Fig. 4.1d) shows the zero energy solution in the (μ, k_y) plane, with fixed Δ and the junction length $w = 10\hbar v_F / \Delta$. In general, there exist multiple zero energy bound states at discrete k_y values $\{k_y^i\}$ for finite μ . For increasing μ and w , these solutions become increasingly close-packed. This nontrivial result has important implications for experiments. The Majorana quantum wire is only ideal in the limit of $\mu, w \rightarrow 0$. As μ is tuned away from the Dirac point, the single zero energy state at $k = 0$ will be replaced by multiple zero energy solutions along the k_y axis, and eventually a nearly flat dispersion at zero energy.

To unambiguously establish this claim, we solve the differential equation $\mathcal{H}(x, k_y)\psi(x, k_y) = E\psi(x, k_y)$ numerically for a finite size system, $x \in [0, L]$ as shown in Fig. 4.1a), with open boundary conditions at $x = 0, L$ [89]. Here the quasiparticle wave function $\psi =$

$(u_\uparrow, u_\downarrow, v_\uparrow, v_\downarrow)^T$, with the label (x, k_y) omitted. To fully describe the proximity effect including the induced superconducting correlations in the TI region and the suppression of superconductivity near the TI-S boundary, we determine the order parameter profile $\Delta(x)$ self-consistently through the gap equation

$$\Delta(x) = g(x) \sum_{\epsilon_n < \omega_D} \int dk_y u_{n,\uparrow}(x, k_y) v_{n,\downarrow}^*(x, k_y). \quad (4.4)$$

Here n labels the eigenstates with energy ϵ_n , g is the effective attractive interaction, and ω_D is the Debye frequency. We assume g is zero in the TI region and constant inside S. We expand $\psi(x, k_y)$ and $\Delta(x)$ in Fourier series and convert the differential equation into an algebraic equation [90, 91]. Starting with an initial guess of $\Delta(x)$ which features phase difference π , the iterative procedure is repeated until desired convergence is achieved. Note that the phase difference π is self-maintained throughout and not fixed by hand after every iteration. Then, the local spectral function,

$$A_\sigma(E, k_y, x) = \sum_n \delta(E - \epsilon_n) |u_{n\sigma}(x, k_y)|^2, \quad (4.5)$$

and the local density of states (LDOS),

$$N(E, x) = \int dk_y \sum_{n,\sigma} \delta(E - \epsilon_n) |u_{n\sigma}(x, k_y)|^2, \quad (4.6)$$

can be computed for $\sigma = \uparrow, \downarrow$. The calculation is checked to reproduce known results, e.g., the linearly dispersing Majorana spectrum at $\mu = 0$ predicted in Ref. [7].

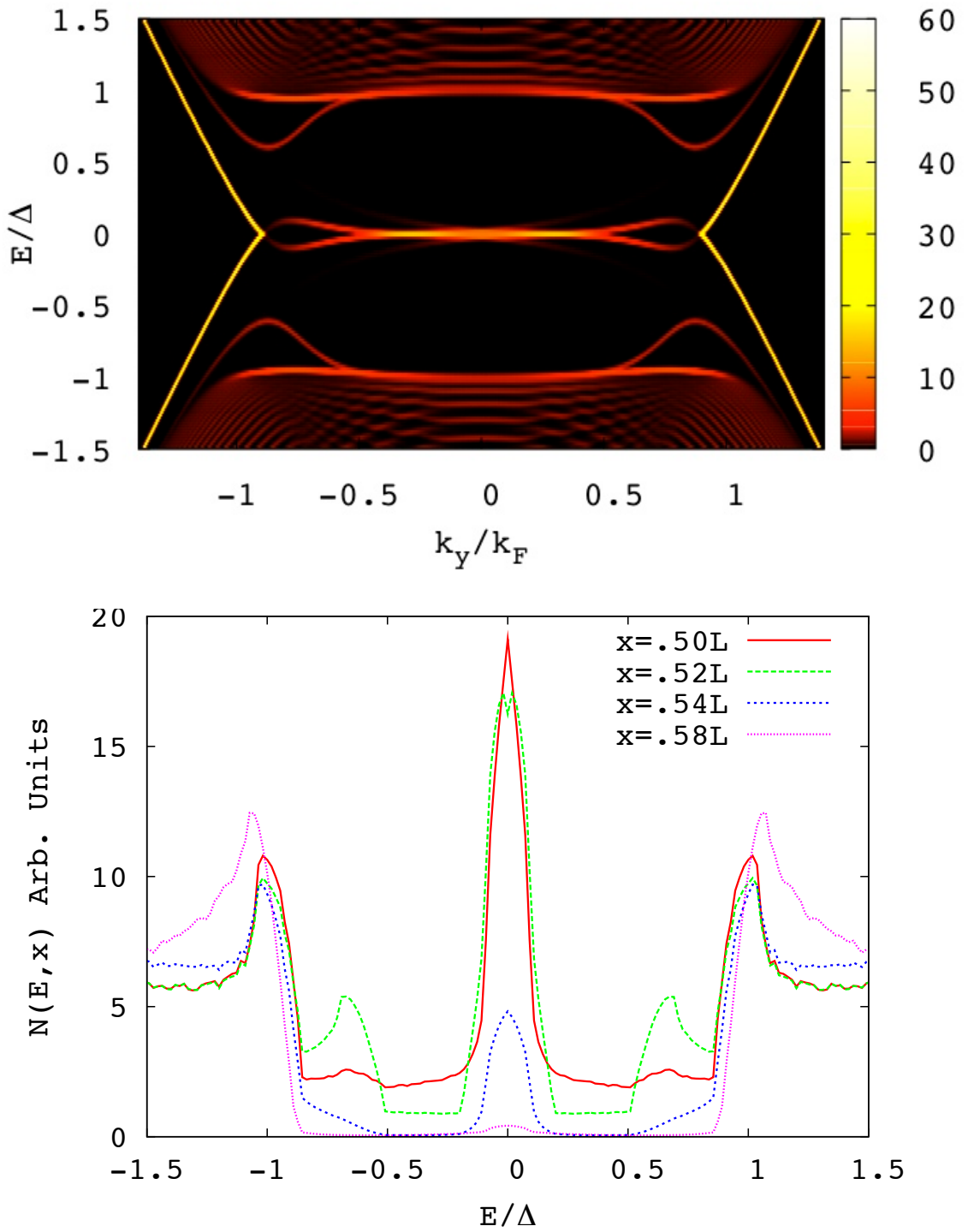


Figure 4.2: (color online) The local spectral function $A_{\uparrow}(E, k_y, x)$ (upper panel) and local density of states $N(E, x)$ (lower panel, red solid line) at the center of the junction, $x = 0.5L$. One sees “flat” Andreev bound states near zero energy for $-k_F < k_y < k_F$, and correspondingly a pronounced peak at zero energy in the LDOS in the lower panel. The lower panel also shows different LDOS away from the center, for x from $0.52L$ to $0.58L$.

4.3 Flat Bands in Spectrum

The upper panel of Fig. 4.2 shows the spectral function at the center of the junction, $A_{\uparrow}(E, k_y, x = 0.5L)$ (A_{\downarrow} is the same for this value of x), with $\mu=20\text{meV}$, $\Delta = 5.5\text{meV}$, $w = 0.04L$, $L = 2576\text{nm}$, $\hbar v_F=4.1 \text{ \AA eV}$, and the Fermi momentum $k_F = \mu/(\hbar v_F)$. In contrast to the $E \sim \hbar v_F k_y$ mode for $\mu = 0$, we see Andreev bound states (ABS) near zero energy within a wide region $-k_F < k_y < k_F$, where the slope $\hbar v_y = \partial E / \partial k_y$ approaches zero. The appearance of numerous crossings at exact zero energy for finite k_y also agrees with the model calculation above in Fig. 4.1d). Beyond this range, e.g. for $k_y > k_F$, the spectrum is reminiscent of the particle-hole folded dispersion of the helical metal, $E \sim \pm \hbar v_F(k_y - k_F)$.

As an approximate ansatz to describe the almost flat dispersion, we introduce the following phenomenological model for the ABS for large $\mu \gg \Delta$,

$$E/\Delta = c(k/k_F)^N, \quad (4.7)$$

where c is a constant and N is a large number. To fix N , we demand that the slope of the dispersion at energy $E \sim \Delta$ coincides with that of the bare dispersion, i.e., $\partial E / \partial k_y|_{E=\Delta} = \hbar v_F$. This gives an estimate of N ,

$$N \simeq \mu/\Delta. \quad (4.8)$$

Note that we are only concerned with the ABS dispersion near zero energy and its continuation beyond k_F . For wider junctions, additional subgap ABS appear at finite energies, and they are not described by Eq. (4.7). Our ansatz is inspired by the mathematical theory of Dirac points with multiple topological charge N as found in multi-layered system discussed in Ref. [92].

The flat dispersion implies a peak at zero energy in the local density of states. The lower panel of Fig. 4.2 shows the LDOS at the center of the junction, at the S-TI boundary, and slightly into the superconductor for the same junction parameters given above. While the zero energy peak becomes less pronounced when away from the junction center, it remains

clearly visible and persists even into the superconductor. Thus, the predicted flat ABS has a clear experimental signature in the tunneling conductance measurements.

The existence of two regimes including the flat Andreev bound states near zero energy is a general feature. We have carried out systematic, self-consistent simulations for the general case of an inhomogeneous chemical potential, e.g., $\mu(x) = \mu_{TI}$ within the TI region and $\mu(x) = \mu_S \neq \mu_{TI}$ inside the superconductors. The movie in the Supplementary Material shows the evolution of a typical spectrum for fixed μ_S with μ_{TI} gradually being increased from zero to μ_S [93]. We see the linear Majorana mode changing into the flat ABS. Select frames from a similar movie are laid out in figures 4.4 and ???. These frames show the evolution from Majorana to flat band as the chemical potential goes from $\mu = 0\text{eV}$ to $\mu = .014\text{eV}$ in the spectral function, $A(x = .5L, k_y, E)$ and DOS, $N(x = .5L, E)$.

4.4 Periodic π Junction

Having established the existence of nearly flat ABS around zero energy, now we systematically trace the evolution from the infinitesimal μ , linear dispersing (Majorana) regime to the large μ flat ABS regime. Also we would like to understand the details of ABS within its narrow ‘‘band width’’. To this end, we will consider a simple model which generalizes the π Josephson junction to periodic systems. Namely, in Eq. (4.2), the order parameter modulates sinusoidally in the x -direction with period $2a$ as schematically shown in the upper panel of Fig. 4.3,

$$\Delta(x) = \Delta \sin(\pi x/a). \quad (4.9)$$

The sign of the order parameter alternates. Thus the structure is effectively a periodic array of the π junctions discussed above in the limit $w \rightarrow 0$. One also recognizes that $\Delta(x)$ describes a stripe or Larkin-Ovchinnikov superconductor [94]. While such superconductors are hard to find, one may imagine bringing them in contact with a TI to realize the model considered here. Now the Hamiltonian \mathcal{H} has discrete translational symmetry in the x -direction, $\mathcal{H}(x) = \mathcal{H}(x + 2a)$. We can apply the Bloch-Floquet theorem and introduce

quasi-momentum k_x living in the Brillouin zone of $(-\pi/2a, \pi/2a)$. For the prescribed $\Delta(x)$, the energy spectrum $E(k_x, k_y)$ can be obtained by diagonalizing \mathcal{H} in k -space. Note that the TI (non-superconducting) region is shrunk to a point, only the homogeneous μ is left as tuning parameter.

The lower panel of Fig. 4.3 shows the spectrum $E(k_x = 0, k_y)$ for $a = 24\hbar v_F/\Delta$, $\mu = 4\Delta$. These flat ABS at zero energy do not show significant variation with k_x . We have checked that the wave function of these zero energy states are localized at the domain wall boundaries of the order parameter field, i.e., at $x = ma$ (red curve in the upper panel of Fig. 4.3). For example, the wave function of the $k_y = 0, k_x = 0, E \approx 0$ mode can be fit well with periodic Gaussian functions $|u(x)| \propto \exp(-1.85(\pi x/\sqrt{2}a)^2)$. Since a is large in this case, these results agree well with the single junction result before. The dispersion, for example, can be fit well using the ansatz in Eq. (4.7). The vanishing band width is, of course, only valid on coarse scales. Closer inspection, by blowing up the spectrum near zero as illustrated in Fig. 4.5, reveals the busy life of the ABS with N_c crossings at zero energy, where N_c scales linearly with μ , in agreement with Fig. 4.1d). Remarkably, all these fine details are compressed within a small energy range.

Fig. 4.5 illustrates the evolution of the ABS at low energies for the periodic structure as μ is increased from zero. For small value of $\mu = 0.83\Delta$, the linear Majorana dispersion splits into two, each developing a curvature, as the zero energy crossings move to finite k_y values. Further increasing μ , these two crossings are stretched further outward, while the dispersion within $k_y \in (-k_F, k_F)$ begin being bent and stretched to form the precursor of the flat band. At the same time, addition of new crossings introduces more twists. The number of crossing scales with $N_c \sim \mu/\Delta$. The spaghetti now becomes a rope, and looking from afar, it appears as a thin thread.

4.5 Summary

Flat bands are more novelties than the norm in condensed matter [95]. Recently, several authors have demonstrated that *surface* Andreev bound states with flat dispersion arise in certain topological superconductors, for example $\text{Cu}_x\text{Bi}_2\text{Se}_3$ [96] and non-centrosymmetric superconductors [97, 98]. Their existence can be traced back to the nontrivial topology associated with the gapped bulk, and thus are topologically protected. This mechanism giving rise to flat bands, via the bulk-boundary correspondence, differs from what is considered here. For example, in Ref. [96], a robust crossing at $k = 0$ is a crucial point in the argument, and the total number of zero energy crossings is guaranteed an odd number. In our case, states at $k_y = 0$ are gapped for finite size systems (or finite period $2a$). Despite these differences, the zero modes share the common trait that they are associated with the sign change of the order parameter when electrons are reflected at the surface or interface.

Several groups have successfully fabricated Josephson structures on Bi_2Se_3 of various length using a variety of superconducting materials including Al, Al/Ti, W, Nb, and Pb etc. [99, 100, 101, 102, 103]. Gate tunable supercurrent has been observed and argued to be due to the TI surface state [99]. Superconducting quantum interference devices based on such junctions have also been demonstrated [104, 102]. Thus the flat Andreev bound states at zero energy, and the zero bias conductance peak in the local density of states, predicted here should be experimentally accessible. Future work will explore control of these slowly dispersing Andreev levels working as qubits [105] when confinement in the y direction is also introduced. Our work also suggests the ac dynamics of the S-TI-S junctions will likely to be very complex featuring different regimes. The flat ABS at zero energy predicted for periodic junction arrays may potentially find technological applications. For example, a diverging density of states at the midgap may be used to generate microwave resonances.

We would like to thank Noah Bray-Ali, Liang Fu, and Takuya Kitagawa for helpful discussions.

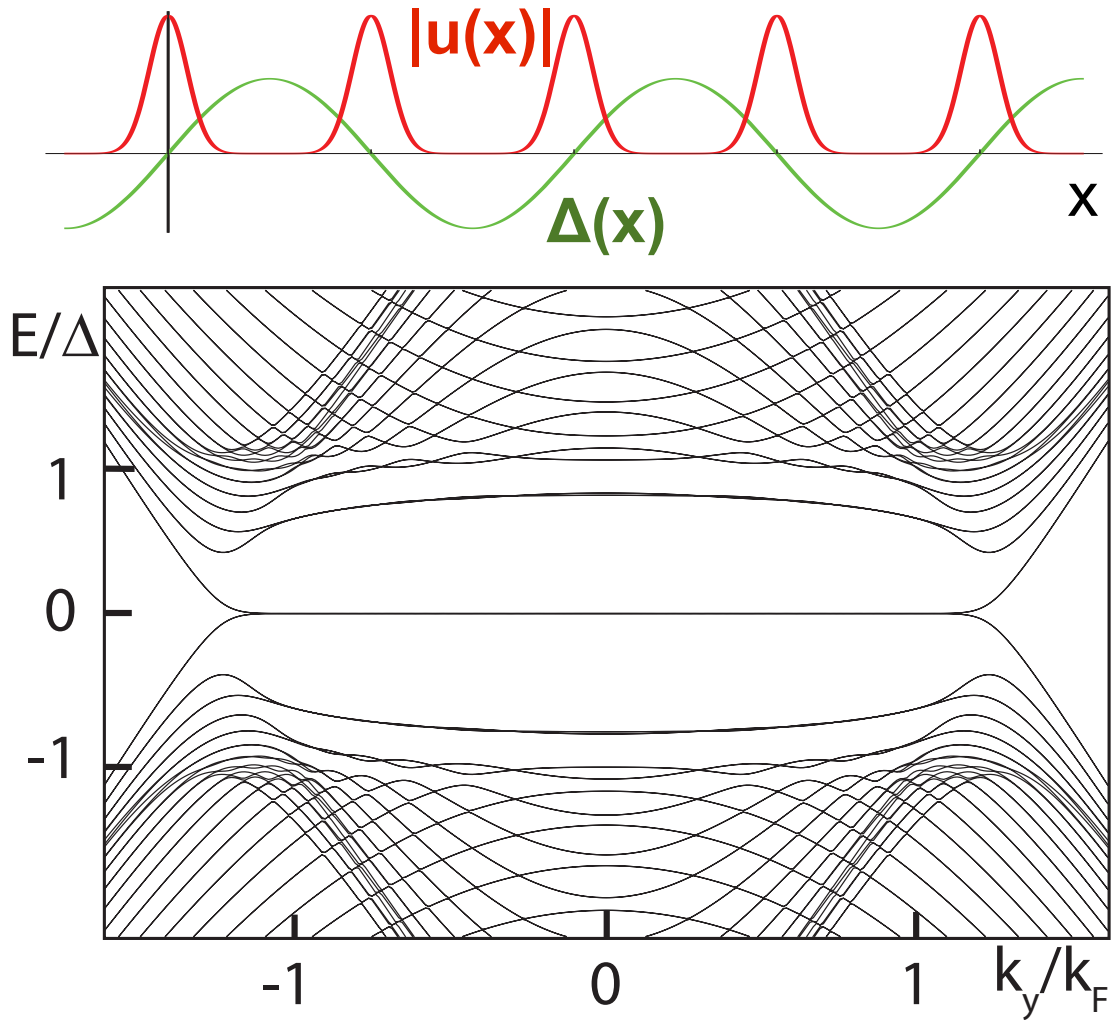


Figure 4.3: (color online) Upper panel: Schematic of the periodic proximity structure with $\Delta(x) = \Delta \sin(\pi x/a)$. The wave function $|u(x)|$ for the zero energy states are peaked at the domain wall boundaries, $x = ma$. Lower panel: Energy spectrum for $a = 24\hbar v_F/\Delta$ and $\mu = 4\Delta$ is flat at zero energy, which has fine structures upon closer inspection.

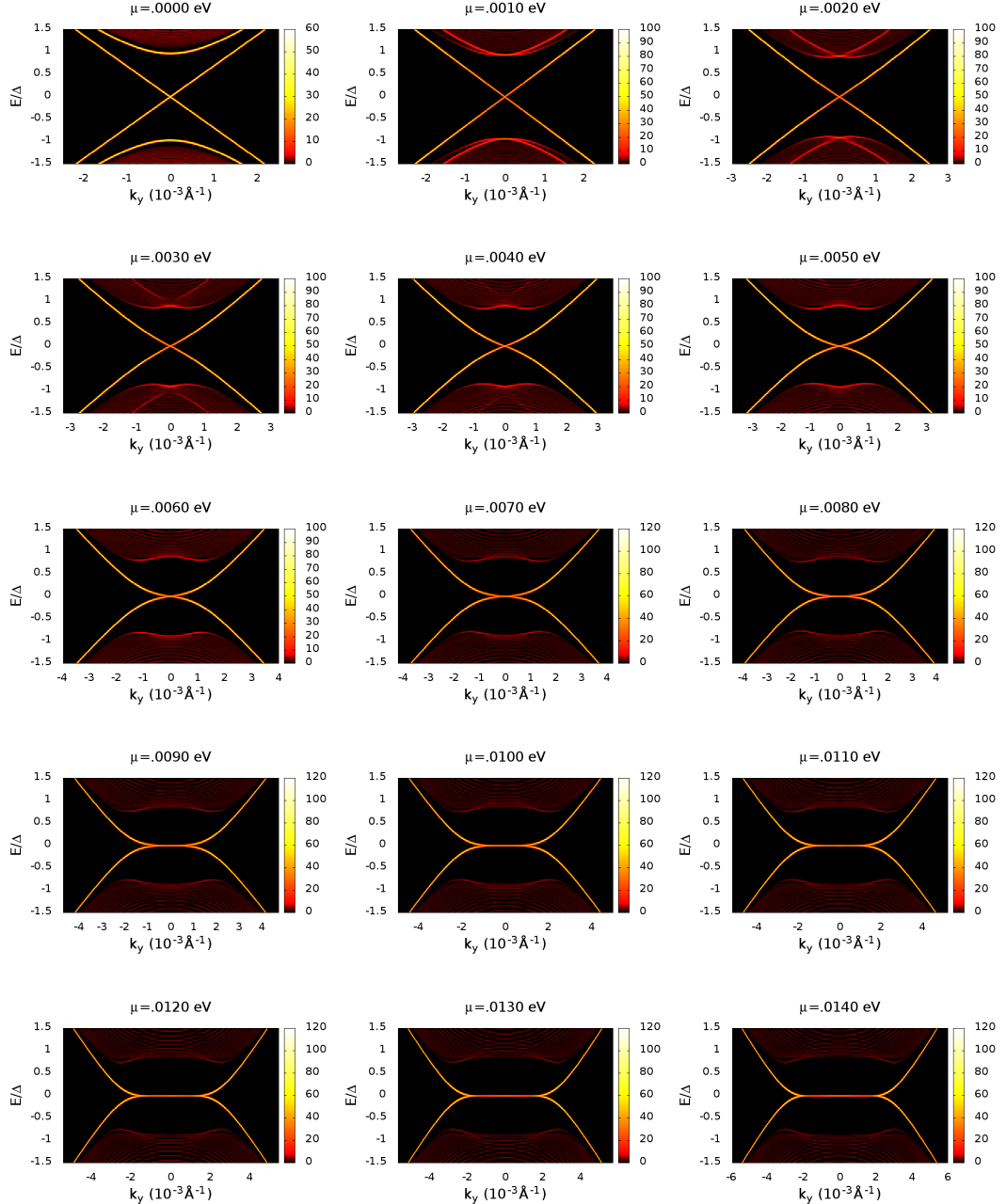


Figure 4.4: (color online) Spectral density function, $A(x = .5L, k_y, E)$, for values of μ from 0 eV to .14 eV. These images are used in a movie found online[2]. The linear dispersion ($E \sim k$) transitions to a flat band ($E \sim k^N$) as μ increases. This flat band is responsible for the peak in DOS in figure 4.2.

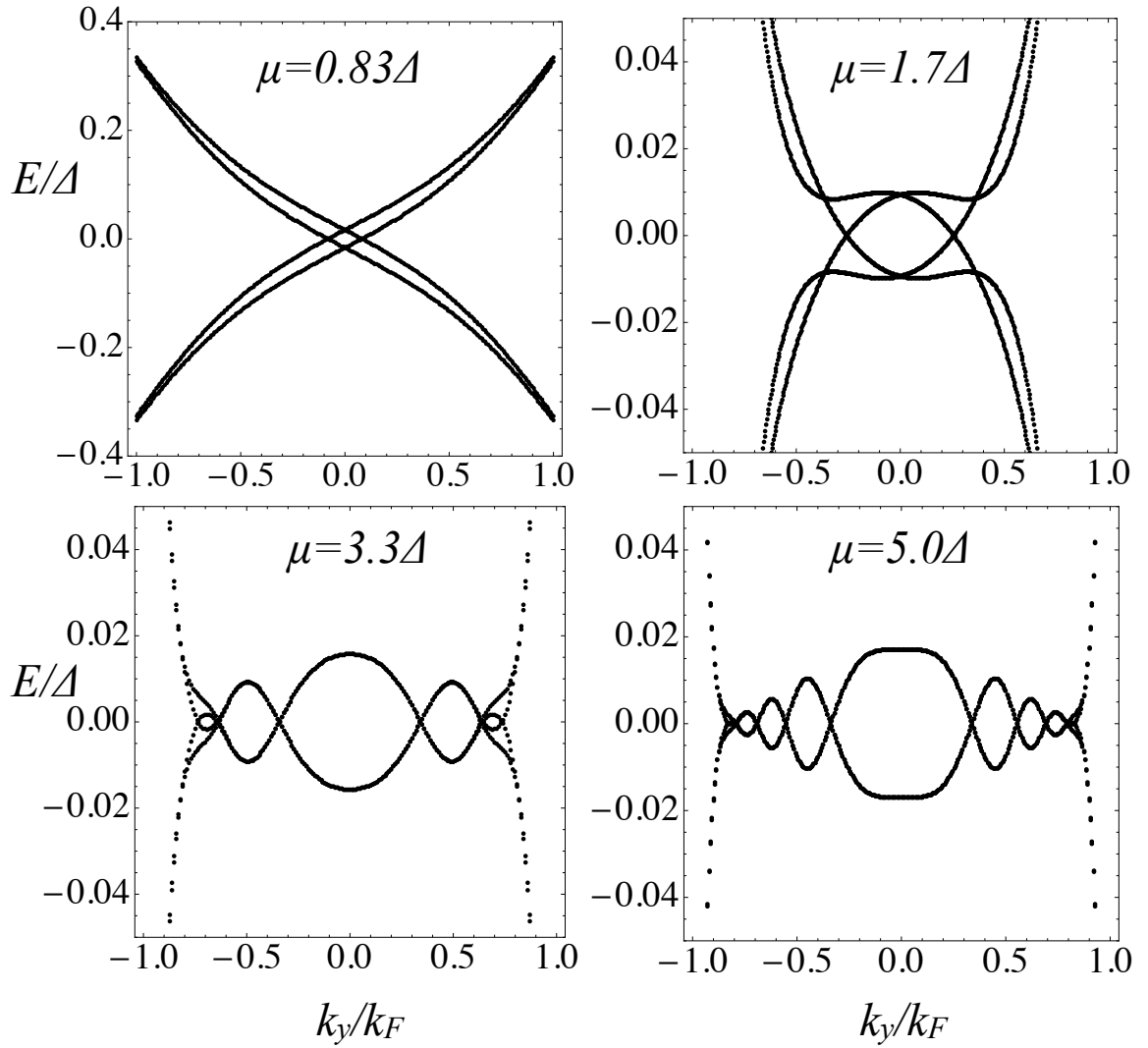


Figure 4.5: Fine structures in the energy spectrum of the periodic proximity structure with fixed $a = 12\hbar v_F/\Delta$ and increasing μ . The linearly dispersing Majorana spectrum at $\mu = 0$ splits and develops curvature to eventually become nearly flat within $(-k_F, k_F)$. The number of zero energy crossings increases with μ .

Chapter 5: Summary and Outlook

Thus far, we have delved into the physics of heterostructures of superconductors and topological insulators, starting with the TI's interaction with a metal and ending with a Josephson junction on the surface of the TI.

We found that electrons traveling from the metal to the surface of the TI can have a perfect spin flip under certain conditions. In addition we found that there occurs a hybridization between the metal and the surface of the TI, where the spectrum near the surface of the TI resembles that of the metal when the metal is strongly in contact with the TI. One possibility to extend the spin-flip mechanism found would be to have two surfaces of TIs sandwiching a metal. This flat 2D quantum device could have implications in spintronics applications.

In the study of the heterostructure of a superconductor and TI, we found that there does exist a subgap mode that penetrates deep into the superconductor. The parameters that describe this mode are renormalized from the respective bulk values of the individual materials due to the interplay between the TI and superconductor. A serious possibility on continuing this focus of microscopic simulation of a S-TI heterostructure is by simulating, more realistically, a Weyl superconductor, a periodic array of S-TI heterostructures with magnetic doping on the TI segments. The Weyl superconductor is an exotic gapless superconductor[106]. This prospective direction has experimental implications due to experimental realizations in magnetically doped TIs[17, 107, 108].

The Josephson junction on the surface of the TI gives rise to some very unique phenomena. The energy spectrum shows that when the junction's phase is π , the linear energy dispersion morphs into a flat, zero-slope dispersion as the chemical potential is tuned away from zero. This dispersion also presents a strong peak in the density of states. The progression from this study has a few directions. The flat band, illustrates that the quasiparticle

excitations have “low” kinetic energy and therefore secondary interactions, if they can be induced, can lead to new phases. And lastly, the ground state of the junction can be determined by comparing the free energy for different phase biases. This realistic study could precipitate further experiments to find the zero-energy Majorana mode.

Chapter A: Additional Papers

Anomalous edge states and topological phases of a kicked quantum Hall system

Mahmoud Lababidi, Indubala I. Satija, and Erhai Zhao

School of Physics, Astronomy, and Computational Sciences, George Mason University, Fairfax, VA 22030

Periodically driven quantum Hall system at a fixed flux is found to exhibit a series of phases featuring anomalous edge modes with the “wrong” chirality. This leads to pairs of counter-propagating chiral edge modes at each edge, in sharp contrast to stationary quantum Hall systems. We show that these anomalous edge modes are robust against weak disorder. They are essential in distinguishing phases with the same Chern and winding numbers. Their existence thus challenges the existing framework describing the topological properties of driven systems. We explore their origin using a simplified model and discuss their experimental signatures.

PACS numbers:

Cyclic time-evolutions of quantum systems are known to have interesting topological properties [1, 2]. Several groups recently showed that periodic driving can turn an ordinary band insulator (superconductor) into a Floquet topological insulator (superconductor) [3–10]. This provides a powerful way to engineer effective Hamiltonians that stroboscopically mimic stationary topological insulators [4, 5]. Moreover, a large class of topological phenomena in periodically driven many-body systems are unique and have no stationary counterparts. An early example is Thouless’s one-dimensional charge pump, where he showed that the charge transport is quantized and related to a topological invariant [11]. Other topological invariants for the time evolution operator in two and three dimensions have been constructed recently [3, 5, 10]. Yet a systematic classification of these invariants analogous to the periodic table of symmetry protected topological phases [12, 13] is still to be achieved.

In this paper, we identify new topological phenomena in a lattice integer quantum Hall (QH) system under cyclic driving with period T . For fixed magnetic flux, variations of the driving parameter induce topological phase transitions where the Chern numbers of the quasienergy bands change. We find multiple phases of the driven QH system featuring counter-propagating chiral edge modes at the each edge, and show they are robust against disorder. In particular, there appear “ π -modes”, pairs of edge modes with opposite chirality at quasienergy π/T . These anomalous edge modes differ from those found previously in other driven two-dimensional (2D) lattice models, where the edge modes at quasienergy π/T all propagate in the same direction and subsequently their number can be inferred either from the Chern number or the winding number [5, 10]. Here, these known topological invariants can not predict the number of edge modes of each chirality, but only their difference. For example, we find two phases (phase B and D below) having the same set of Chern and winding numbers but very different edge state spectra. New theoretical framework is needed to fully characterize and understand the the topological properties of such deceptively simple systems.

Our work is motivated by recent experimental achieve-

ments of artificial magnetic field for ultracold atoms [14, 15] and temporal modulation of optical lattices [16, 17]. We consider a model consisting of (spinless) fermionic atoms loaded onto a square optical lattice. Each site is labeled by vector $\mathbf{r} = n\hat{x} + m\hat{y}$, where n, m are integers, \hat{x} (\hat{y}) is the unit vector in the x (y) direction, and the lattice spacing a is set to be the length unit. The tight binding Hamiltonian has the form

$$H = -J_x \sum_{\mathbf{r}} |\mathbf{r} + \hat{x}\rangle \langle \mathbf{r}| - J_y \sum_{\mathbf{r}} |\mathbf{r} + \hat{y}\rangle \langle \mathbf{r}| + h.c. \quad (1)$$

Here, $|\mathbf{r}\rangle$ is the Wannier state localized at site \mathbf{r} . J_x (J_y) is the nearest neighbor hopping along the x (y) direction. We assume a uniform synthetic magnetic field B is applied in the $-z$ direction, and work in the Landau gauge, $A_x = 0$, $A_y = -Bx$. The flux per plaquette, in units of the flux quantum Φ_0 , is $\alpha = -Ba^2/\Phi_0$. Field B gives rise to the Peierls phase factor $e^{i2\pi n\alpha}$ in the hopping. For static J_x, J_y, H is the well known Hofstadter model [20].

We investigate a class of periodically driven quantum Hall systems described by H above, but with J_x and J_y being periodic functions of time t . We will focusing on the following driving protocol

$$\begin{aligned} J_x(t) &= J_x, \quad J_y(t) = 0, \quad 0 < \text{mod}(t, T) < \tau \\ J_x(t) &= 0, \quad J_y(t) = J_y, \quad \tau < \text{mod}(t, T) < T \end{aligned} \quad (2)$$

Namely, within one period T , the hopping along x is turned on during the interval $(0, \tau)$, while the hopping along y is turned on during the interval (τ, T) . We then have two independent driving parameters,

$$\theta_x = J_x\tau/\hbar, \quad \theta_y = J_y(T-\tau)/\hbar.$$

While it is hard to achieve in solid state systems, temporal modulation of J_x or J_y is straightforward to implement for cold atoms in optical lattices, e.g., by simply tuning the intensity of the laser. In the limit $\tau \rightarrow T$ and $(T-\tau)J_y \rightarrow \text{const}$, the driving protocol becomes

$$J_x(t) = J_x, \quad J_y(t) = J_y T \sum_j \delta(t - jT), \quad (3)$$

i.e., the y hopping is only turned on when $t = jT$, with j any integer. In this limit, $\theta_x = J_x T / \hbar$, $\theta_y = J_y T / \hbar$. We will simplify refer to systems described by (2) or (3) as kicked quantum Hall systems, because (3) resembles the well studied kicked rotors.

The time evolution operator of the system, defined by $|\psi(t)\rangle = U(t)|\psi(0)\rangle$, has the formal solution $U(t) = \mathcal{T} \exp[-i \int_0^t H(t') dt']$, where \mathcal{T} denotes time-ordering and we set $\hbar = 1$ throughout. The discrete translation symmetry $H(t) = H(t+T)$ leads to a convenient basis $\{|\phi_\ell\rangle\}$, defined as the eigenmodes of Floquet operator $U(T)$,

$$U(T)|\phi_\ell\rangle = e^{-i\omega_\ell T}|\phi_\ell\rangle.$$

Here the quasienergy ω_ℓ , by definition, is equivalent to $\omega_\ell + 2p\pi/T$ for any integer p and lives within the quasienergy Brillouin zone (QBZ), $\omega \in [-\pi/T, \pi/T]$. For rational flux $\alpha = 1/q$, U is a $q \times q$ matrix in momentum space and there are q quasienergy bands. For convenience, we label the lowest band within the QBZ with $\ell = 1$, and the subsequent bands at increasingly higher quasienergies with $\ell = 2, 3, \dots, q$. Correspondingly, we call the gap below the ℓ -th band the ℓ -th gap. For example, the gap around $\pm\pi/T$ is the first gap. The Chern number for the ℓ -th quasienergy band can be defined analogous to the stationary case [21]

$$c_\ell = \frac{i}{2\pi} \int dk_x dk_y [\partial_{k_x} \phi_\ell^*(\mathbf{k}) \partial_{k_y} \phi_\ell(\mathbf{k}) - c.c.],$$

where the integration is over the magnetic Brillouin zone, and $\phi_\ell(\mathbf{k})$ is the ℓ -th eigenwavefunction of $U(\mathbf{k}, T)$.

Figure 1 displays four representative quasienergy spectra of a finite slab of length L in the x direction under periodic driving (2). As in static QH systems, we observe edge states forming within the quasienergy gaps. Consider the left edge ($x = 0$) and let us denote the number of chiral edge modes propagating in the \hat{y} ($-\hat{y}$) direction by n_ℓ^+ (n_ℓ^-). For driven 2D systems, the Chern numbers are generally insufficient to predict (n_ℓ^+, n_ℓ^-) . Instead, as shown by Rudner et al [10], the net chirality of the edge modes inside the ℓ -th quasienergy gap, $w_\ell \equiv n_\ell^+ - n_\ell^-$, is given by the following winding number

$$w_\ell = \int \frac{dk_x dk_y dt}{24\pi^2} \epsilon^{\mu\nu\rho} \text{Tr} [(u^{-1} \partial_\mu u)(u^{-1} \partial_\nu u)(u^{-1} \partial_\rho u)].$$

Here $\mu, \nu, \rho = 1, 2, 3$ corresponds to k_x, k_y, t respectively, and $u(\mathbf{k}, t)$ is a smooth extrapolation of $U(\mathbf{k}, t)$ [10]

$$u(\mathbf{k}, t) = U(\mathbf{k}, 2t) \theta(T/2 - t) + e^{-i\mathcal{H}(\mathbf{k})2(T-t)} \theta(t - T/2),$$

where $\mathcal{H}(\mathbf{k}) = -(i/T) \log U(T)$ is the effective Hamiltonian with the branch cut of the logarithm chosen at quasienergies within the ℓ -th gap. In fact, as shown in Ref. [10], the Chern numbers can be inferred from the winding numbers by the relation $c_\ell = w_{\ell+1} - w_\ell$.

Applying the theoretical analysis outlined above, we obtain Fig. 2, the zero temperature “phase diagram”

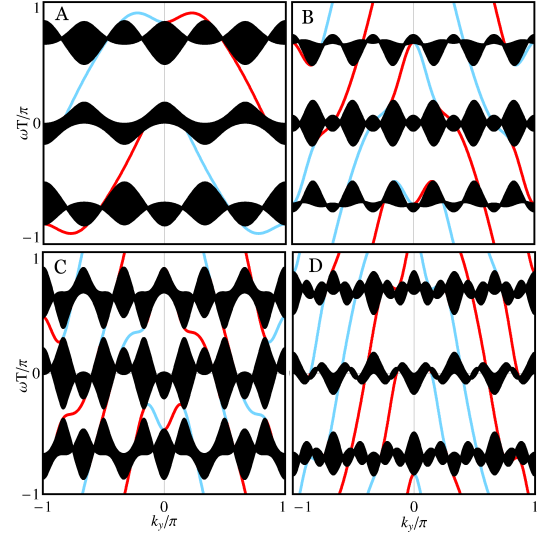


FIG. 1: (color online) Quasienergy spectra of a finite (in the x -direction) slab of periodically driven quantum Hall system at flux $-1/3$ and fixed $\theta_x = \pi/3$. The four panels, $\theta_y = 0.5\pi, \pi, 1.2\pi$, and 1.5π , correspond to phase A, B, C, and D, respectively, shown in Fig. 2. Edge states localized on the left (right) edge are shown in blue (red).

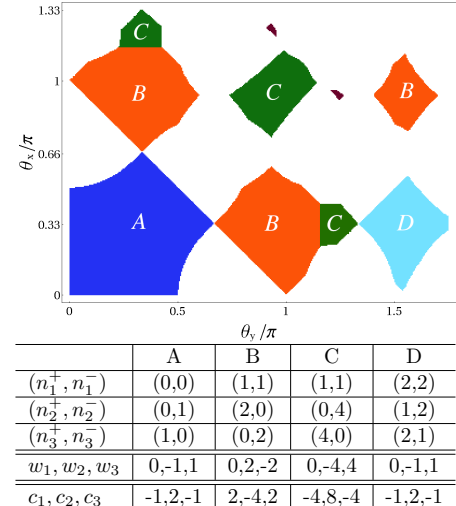


FIG. 2: (color online) Phase diagram of a periodically driven quantum Hall system in the plane spanned by driving parameter θ_x and θ_y at flux $\alpha = -1/3$. Each phase (A, B, C, and D) is characterized by $\{(n_\ell^+, n_\ell^-)\}$, the number of modes within the ℓ -th gap and propagating along $\pm\hat{y}$ at the left edge. The winding number of the ℓ -th gap $w_\ell = n_\ell^+ - n_\ell^-$, and the Chern number of the ℓ -th band $c_\ell = w_{\ell+1} - w_\ell$ (see main text).

of the kicked quantum Hall system in terms of two independent driving parameters, θ_x and θ_y . It showcases four representative phases, labelled by A to D, for flux $\alpha = -1/3$. All of them feature three well defined quasienergy bands and three gaps, while the spectrum in the rest of the phase diagram is largely gapless. The corresponding spectrum of each phase in the slab geometry can be found in Figure 1. The table in Fig. 2 summarizes what we know about each phase: the number of edge modes on the left edge propagating in the $\pm\hat{y}$ direction, (n_ℓ^+, n_ℓ^-) , inside the ℓ -th gap; the winding number w_ℓ of the ℓ -th gap; and the Chern number c_ℓ of the ℓ -th band. Note that w_ℓ and c_ℓ are calculated independently from the bulk spectrum. We also note that at the phase transition points where the gap closes, the Chern numbers always change by a multiple of 3, consistent with the Diophantine equation [18]. In what follows, we discuss in turn each of these phases.

(A). The main features of phase A can be understood by considering the fast driving limit, $\theta_1, \theta_2 \ll 1$. The effective Hamiltonian \mathcal{H} , takes the same form of H in Eq. (1), only with the bare hopping replaced by the effective hopping $J_x \rightarrow J_x\tau/T$, $J_y \rightarrow J_y(1-\tau/T)$. The driven system in phase A stroboscopically mimics a static QH system with the same flux but renormalized hopping. In particular, there is no edge state crossing the gap centered round $\pm\pi/T$.

(B). Phase B highlights a remarkable consequence of periodic driving: there are now two chiral edge modes inside the second and third gap. This is in sharp contrast to phase A, not only in the number of edge modes, but also in their chirality. Thus, simple periodic modulations of hopping proposed here is sufficient to change both the number and the chirality of edge states. More importantly, phase B contains a pair of counter-propagating edge modes, dubbed “ π -modes”, inside the first gap at the QBZ boundary $\pm\pi/T$. Note that the net chirality is zero, $w_1 = n_1^+ - n_1^- = 0$. Previous work on driven 2D systems [5, 10] also found chiral edge modes at $\pm\pi/T$. However, there the π -modes all have the same chirality, and the nearby bands are trivial with zero Chern number. Then the following two questions naturally arise. What is the origin of such pairs of π -modes? Are they robust against perturbations? Counter-propagating chiral edge modes at the same edge are usually argued to be unstable, because backscattering may couple them leading to the opening of a gap. However, a closer inspection reveals that the two π -modes of opposite chirality (shown in blue for the left edge) cross the QBZ boundary at k_y^a and $k_y^b = k_y^a + \pi$ respectively, where the precise value of k_y^a depends on $\theta_{x,y}$. Thus backscattering, $k_y \rightarrow -k_y$, does not directly hybridize them. We have verified the stability of the π -modes against disorder by numerically solving for the spectra of finite systems of dimension $L_x \times L_y$ in the presence of static on-site disorder potential, $\delta\mu(\mathbf{r}) \in (-\Delta, \Delta)$. To resolve the number of edge states within

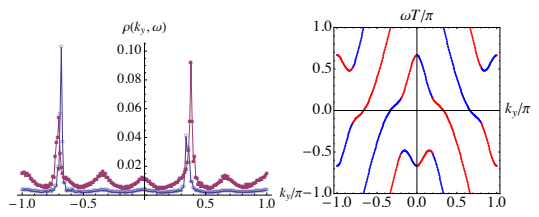


FIG. 3: (color online) Left: Robust edge states in the presence of disorder $\Delta = 0.3J_x$. The two peaks in the spectral function for $\omega = 0.95\pi/T$ (circle) and $0.85\pi/T$ (filled square) suggest two π -modes at the left edge, consistent with Fig. 1B. Right: Winding of the quasienergy spectrum of a two-leg ladder. Red (blue) indicates the eigenstate is predominantly on the right (left) leg. $\alpha = -1/3$, $\theta_x = \pi/3$, $\theta_y = \pi$.

the first gap, we define spectral function $\rho(k_y, \omega) = \sum_{n,x < L_x/2} \delta(\omega - E_n) |\sum_y \psi_n(x, y) e^{-ik_y y} / L_y|^2$, where the sum over x is restricted to the left half of the slab, E_n and ψ_n are the n -th quasienergy and the corresponding eigenwavefunction, respectively. As shown in Fig. 3, $\rho(k_y, \omega)$ for $\Delta = 0.3J_x$ is peaked at two different k_y values, with separated approximately by π , suggesting two edge modes near π/T . These evidences indicate that the π -modes are stable against weak disorder.

(C) Phase C is very similar to phase B. The only difference is that there are 4 (instead of 2 in phase B) chiral edge modes propagating in the same direction inside the second and third gap. This is yet another example that Chern numbers of the quasi-energy bands can be controlled by periodic driving.

(D) Phase D is qualitatively different from all other phases. Firstly, near the QBZ boundary, there are two pairs of counter-propagating π -modes, $n_1^+ = n_1^- = 2$. Secondly, the edge states within the second and third gap also contain counter-propagating modes: two of the edge modes propagate in the same direction, but the remaining one propagates in the opposite direction. For example, $n_2^+ = 1$, $n_2^- = 2$. Although phase D has exactly the same set of $\{w_\ell\}$ and $\{c_\ell\}$ as phase A, it has counter-propagating edge modes in all three quasienergy gaps that are robust against weak disorder. The existence of phase D thus demonstrates unequivocally that neither the winding numbers or Chern numbers give a complete characterization of the driven QH system.

Below we shed more light on the anomalous edge modes, and the successive phase transitions between the phases, using a simple model which allows analytical analysis. Consider a two-leg ladder extending infinitely in the y direction. The ladder spectrum already contains all the essential features of edge states found in large systems as shown in Figure 1. For flux $1/3$, the Floquet operator of the ladder is $U(k_y, T) = e^{i\theta_y} [-\cos k_y + \sigma_z \sqrt{3} \sin k_y] e^{i\theta_x \sigma_x}$, where the σ 's are Pauli matrices in the orbital space. It

follows that the effective Hamiltonian of the ladder

$$\mathcal{H}(k_y)T = \theta_y \cos k_y + \boldsymbol{\sigma} \cdot \mathbf{h}(k_y),$$

with $h(k_y) = |\mathbf{h}| = \arccos[\cos \theta_x \cos(\theta_y \sqrt{3} \sin k_y)]$. Thus, the quasienergy spectrum has two bands (branches),

$$\omega_{\pm}(k_y)T = \theta_y \cos k_y \pm h(k_y), \quad (\text{mod } 2\pi).$$

Figure 3 shows the ladder spectrum for $\theta_x = \pi/3$ and $\theta_y = \pi$ (phase B). For vanishingly small θ_y , the bands are almost flat, $\omega_{\pm} \simeq \pm \theta_x/T$. As θ_y is increased, the curvature and the width of both bands increase. Beyond a critical value $\theta_y \simeq 0.57\pi$, the top of the ω_+ band (and the bottom of the ω_- band) grows beyond the QBZ, and re-enters from the opposite side of the QBZ. Consequently, the number of states crossing the QBZ boundary, $n_1^+ + n_1^-$, jumps from 0 to 4, marking a transition from phase A to phase B. From this perspective, the pair of π -modes results from the winding of quasienergy across the QBZ boundary as driving in the y -direction (θ_y) is increased. Similarly, for $\theta_y > 1.33\pi$, both the top and bottom of ω_{\pm} exceed the QBZ, giving rise to two pairs of π -modes at each edge in phase D. When folded into the QBZ, they intrude into the second and third bulk gap, leading to the anomalous edge mode propagating in the “wrong” direction. Remarkably, the chirality of the edge modes in Fig. 1 agrees with the predictions of the ladder model in Fig. 3. That the π -modes always appear in pairs is guaranteed by a “hidden” symmetry of $U(T)$,

$$U(k_y + \pi, T) = \sigma_z U^*(k_y, T) \sigma_z.$$

Accordingly, a quasienergy eigenvalue of $U(k_y, T)$ at π/T implies another eigenvalue at $k_y + \pi$ with quasienergy $-\pi/T$ which is equivalent to π/T . Therefore the edge states can only cross $\pm \pi/T$ even number of times at k_y values differing by π [25]. Such pairs of π -modes are reminiscent of, and of course fundamentally different from, the counter-propagating edge modes protected by time-reversal symmetry in quantum spin Hall effect [22].

The anomalous edge modes unique to periodically driven QH system can be detected experimentally by momentum-resolved radio-frequency spectroscopy [23], which measures the spectral function $\rho(k_y, \omega)$. Atoms occupying the π -mode at quasienergy ω absorb radio-frequency photon and undergo a vertical transition to an empty hyperfine state which can be subsequently imaged. For example, in phase B, the measured spectral function will feature peaks at $k_y^{a,b}$ and energy $E_n = (2n + 1)\pi/T$. This method can also be used to observe chiral edge states within the second and third quasienergy gap. Alternatively, the edge currents can be probed by quantum quenches that convert them into density patterns [24].

The static QH system is home to the Hofstadter butterfly, with an intricate band structure whose Chern numbers are given by the Diophantine equation. Periodic

driving gives rise to new effective Hamiltonians and a rich landscape of phases which not only have new Chern numbers but also anomalous edge states and demands new ways to characterize topology of exotic states of matter.

We thank Brandon Anderson, Michael Levin, Xiaopeng Li, Takuya Kitagawa, and Mark Rudner for helpful discussions. This work is supported by AFOSR, NIST, and NSF (ML and EZ). EZ also acknowledge the support from KITP through NSF PHY11-25915.

-
- [1] M. V. Berry, Royal Society of London Proceedings Series A **392**, 45 (1984).
 - [2] Y. Aharonov and J. Anandan, Phys. Rev. Lett. **58**, 1593 (1987), URL <http://link.aps.org/doi/10.1103/PhysRevLett.58.1593>.
 - [3] T. Oka and H. Aoki, Phys. Rev. B **79**, 081406 (2009), URL <http://link.aps.org/doi/10.1103/PhysRevB.79.081406>.
 - [4] N. H. Lindner, G. Refael, and V. Galitski, Nature Physics **7**, 490 (2011), ISSN 1745-2473, URL <http://www.nature.com/nphys/journal/v7/n6/full/nphys1926.html>.
 - [5] T. Kitagawa, E. Berg, M. Rudner, and E. Demler, Physical Review B **82**, 235114 (2010), URL <http://link.aps.org/doi/10.1103/PhysRevB.82.235114>.
 - [6] N. H. Lindner, D. L. Bergman, G. Refael, and V. Galitski, arXiv:1111.4518 (2011), URL <http://arxiv.org/abs/1111.4518>.
 - [7] T. Kitagawa, T. Oka, A. Brataas, L. Fu, and E. Demler, Physical Review B **84**, 235108 (2011), URL <http://link.aps.org/doi/10.1103/PhysRevB.84.235108>.
 - [8] L. Jiang, T. Kitagawa, J. Alicea, A. R. Akhmerov, D. Pekker, G. Refael, J. I. Cirac, E. Demler, M. D. Lukin, and P. Zoller, Physical Review Letters **106**, 220402 (2011), URL <http://link.aps.org/doi/10.1103/PhysRevLett.106.220402>.
 - [9] Z. Gu, H. A. Fertig, D. P. Arovas, and A. Auerbach, Physical Review Letters **107**, 216601 (2011), URL <http://link.aps.org/doi/10.1103/PhysRevLett.107.216601>.
 - [10] M. S. Rudner, N. H. Lindner, E. Berg, and M. Levin, arXiv:1212.3324 (2012), URL <http://arxiv.org/abs/1212.3324>.
 - [11] D. J. Thouless, Phys. Rev. B **27**, 6083 (1983), URL <http://link.aps.org/doi/10.1103/PhysRevB.27.6083>.
 - [12] A. Kitaev, AIP Conf. Proc. **1134**, 22 (2009).
 - [13] A. P. Schnyder, S. Ryu, A. Furusaki, and A. W. W. Ludwig, Phys. Rev. B **78**, 195125 (2008), URL <http://link.aps.org/doi/10.1103/PhysRevB.78.195125>.
 - [14] Y. J. Lin, R. L. Compton, K. Jimenez-Garcia, J. V. Porto, and I. B. Spielman, Nature **462**, 628 (2009), URL <http://dx.doi.org/10.1038/nature08609>.
 - [15] M. Aidelsburger, M. Atala, S. Nascimbène, S. Trotzky, Y.-A. Chen, and I. Bloch, Phys. Rev. Lett. **107**, 255301 (2011), URL <http://link.aps.org/doi/10.1103/PhysRevLett.107.255301>.
 - [16] J. Struck, C. Ölschläger, M. Weinberg, P. Hauke, J. Simonet, A. Eckardt, M. Lewenstein, K. Sengstock, and P. Windpassinger, Phys. Rev. Lett. **108**,

- 225304 (2012), URL <http://link.aps.org/doi/10.1103/PhysRevLett.108.225304>.
- [17] P. Hauke, O. Tielemans, A. Celi, C. Ölschläger, J. Simonet, J. Struck, M. Weinberg, P. Windpassinger, K. Sengstock, M. Lewenstein, et al., Phys. Rev. Lett. **109**, 145301 (2012), URL <http://link.aps.org/doi/10.1103/PhysRevLett.109.145301>.
- [18] I. Dana, Y. Avron, and J. Zak, Journal of Physics C: Solid State Physics **18**, L679 (1985), URL <http://stacks.iop.org/0022-3719/18/i=22/a=004>.
- [19] Y. Hatsugai and M. Kohmoto, Phys. Rev. B **42**, 8282 (1990), URL <http://link.aps.org/doi/10.1103/PhysRevB.42.8282>.
- [20] D. R. Hofstadter, Physical Review B **14**, 2239 (1976), URL <http://link.aps.org/doi/10.1103/PhysRevB.14.2239>.
- [21] D. J. Thouless, M. Kohmoto, M. P. Nightingale, and M. den Nijs, Physical Review Letters **49**, 405 (1982), URL <http://link.aps.org/doi/10.1103/PhysRevLett.49.405>.
- [22] C. L. Kane and E. J. Mele, Phys. Rev. Lett. **95**, 226801 (2005), URL <http://link.aps.org/doi/10.1103/PhysRevLett.95.226801>.
- [23] J. T. Stewart, J. P. Gaebler, and D. S. Jin, Nature **454**, 744 (2008), URL <http://dx.doi.org/10.1038/nature07172>.
- [24] M. Killi and A. Paramekanti, Physical Review A **85**, 061606 (2012), URL <http://link.aps.org/doi/10.1103/PhysRevA.85.061606>.
- [25] The argument can be generalized to slab of any size L .

Robustness of single-qubit geometric gate against systematic error

J. T. Thomas, Mahmoud Lababidi, and Mingzhen Tian

School of Physics, Astronomy and Computational Sciences, George Mason University, Fairfax, Virginia 22030, USA

(Received 30 June 2010; revised manuscript received 4 August 2011; published 24 October 2011)

Universal single-qubit gates are constructed from a basic Bloch rotation operator realized through nonadiabatic Abelian geometric phase. The driving Hamiltonian in a generic two-level model is parameterized using controllable physical variables. The fidelity of the basic geometric rotation operator is investigated in the presence of systematic error in control parameters, such as the driving pulse area and frequency detuning. Compared to a conventional dynamic rotation, the geometric rotation shows improved fidelity.

DOI: 10.1103/PhysRevA.84.042335

PACS number(s): 03.67.Pp, 03.67.Lx, 03.65.Vf

I. INTRODUCTION

In the implementation of scalable quantum information processing, a key challenge is to achieve controlled quantum state preparation and manipulation with high fidelity in the presence of imperfections. In the commonly adapted quantum computing circuit model [1], this requires a set of robust universal quantum gates. Quantum gates degrade due to both imperfections in the control Hamiltonian and decoherence in the physical qubit system during the gate operation. When the operation time is kept much shorter than the qubit coherence time, the systematic error and random noise in the control Hamiltonian become the dominant causes for the operation error [2]. The quality of a quantum gate is usually characterized by gate fidelity or error rate per gate. A scalable computation can be achieved through quantum error correction [3], provided the error rate is smaller than a certain threshold, usually 10^{-4} , or a fidelity above 99.999% [2,4].

In recent years various all-geometric schemes based on quantum holonomy have been considered effective ways to minimize the operation errors caused by random noise. A control Hamiltonian is designed to drive a qubit along a specific path so that the resulting state transformation is affected only by the global geometry of the quantum system, not by the details of the evolution paths that are usually fluctuating due to noises in the control Hamiltonian [5–13]. The all-geometric approaches existing so far utilize either Abelian- or non-Abelian holonomy, which results in the state transformation expressed as a phase change or a unitary matrix, respectively. The non-Abelian geometric approach, usually called holonomic quantum computation [5], has been considered as a novel quantum computation model and proven fault tolerant under the adiabatic condition [14]. In the circuit model, holonomic quantum gates have been investigated for robustness against random parametric noise, most of them in adiabatic cases [15], which requires a long operation time. Breaking the adiabatic limit to shorten the operation time brings the quantum gates into no pure-geometric regimes [16]. Non-Abelian quantum gates have not been experimentally demonstrated mainly due to the difficulties in manipulation and measurement of multiple degenerate quantum states. On the other hand, the Abelian all-geometric approach is relatively simple since the gate operations are performed on nondegenerate two-level qubits through either Berry's phase [17] in an adiabatic evolution or Aharonov-Anandan (A-A) phase [18] in a nonadiabatic process. Abelian geometric gates

have been proposed and demonstrated in almost all viable qubit systems so far, including [8–13] NMR, cold atoms or ions, photons, superconducting circuits, quantum dots, cavity QED, and atomic ensembles in solids. The fault tolerance against errors in the control Hamiltonian is still under investigation, and fidelity analysis has been focused on the effect of the random error [19–22]. The results, however, are still less conclusive for a general two-level system. In addition, the effects from seemingly simple systematic errors have not yet been addressed.

In this paper we focus on the robustness of a type of nonadiabatic Abelian geometric gates against systematic errors in the control parameters. Based on A-A phase, two noncommutable basic Bloch rotations were previously proposed and experimentally demonstrated, which can be used to compose any universal single-qubit gate [12]. The Hamiltonians controlling the rotations are made of a special type of composite pulses that drive the eigenvectors of the system through closed paths in the projective Hilbert space (a Bloch sphere), eliminating the dynamic phase. This paper generalizes the basic rotations as a rotation operator that suffices for making any single-qubit gates. Since the two-level qubit and the driving Hamiltonian are parameterized as a Bloch vector and a torque vector, respectively, evolving on the Bloch sphere this scheme is applicable to a generic two-level qubit. We are able to use the rotation operator to analyze the gate fidelity, which is independent of the qubit state. The fidelity is calculated in the presence of systematic errors in the control parameters, such as pulse area and frequency detuning. The geometric rotation is compared with conventional dynamic rotation. The link between the geometricity and high operation fidelity is discussed.

II. UNIVERSAL QUANTUM GATES AND BASIC BLOCH ROTATION

The quantum state of a qubit $|\psi\rangle = \cos\frac{\alpha}{2}|0\rangle + e^{i\beta}\sin\frac{\alpha}{2}|1\rangle$ can be represented by a Bloch vector $\vec{r} = (\sin\alpha\cos\beta, \sin\alpha\sin\beta, \cos\alpha)$ on the Bloch sphere as shown in Fig. 1(a). The polar angle α varies from 0 to π and the azimuthal angle β from 0 to 2π . A rotation on the Bloch sphere represents a universal quantum gate that can be expressed as

$$U_{\vec{n}}(\theta) = \exp(-i\vec{\sigma} \cdot \vec{n}\theta/2) = \cos(\theta/2)I - i\sin(\theta/2)\vec{\sigma} \cdot \vec{n}, \quad (1)$$

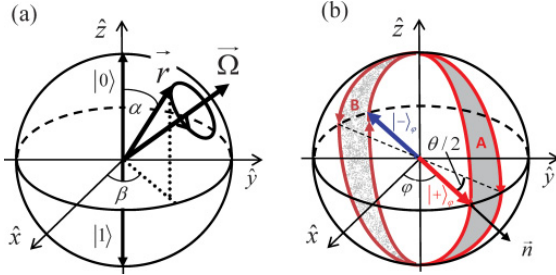


FIG. 1. (Color online) (a) Bloch vector \vec{r} rotates around Rabi vector $\vec{\Omega}$ on the Bloch sphere. (b) Geometric paths A and B for basis vectors $|+\rangle_\phi$ and $|-\rangle_\phi$, respectively, to accomplish rotation $U(\theta, \varphi)$ in Eq. (2), where \vec{n} is the rotation axis and θ the rotation angle.

where θ is the angle of rotation around axis \vec{n} , and I and $\vec{\sigma} = (\sigma_x, \sigma_y, \sigma_z)$ are the identity and Pauli matrices, respectively.

Since a rotation around an arbitrary axis can be made by rotations around two unparallel axes in the x - y plane, the problem of making a universal set of single-qubit gates reduces to making rotations around $\vec{n} = (\cos \varphi, \sin \varphi, 0)$ in the x - y plane, where φ is the angle between the x axis and the rotation axis \vec{n} . The rotation operator becomes

$$U(\theta, \varphi) = \cos(\theta/2)I - i \sin(\theta/2)(\cos \varphi \sigma_x + \sin \varphi \sigma_y), \quad (2)$$

where φ defines the rotation axis and θ the rotation angle. Any single-qubit gate can be made of at most three rotations characterized by such an operator with controllable φ and θ [23].

In a generic two-level model, the motion of the Bloch vector obeys the Bloch equation [24], $d\vec{r}/dt = \vec{\Omega} \times \vec{r}$, where the Bloch vector represents the quantum state and the driving Hamiltonian $H = (\hbar \Delta/2)\sigma_z + (\hbar \Omega_0/2)(\cos \varphi \sigma_x + \sin \varphi \sigma_y)$ in the rotating frame is parameterized by the torque given by the Rabi vector $\vec{\Omega}$. As shown in Fig. 1(a), the Bloch vector rotates around the driving torque by an angle of the pulse area $\theta = \Omega \tau$, where τ is the duration for a constant torque acting on the Bloch vector. The evolution of a two-level system, such as an atom or spin-1/2 particle, can be modeled as an effective dipole moment driven by an effective field near the resonance of the transition between the two energy levels of the qubit [24]. The driving field, $F(t) = \Omega_0 \cos(\omega t + \phi)$, determines the Rabi vector to be $\vec{\Omega} = (-\Omega_0 \cos \phi, -\Omega_0 \sin \phi, \Delta)$. The field amplitude Ω_0 is defined as Rabi frequency and takes into account the effective dipole moment; ϕ is the phase of the field; and Δ is the frequency detuning between the driving field and the resonance of the two-level system. These are the parameters that define the quantum gate operation and control the motion of the Bloch vector.

Conventionally, to make the rotation around an axis $\vec{n} = (\cos \varphi, \sin \varphi, 0)$ in the x - y plane as in Eq. (2), a pulse of an on-resonance field with constant amplitude Ω_0 , phase $(\varphi + \pi)$, and duration τ is applied. A pulse with such parameters sets the Rabi vector $\vec{\Omega} = (\Omega_0 \cos \varphi, \Omega_0 \sin \varphi, 0)$ along the desired rotation axis and the pulse area to the rotation angle $\theta = \Omega_0 \tau$. The dynamic evolution driven by a simple pulse is ideal with

100% operation fidelity if the control parameters, including the Rabi frequency, phase, pulse length, and detuning, are perfect. However, when there is systematic error or random noise in the control parameters, this conventional simple pulse scheme may result in a high error rate and low fidelity.

III. SYSTEMATIC ERROR AND GATE FIDELITY

In the presence of error in the control parameters, an ideal operator U , such as in Eq. (2) turns into an imperfect operator V with erroneous rotation axis, angle, or both. Fidelity, usually used to evaluate the closeness of the two operators, is defined as [23,25,26]

$$F = |\text{Tr}(VU^\dagger)|/2. \quad (3)$$

This allows us to study the fidelity of any quantum gate independent of the qubit state.

Systematic errors in the control parameters that affect the operation in Eq. (2) can be mainly categorized as pulse area error and frequency detuning error. The error in the pulse area $\theta = \Omega \tau$ is usually caused by inaccuracy in the Rabi frequency and the pulse duration. These result in an erroneous rotation angle. The detuning error due to the frequency difference between the driving pulse and the qubit resonance causes errors in the rotation axis and angle. Similar to the treatment for the composite pulse in NMR [27–29], we consider the pulse area and detuning errors separately.

The pulse area $\theta_\varepsilon = \theta(1 + \varepsilon)$ with a percentage error ε corresponds to the operator $V(\theta, \varphi) = \exp(-i\vec{\sigma} \cdot \vec{n}\theta_\varepsilon/2)$. Using Eq. (3) the fidelity of such an operator is calculated to be

$$F_{\varepsilon\varepsilon} = \cos(\varepsilon\theta/2), \quad (4)$$

in which the fidelity degrades with the pulse area error and the rotation angle in the range of $[-\pi, \pi]$. The error affects a large rotation angle more than a small angle. The fidelity is uniform for all rotation axes at a given error level and rotation angle.

In most of the cases the percentage error in pulse area is expected to be small, where $|\varepsilon| \ll 1$ holds and the fidelity approximates to

$$F_{\varepsilon\varepsilon} \approx 1 - \frac{1}{2} \left(\frac{\theta}{2} \right)^2 \varepsilon^2. \quad (5)$$

In the presence of the frequency detuning Δ , the Rabi frequency is generalized as $\Omega = \sqrt{\Omega_0^2 + \Delta^2} = \Omega_0 \sqrt{1 + f^2}$, where Ω_0 is on-resonance Rabi frequency and $f = \Delta/\Omega_0$ is the relative detuning with respect to Ω_0 . The detuning affects both the rotation angle and the direction of the rotation axis. The ideal rotation angle θ turns into $\theta\sqrt{1 + f^2}$ and the rotation axis $\vec{n} = (\cos \varphi, \sin \varphi, 0)$ shifts to $\vec{n}_f = (\frac{1}{\sqrt{1+f^2}} \cos \varphi, \frac{1}{\sqrt{1+f^2}} \sin \varphi, \frac{f}{\sqrt{1+f^2}})$. The rotation operator becomes

$$V(\theta, \varphi) = \cos \left(\frac{\theta\sqrt{1+f^2}}{2} \right) I - i \sin \left(\frac{\theta\sqrt{1+f^2}}{2} \right) \vec{\sigma} \cdot \vec{n}_f. \quad (6)$$

The corresponding fidelity is calculated to be

$$F_{sf} = \cos \frac{\theta \sqrt{1+f^2}}{2} \cos \frac{\theta}{2} + \frac{1}{\sqrt{1+f^2}} \sin \frac{\theta \sqrt{1+f^2}}{2} \sin \frac{\theta}{2}. \quad (7)$$

Under the small error approximation $|f| \ll 1$,

$$F_{sf} \approx 1 - \frac{1}{2} \sin^2 \left(\frac{\theta}{2} \right) f^2. \quad (8)$$

Equations (7) and (8) show that the detuning degrades the fidelity with a large effect at large rotation angle. The fidelity does not depend on φ , which means uniformity for all rotation axes in the x - y plane.

IV. GEOMETRIC ROTATION

In this section a geometric rotation is designed using A-A phase [18]. The rotation defined in Eq. (2) can be rewritten using a pair of orthogonal states $|\pm\rangle_\varphi$ as

$$U(\theta, \varphi) |\pm\rangle_\varphi = e^{\mp i\theta/2} |\pm\rangle_\varphi, \quad (9)$$

where $|\pm\rangle_\varphi = \frac{1}{\sqrt{2}} (\begin{smallmatrix} 1 \\ \pm e^{i\varphi} \end{smallmatrix})$ are the eigenstates of operator $\vec{\sigma} \cdot \vec{n}$ represented by a pair of basis vectors parallel to the rotation axis \vec{n} defined by angle φ in the x - y plane as shown in Fig. 1(b). An all-geometric scheme realizes the operation in Eq. (9) by making the two basis vectors go through closed loops to acquire the required phase terms. In order to ensure the phases are purely geometric in this process where the dynamic phase vanishes, the evolution loop for each of the basis vectors has to consist of segments of great circles on the Bloch sphere [20,30]. There are infinite options to design the loops to perform a given rotation, since the number of segments could be any value from 2 to infinity while making the solid angle enclosed by the loop to be the rotation angle θ . We focus our study on a three-segment loop, which is the simplest that an on-resonant field can drive. The loops for $|+\rangle_\varphi$ and $|-\rangle_\varphi$ are marked by the shaded areas A and B, respectively in Fig. 1(b), where every segment of the loops is made on a geodesic and the solid angle enclosed by the loop is the desired rotation angle. The field that drives the eigenvectors through the loops has three segments as well, with corresponding parameters denoted as $(\pi/2, \varphi + \pi/2)$, $(\pi, \varphi - \pi/2 - \theta/2)$, and $(\pi/2, \varphi + \pi/2)$, where the first value in each parenthesis denotes the pulse area and the second value the phase. Driven by this field, basis vectors $|+\rangle_\varphi$ and $|-\rangle_\varphi$ go through their closed loops A and B in Fig. 1(b), respectively. While state $|+\rangle_\varphi$ gains a geometric phase of $-\theta/2$ becoming $e^{-i\theta/2} |+\rangle_\varphi$, state $|-\rangle_\varphi$ gains an opposite phase and turns into $e^{i\theta/2} |-\rangle_\varphi$. Under such an operation an arbitrary qubit state $|\psi\rangle = \begin{pmatrix} c_0 \\ c_1 \end{pmatrix}$ turns into

$$\begin{pmatrix} \cos \frac{\theta}{2} c_1 - i e^{-i\varphi} \sin \frac{\theta}{2} c_0 \\ -i e^{i\varphi} \sin \frac{\theta}{2} c_1 + \cos \frac{\theta}{2} c_0 \end{pmatrix}.$$

This is equivalent to applying a rotation operator in Eq. (2) to the initial state. On this geometric path the operation is accomplished by three consecutive rotations as

$$U(\theta, \varphi) = U(\pi/2, \varphi + \pi/2) U(-\pi, \varphi + \pi/2) + \pi/2 + \theta/2) U(\pi/2, \varphi + \pi/2). \quad (10)$$

Throughout the path the Rabi vectors are always perpendicular to the basis vectors, which nulls the dynamic phase change in the process.

In the presence of systematic errors in the pulse area and frequency detuning, the ideal operator in Eq. (10) turns into

$$V(\theta, \varphi) = V(\pi/2, \varphi + \pi/2) V(-\pi, \varphi + \pi/2) + \pi/2 + \theta/2) V(\pi/2, \varphi + \pi/2). \quad (11)$$

This operator is calculated by plugging in the imperfect pulse areas and/or axes in each of the segments. Then the fidelity can be calculated according to Eq. (3).

For the same percentage pulse area error ε as for the simple pulse operator, the fidelity of the geometric operator is calculated to be

$$F_{ge} = \sin^2 \frac{\pi \varepsilon}{2} \cos \frac{\theta}{2} + \cos^2 \frac{\pi \varepsilon}{2} \cos^2 \frac{\theta}{2} + \cos \frac{\pi \varepsilon}{2} \sin^2 \frac{\theta}{2}. \quad (12)$$

The fidelity is a function of both pulse area error and rotation angle while the rotation axis is not involved. When the error is small, $|\varepsilon| \ll 1$, Eq. (12) approximates to

$$F_{ge} \approx 1 - \frac{1}{2} \frac{1}{4} (\pi \varepsilon)^2 \left[\cos \frac{\theta}{2} - 1 \right]^2. \quad (13)$$

By comparing Eqs. (5) and (13), one can conclude, under the small error approximation, that the fidelity of the geometric operator is always equal to or better than the simple pulse operator. Both operators have 100% fidelity at $\theta = 0$, and a minimum fidelity, $1 - \frac{1}{2} \frac{1}{4} (\pi \varepsilon)^2$, at $|\theta| = \pi$. Other than those two points, the geometric operator always yields better fidelity. Beyond the small error regime, the comparison of the exact fidelities of the two operators is plotted in Fig. 2. The fidelity difference $F_{ge} - F_{se}$ as a function of the percentage error and the rotation angle is plotted in Fig. 2(a) and the average of the fidelity over all rotation angles in Fig. 2(b). The results show that the geometric operator holds equal or higher fidelity compared to the simple pulse operator for all rotation angles and all values of pulse area error between 0 and 100%. As a result, the geometric operator has higher average fidelity than the simple pulse operator.

Similarly, the fidelity of the geometric operator is calculated in the presence of the frequency detuning error as

$$F_{gf} = \frac{1}{1+f^2} \cos^2 \frac{\theta}{2} + \frac{f^2}{1+f^2} \cos \frac{\theta}{2} + \frac{1}{\sqrt{1+f^2}} \sin^2 \frac{\theta}{2}. \quad (14)$$

The small error approximation leads to

$$F_{gf} \approx 1 - \frac{1}{2} f^2 \left(\cos \frac{\theta}{2} - 1 \right)^2. \quad (15)$$

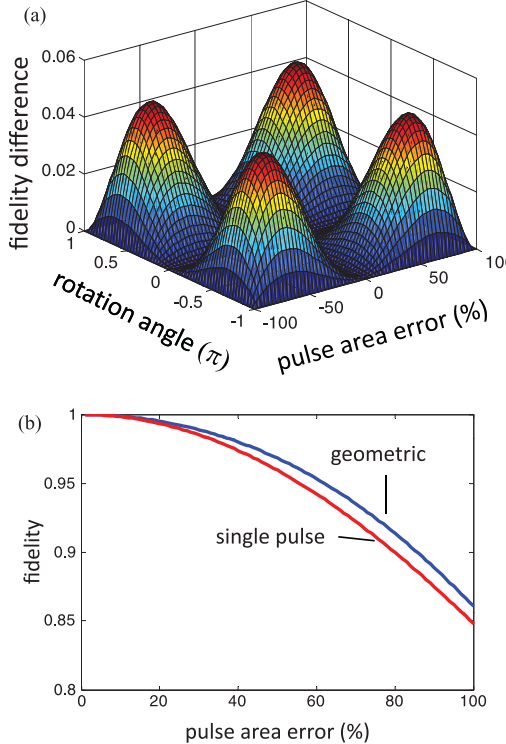


FIG. 2. (Color online) (a) Fidelity difference between geometric and simple pulse operators as a function of pulse area error and rotation angle. (b) Fidelities affected by pulse area error for geometric and simple pulse operators averaged over rotation angles from $-\pi$ to $-\pi$.

Under the condition $|f| \ll 1$, we compare the simple pulse operator in (8) and geometric operator in (15). For the rotation angle in the range of $0 < |\theta| < \pi$, $F_{\text{gf}} > F_{\text{sf}}$ holds true with the maximum fidelity $F_{\text{gf}} = F_{\text{sf}} = 1$ at $\theta = 0$, and the minimum fidelity $F_{\text{gf}} = F_{\text{sf}} = 1 - \frac{1}{2}f^2$ at $|\theta| = \pi$. The comparison of the two operators for large detuning range is presented in Fig. 3. The fidelity difference $F_{\text{gf}} - F_{\text{sf}}$ is plotted in Fig. 3(a). F_{gf} from Eq. (14) and F_{se} from Eq. (7) averaged over all rotation angles are plotted in Fig. 3(b). The results show that the geometric operator holds equal or higher fidelity compared to the simple pulse operator against the frequency detuning for all rotation angles.

The geometric operator, however, is not entirely immune to the systematic errors in the pulse area and detuning: the fidelity decreases when an error increases. Two consequences of a system error are noncyclic paths for the eigenvectors and nonvanishing dynamic phases. For practical reasons we keep to the small error regime so that the evolution paths for the eigenvectors $|\pm\rangle_\varphi$ can still be approximated as closed loops. As a result, the degradation of the operation fidelity caused by the erroneous Hamiltonian should be attributed to the dynamic phase. We calculated the dynamic phase according to $\alpha_d = -\frac{i}{\hbar} \int \langle \chi(t)|H|\chi(t)\rangle_\varphi dt$, where $|\chi(t)\rangle_\varphi$ represents the states evolving from the initial state $|+\rangle_\varphi$ on path A shown in

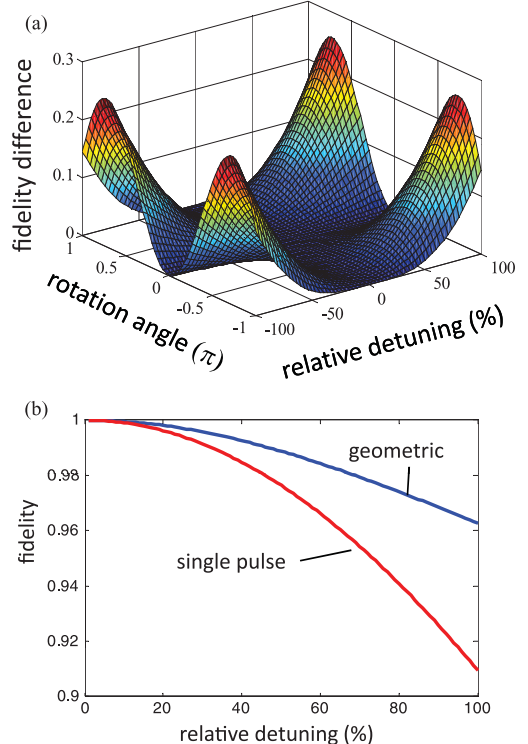


FIG. 3. (Color online) (a) Fidelity difference between geometric and simple pulse operators as a function of frequency detuning and rotation angle. (b) Fidelities affected by frequency detuning for geometric and simple pulse operators averaged over rotation angles from $-\pi$ to $-\pi$.

Fig. 1(b). Under small pulse area error, $|\varepsilon| \ll 1$, the dynamic phase was calculated to be

$$\alpha_{\text{de}} \approx \left(\frac{\pi}{2}\right)^2 \varepsilon \sin \frac{\theta}{2} \left(2 - \cos \frac{\theta}{2}\right). \quad (16)$$

This adds an extra angle $2|\alpha_{\text{de}\pm}|$ to the desired rotation. Comparing Eqs. (13) and (16) reveals the relationship between the fidelity degradation and the dynamic phase as,

$$F_{\text{ge}} = 1 - \frac{2}{\pi^2} \frac{1 - \cos \frac{\theta}{2}}{(1 + \cos \frac{\theta}{2}) [2 - \cos \frac{\theta}{2}]^2} \alpha_{\text{de}}^2. \quad (17)$$

The second term shows the fidelity decreases quadratically with the dynamic phase caused by the pulse area error. A fidelity of 100% is achieved for a pure geometric operator, corresponding to a vanishing dynamic phase.

The fidelity degradation caused by the detuning was studied in a similar way. Under small error approximation, we calculated the dynamic phase as a function of the detuning and the rotation angle as

$$\alpha_{\text{df}} \approx \frac{\pi}{2} f \left(\cos \frac{\theta}{2} - 1\right)^2. \quad (18)$$

Comparing the dynamic phase in (18) and the fidelity in (15), one can see the fidelity degradation is linked to the dynamic phase as

$$F_{\text{gf}} = 1 - \frac{2}{\pi^2} \frac{1}{(\cos \frac{\theta}{2} - 1)^2} \alpha_{\text{df}}^2, \quad (19)$$

which shows a similar relationship: the fidelity degrades quadratically with the dynamic phase caused by the frequency detuning.

While the rotation operator in Eq. (10) is all geometric under the ideal condition, systematic errors cause the eigenvectors to evolve on non-purely geometric paths. This is manifested as a nonvanishing dynamic phase. As a result, the operation fidelity decreases. This is consistent with the conclusion that the geometric path yields the highest fidelity.

V. CONCLUSION

A Bloch rotation operator based on nonadiabatic Abelian geometric phase has been designed and analyzed using a general model for a two-level qubit driven by a parameterized Hamiltonian. This operator is sufficient to make a set of universal single-qubit gates by setting the parameters such as pulse area, frequency, and phase of the effective control field. The fidelity of the geometric operator was analyzed against the systematic errors in the pulse area and the frequency detuning. An operator-based fidelity definition was used so that the results are independent of the qubit state. The geometric rotation operator was compared with the conventional simple pulse dynamic rotation. The systematic error degrades both types of operations with low fidelity at large rotation angle. The geometric operator shows overall improved fidelity over the simple pulse rotation. The reason for the degradation of the geometric operation is that the operator is no longer purely geometric when the systematic errors in both pulse area and frequency detuning cause the evolution path to deviate from the geometric path. As a result, the decrease in the fidelity is related to a nonvanishing dynamic phase. Further investigation is needed on the origin of the robustness of the

geometric rotation against systematic errors compared with the dynamic operator.

Since our analysis is based on a generic nondegenerate two-level qubit model, the method and results in this paper are applicable to a variety of physical qubit systems, such as: NMR, atoms, ions, photons, superconducting circuits, and quantum dots. The model is suitable for both single-entity and ensemble qubits. When the inhomogeneity exists in the pulse area error or the frequency detuning in an ensemble, the fidelity calculation should be averaged over the entire ensemble. Geometric two-qubit gates, such as controlled-not and controlled-phase gates, can be analyzed in a similar way by introducing a qubit-qubit coupling term to the driving Hamiltonian.

While systematic control errors that can be parameterized into effective pulse area and frequency detuning errors exist in realistic systems, stochastic random fluctuation in the Hamiltonian is equally important. Both the dynamic and geometric operators discussed in this paper can be studied through numerical calculation of the fidelity according to Eq. (3), which is quite straightforward. However, the results will depend on the noise model, which could be quite different for the parameterized effective field in different physical systems and needs further investigation.

Our results on systematic errors are obtained for the simplest geometric path driven by an on-resonance effective field. More geometric paths can be designed by including off-resonance fields. For the practical purpose of achieving maximal gate fidelity, the path design should be optimized against both systematic and stochastic errors. The composition of the set of universal gates could play an important role as well in the optimization process.

ACKNOWLEDGMENTS

The authors gratefully acknowledge grant support from National Institute of Standards and Technology (Contract No. 70NANB7H6138, Am 001) and from the Office of Naval Research (Contract No. N00014-09-1-1025A). M.L. would like to thank Dr. Sophia Economou for fruitful discussions.

-
- [1] D. Deutsch, *Proc. R. Soc. London A* **425**, 73 (1989).
 - [2] E. Knill, *Nature* **434**, 39 (2005).
 - [3] P. W. Shor, *Phys. Rev. A* **52**, R2493 (1995); A. M. Steane, *Phys. Rev. Lett.* **77**, 793 (1996).
 - [4] C. M. Dawson, H. L. Haselgrave, and M. A. Nielsen, *Phys. Rev. Lett.* **96**, 020501 (2006); R. Li, M. Hoover, and F. Gaitan, *Quant. Info. Camp.* **9**, 290 (2009).
 - [5] P. Zanardi and M. Rasetti, *Phys. Lett. A* **264**, 94 (1999).
 - [6] A. Recati, T. Calarco, P. Zanardi, J. I. Cirac, and P. Zoller, *Phys. Rev. A* **66**, 032309 (2002).
 - [7] J. Pachos and S. Chountasis, *Phys. Rev. A* **62**, 052318 (2000).
 - [8] X.-B. Wang and M. Keiji, *Phys. Rev. Lett.* **87**, 097901 (2001); J. A. Jones, V. Vedral, A. Ekert, and G. Castagnoli, *Nature* **398**, 305 (2002); Y. Ota, Y. Goto, Y. Kondo, and A. M. Nakahara, *Phys. Rev. A* **80**, 052311 (2009).
 - [9] L.-M. Duan, J. I. Cirac, and P. Zoller, *Science* **292**, 1695 (2001); F. Schmidt-Kaler, H. Haffner, M. Riebe, S. Gulde, G. P. T. Lancaster, T. Deuschle, C. Becher, C. F. Roos, J. Escher, and R. Blatt, *Nature* **422**, 408 (2003); D. Leibfried *et al.*, *ibid.* **422**, 412 (2003).
 - [10] J. J. Garcia-Ripoll and J. I. Cirac, *Philos. Trans. R. Soc. London A* **361**, 1537 (2003).
 - [11] G. Falci, R. Fazio, G. M. Palma, J. Siewert, and V. Vedral, *Nature* **407**, 355 (2000).
 - [12] M. Tian, Z. W. Barber, J. A. Fischer, and W. R. Babbitt, *Phys. Rev. A* **69**, 050301(R) (2004); M. Tian, I. Zafarullah, T. Chang, R. K. Mohan, and W. R. Babbitt, *ibid.* **79**, 022312 (2009).
 - [13] S. E. Economou and T. L. Reinecke, *Phys. Rev. Lett.* **99**, 217401 (2007); S. Yin and D. M. Tong, *Phys. Rev. A* **79**, 044303 (2009).
 - [14] O. Oreshkov, T. A. Brun, and D. A. Lidar, *Phys. Rev. Lett.* **102**, 070502 (2009); O. Oreshkov, *ibid.* **103**, 090502 (2009).
 - [15] G. De Chiara and G. M. Palma, *Phys. Rev. Lett.* **91**, 090404 (2003); P. Solinas, P. Zanardi, and N. Zanghi, *Phys. Rev. A* **70**, 042316 (2004); C. Lupo, P. Aniello, M. Napolitano, and G. Florio, *ibid.* **76**, 012309 (2007).

- [16] G. Florio, P. Facchi, R. Fazio V. Giovannetti, and S. Pascazio, *Phys. Rev. A* **73**, 022327(2006).
- [17] M. V. Berry, *Proc. R. Soc. London A* **392**, 45 (1984).
- [18] Y. Aharonov and J. Anandan, *Phys. Rev. Lett.* **58**, 1593 (1987).
- [19] A. Nazir, T. P. Spiller, and W. J. Munro, *Phys. Rev. A* **65**, 042303 (2002).
- [20] A. Blais and A. M. S. Tremblay, *Phys. Rev. A* **67**, 012308 (2003).
- [21] S-L Zhu and P. Zanardi, *Phys. Rev. A* **72**, 020301(R) (2005).
- [22] S. Fillipp, *Eur. Phys. J.* **160**, 165 (2008).
- [23] M. A. Nielsen and I. L. Chuang, *Quantum Computation and Quantum Information* (Cambridge University Press, Cambridge, 2000).
- [24] L. Allen and J. H. Eberly, *Optical Resonance, and Two-Level Atoms* (Dover Publications, Inc., New York, 1987).
- [25] M. Nielsen, *Phys. Lett. A* **303**, 249 (2002); C. M. Dawson, H. L. Haselgrove, and M. A. Nielsen, *Phys. Rev. A* **73**, 052306 (2006).
- [26] X. Wang, C-S. Yu, and X. X. Yi, *Phys. Lett. A* **373**, 58 (2008).
- [27] M. H. Levitt, *Prog. NMR Spectrosc.* **18**, 61 (1986).
- [28] R. Tycko, *Phys. Rev. Lett.* **51**, 775 (1983).
- [29] J. A. Jones, *Philos. Trans. R. Soc. London A* **361**, 1429 (2003).
- [30] E. Sjoqvist, *Physics* **1**, 35 (2008).

Bibliography

Bibliography

- [1] V. Heine, Proceedings of the Physical Society (London) **81**, 300 (1963).
- [2] <http://lababidi.me/phys/flatband/>.
- [3] K. v. Klitzing, G. Dorda, and M. Pepper, Physical Review Letters **45**, 494 (1980).
- [4] C. L. Kane and E. J. Mele, Physical Review Letters **95**, 226801 (2005).
- [5] B. A. Bernevig, T. L. Hughes, and S.-C. Zhang, Science **314**, 1757 (2006), PMID: 17170299.
- [6] M. König et al., Science **318**, 766 (2007), PMID: 17885096.
- [7] L. Fu and C. L. Kane, Physical Review Letters **100**, 096407 (2008).
- [8] M. Z. Hasan and C. L. Kane, Reviews of Modern Physics **82**, 3045 (2010).
- [9] J. Linder, Y. Tanaka, T. Yokoyama, A. Sudb, and N. Nagaosa, Physical Review Letters **104**, 067001 (2010).
- [10] X. Qi and S. Zhang, Reviews of Modern Physics **83**, 1057 (2011).
- [11] J. Seo et al., Nature **466**, 343 (2010).
- [12] O. V. Yazyev, J. E. Moore, and S. G. Louie, Physical Review Letters **105**, 266806 (2010).
- [13] A. A. Burkov and D. G. Hawthorn, Physical Review Letters **105**, 066802 (2010).
- [14] H. Peng et al., Nature Materials **9**, 225 (2010).
- [15] J. G. Analytis et al., Physical Review B **81**, 205407 (2010).
- [16] P. Cheng et al., Physical Review Letters **105**, 076801 (2010).
- [17] Q. Liu, C.-X. Liu, C. Xu, X.-L. Qi, and S.-C. Zhang, Physical Review Letters **102**, 156603 (2009).
- [18] H.-Z. Lu, W.-Y. Shan, W. Yao, Q. Niu, and S.-Q. Shen, Physical Review B **81**, 115407 (2010).
- [19] B. Seradjeh, J. E. Moore, and M. Franz, Physical Review Letters **103**, 066402 (2009).
- [20] D. Hsieh et al., Nature **452**, 970 (2008).

- [21] L. Fu, C. L. Kane, and E. J. Mele, Physical Review Letters **98**, 106803 (2007).
- [22] L. Fu and C. L. Kane, Physical Review B **76**, 045302 (2007).
- [23] D. Hsieh et al., Nature **460**, 1101 (2009).
- [24] D. Hsieh et al., Physical Review Letters **103**, 146401 (2009).
- [25] D. Hsieh et al., Science **323**, 919 (2009), PMID: 19213915.
- [26] P. Roushan et al., Nature **460**, 1106 (2009).
- [27] V. P. Mineev and K. V. Samochin, *Introduction to Unconventional Superconductivity*, Taylor & Francis, 1999.
- [28] N. Read and D. Green, Phys. Rev. B **61**, 10267 (2000).
- [29] L. Fu and C. L. Kane, Phys. Rev. Lett. **100**, 096407 (2008).
- [30] T. Tokuyasu, J. A. Sauls, and D. Rainer, Phys. Rev. B **38**, 8823 (1988).
- [31] L. Fu, C. L. Kane, and E. J. Mele, Phys. Rev. Lett. **98**, 106803 (2007).
- [32] J. E. Moore and L. Balents, Phys. Rev. B **75**, 121306 (2007).
- [33] R. Roy, Phys. Rev. B **79**, 195322 (2009).
- [34] D. Hsieh et al., Nature **452**, 970 (2008).
- [35] Y. Xia et al., Nat Phys **5**, 398 (2009).
- [36] H. Zhang et al., Nat Phys **5**, 438 (2009).
- [37] Y. L. Chen et al., Science **325**, 178 (2009).
- [38] D. Hsieh et al., Nature **460**, 1101 (2009).
- [39] A. A. Burkov and D. G. Hawthorn, Phys. Rev. Lett. **105**, 066802 (2010).
- [40] X.-L. Qi and S.-C. Zhang, Physics Today **63**, 33 (2010).
- [41] M. Z. Hasan and C. L. Kane, ArXiv:1002.3895 (2010).
- [42] X. Qi and S. Zhang, ArXiv:1008.2026 (2010).
- [43] T. Yokoyama, Y. Tanaka, and N. Nagaosa, Phys. Rev. Lett. **102**, 166801 (2009).
- [44] V. Heine, Phys. Rev. **138**, A1689 (1965).
- [45] S. G. Louie and M. L. Cohen, Phys. Rev. B **13**, 2461 (1976).
- [46] J. Tersoff, Phys. Rev. Lett. **52**, 465 (1984).
- [47] A. Millis, D. Rainer, and J. A. Sauls, Phys. Rev. B **38**, 4504 (1988).

- [48] T. D. Stanescu, J. D. Sau, R. M. Lutchyn, and S. Das Sarma, Phys. Rev. B **81**, 241310 (2010).
- [49] J. G. Checkelsky, Y. S. Hor, R. J. Cava, and N. P. Ong, ArXiv:1003.3883 (2010).
- [50] I. V. Tokatly, A. G. Tsibizov, and A. A. Gorbatsevich, Phys. Rev. B **65**, 165328 (2002).
- [51] D. J. BenDaniel and C. B. Duke, Phys. Rev. **152**, 683 (1966).
- [52] W. Kohn, Phys. Rev. **115**, 809 (1959).
- [53] E. I. Blount, *Solid State Physics*, volume 13, Academic Press, 1962.
- [54] Y.-C. Chang and J. N. Schulman, Phys. Rev. B **25**, 3975 (1982).
- [55] X.-L. Qi, T. L. Hughes, and S.-C. Zhang, Phys. Rev. B **78**, 195424 (2008).
- [56] N. F. Mott and H. S. Massey, *The Theory of Atomic Collisions*, Oxford University Press, 3rd edition, 1965.
- [57] F. Garcia-Moliner and V. R. Velasco, *Theory of single and multiple interfaces*, World Scientific, 1992.
- [58] L. Fu and C. L. Kane, Physical Review Letters **100**, 096407 (2008).
- [59] N. Read and D. Green, Physical Review B **61**, 10267 (2000).
- [60] X. Qi and S. Zhang, Reviews of Modern Physics **83**, 1057 (2011).
- [61] R. M. Lutchyn, J. D. Sau, and S. Das Sarma, Physical Review Letters **105**, 077001 (2010).
- [62] J. D. Sau, S. Tewari, R. M. Lutchyn, T. D. Stanescu, and S. Das Sarma, Physical Review B **82**, 214509 (2010).
- [63] J. Alicea, Physical Review B **81**, 125318 (2010).
- [64] L. Mao and C. Zhang, Physical Review B **82**, 174506 (2010).
- [65] L. Mao, J. Shi, Q. Niu, and C. Zhang, Physical Review Letters **106**, 157003 (2011).
- [66] Y. Tanaka, T. Yokoyama, and N. Nagaosa, Physical Review Letters **103**, 107002 (2009).
- [67] J. Linder, Y. Tanaka, T. Yokoyama, A. Sudb, and N. Nagaosa, Physical Review B **81**, 184525 (2010).
- [68] J. Linder, Y. Tanaka, T. Yokoyama, A. Sudb, and N. Nagaosa, Physical Review Letters **104**, 067001 (2010).
- [69] B. Sacp et al., Nat Commun **2**, 575 (2011).

- [70] M. Veldhorst et al., Bulletin of the American Physical Society **Volume 56, Number 1**.
- [71] D. M. Zhang et al., Bulletin of the American Physical Society **Volume 56, Number 1**.
- [72] A. M. Black-Schaffer, Physical Review B **83**, 060504 (2011).
- [73] Y. S. Hor et al., Physical Review Letters **104**, 057001 (2010).
- [74] L. A. Wray et al., Nat Phys **6**, 855 (2010).
- [75] M. Kriener, K. Segawa, Z. Ren, S. Sasaki, and Y. Ando, Physical Review Letters **106**, 127004 (2011).
- [76] H. Zhang et al., Nat Phys **5**, 438 (2009).
- [77] W. Zhang, R. Yu, H. Zhang, X. Dai, and Z. Fang, New Journal of Physics **12**, 065013 (2010).
- [78] E. Zhao, C. Zhang, and M. Lababidi, ArXiv:1005.3064 (2010).
- [79] K. Halterman and O. T. Valls, Physical Review B **65**, 014509 (2001).
- [80] B. P. Stojkovi and O. T. Valls, Physical Review B **47**, 5922 (1993).
- [81] M. Eschrig, Phys. Rev. B **80**, 134511 (2009).
- [82] Y. Tanaka, T. Yokoyama, and N. Nagaosa, Phys. Rev. Lett. **103**, 107002 (2009).
- [83] F. S. Bergeret, A. F. Volkov, and K. B. Efetov, Reviews of Modern Physics **77**, 1321 (2005).
- [84] M. I. Katsnelson, K. S. Novoselov, and A. K. Geim, Nat Phys **2**, 620 (2006).
- [85] J. R. Williams et al., Physical Review Letters **109**, 056803 (2012).
- [86] J. Moore, Physics **5**, 84 (2012).
- [87] C. W. J. Beenakker, Phys. Rev. Lett. **97**, 067007 (2006).
- [88] C. W. J. Beenakker, Rev. Mod. Phys. **80**, 1337 (2008).
- [89] The exact choice of boundary conditions will not affect the local physics at the junction, if L is sufficiently large. The open boundary condition may be realized, as an example, by having strong ferromagnets at $x = 0, L$. They will introduce chiral edge modes spatially well separated from the center of the junction and will not affect the local spectrum there.
- [90] K. Halterman, O. T. Valls, and M. Alidoust, Physical Review B **84**, 064509 (2011).
- [91] M. Lababidi and E. Zhao, Phys. Rev. B **83**, 184511 (2011).
- [92] T. Heikkilä and G. Volovik, JETP Letters **93**, 59 (2011).

- [93] See Supplementary Materials for the evolution of the spectrum of the whole system for increasing μ_{TI} . $\mu_S = 100\text{meV}$, $\Delta = 6\text{meV}$, $L = 500\text{nm}$, $W = 50\text{nm}$.
- [94] The realization of Larkin-Ovchinnikov superconductor usually requires a Zeeman field. Our proposal needs LO states without magnetic field, such as those described in arXiv:1209.2235 by Cho et al.
- [95] T. T. Heikkilä, N. B. Kopnin, and G. E. Volovik, JETP Letters **94**, 252 (2011).
- [96] T. H. Hsieh and L. Fu, Physical Review Letters **108**, 107005 (2012).
- [97] P. M. R. Brydon, A. P. Schnyder, and C. Timm, Phys. Rev. B **84**, 020501 (2011).
- [98] A. P. Schnyder and S. Ryu, Physical Review B **84**, 060504 (2011).
- [99] B. Sacépé et al., Nat Commun **2** (2011).
- [100] D. Zhang et al., Phys. Rev. B **84**, 165120 (2011).
- [101] M. Veldhorst et al., Nat Mater **11**, 417 (2012).
- [102] F. Qu et al., Sci. Rep. **2** (2012).
- [103] J. R. Williams et al., eprint arXiv:1202.2323 (2012).
- [104] M. Veldhorst, C. G. Molenaar, X. L. Wang, H. Hilgenkamp, and A. Brinkman, eprint arXiv:1112.5858 (2011).
- [105] A. Zazunov, V. S. Shumeiko, E. N. Bratus', J. Lantz, and G. Wendum, Phys. Rev. Lett. **90**, 087003 (2003).
- [106] T. Meng and L. Balents, Physical Review B **86**, 054504 (2012).
- [107] Y. L. Chen et al., Science **329**, 659 (2010), PMID: 20689013.
- [108] J. Zhang et al., Science **339**, 1582 (2013), PMID: 23539598.

Curriculum Vitae

Mahmoud Lababidi was born in 1983 in the United States. He earned his Bachelor of Science in Computer Engineering from the University of Florida, Gainesville in 2006. He enrolled in the Physics PhD program at George Mason University in 2008 and began working under the supervision of Professor Erhai Zhao in 2010.

List of Publications

I

Mott scattering at the interface between a metal and a topological insulator
Erhai Zhao and Chun Zhang and Mahmoud Lababidi
Physical Review B 82, 205331

II

Microscopic simulation of superconductor/topological insulator proximity structures
Mahmoud Lababidi and Erhai Zhao
Physical Review B 83, 184511

III

Nearly flat Andreev bound states in superconductor-topological insulator hybrid structures
Mahmoud Lababidi and Erhai Zhao
Physical Review B 86, 161108(R)

IV

Anomalous edge states and topological phases of a kicked quantum Hall system
Mahmoud Lababidi, Indubala I. Satija, and Erhai Zhao
arXiv:1307.3569

V

Robustness of single-qubit geometric gate against systematic error
J. T. Thomas, Mahmoud Lababidi, and Mingzhen Tian
Physical Review A 84, 042335